O'Brien, P.E., Cooper, A.K., Richter, C., et al., 2001
Proceedings of the Ocean Drilling Program, Initial Reports Volume 188

4. SITE 1166[1]

Shipboard Scientific Party[2]

PRINCIPAL RESULTS

Hole 1166A

Position: 67°41.77′S, 74°47.22′E
Start hole: 1310 hr, 16 February 2000
End hole: 1600 hr, 21 February 2000
Time on hole (hr): 134.5
Seafloor (drill-pipe measurement from rig floor, mbrf): 486.7
Distance between rig floor and sea level (m): 11.3
Water depth (drill-pipe measurement from sea level, m): 475.4
Total depth (drill-pipe measurement from rig floor, mbrf): 868.0
Penetration (mbsf): 381.3
Coring totals: type: RCB; number: 40; cored: 381.3m; recovered: 18.6%
Lithology:

Subunit IA–poorly sorted diatom-bearing sandy silty clay
Subunit IB–diamicton
Subunit IC–interbedded, poorly sorted sandy silt with lonestones (and diatoms) and diatom-bearing clayey silt
Subunit ID–diamicton and poorly sorted clayey sandy silt
Unit II–claystone and diatom-bearing claystone interbedded with sand beds
Unit III–matrix-supported coarse to very coarse sand with abundant granules
Unit IV–homogeneous highly carbonaceous clay and laminated sandy silt with organic detritus
Unit V–claystone with very fine laminations and very fine sandy silt

[1]Examples of how to reference the whole or part of this volume.
[2]Shipboard Scientific Party addresses.

Ms 188IR-104

Hole 1166B

Position: 67°41.79′S, 74°47.22′E
Start hole: 1600 hr, 21 February 2000
End hole: 1330 hr, 22 February 2000
Time on hole (hr): 21.5
Seafloor (drill-pipe measurement from rig floor, mbrf): 480.0
Distance between rig floor and sea level (m): 11.3
Water depth (drill-pipe measurement from sea level, m): 511.2
Total depth (drill-pipe measurement from rig floor, mbrf): 522.5
Penetration (mbsf): 42.5
Coring totals: No core; Dedicated logging while drilling hole.

Site 1166 is situated on the Prydz Bay continental shelf on the southwestern flank of Four Ladies Bank, ~40 km southwest of Ocean Drilling Program (ODP) Site 742 (Leg 119). Prydz Bay is at the downstream end of a drainage system that originates in the Gamburtsev Mountains of central East Antarctica. The early development and growth of the Cenozoic Antarctic Ice Sheet is believed to have started in middle Eocene to early Oligocene time, but to date, drilling on the continent and the continental margin has not sampled a stratigraphic section that clearly spans and includes the transition period from preglacial to glacial conditions. Site 1166 was chosen to recover core from the Cenozoic sediments below the horizon reached at Site 742. This was intended to provide an age for the arrival of glaciers in Prydz Bay and a record of changes in paleoenvironments and biota with the onset of glaciation.

When the *JOIDES Resolution* arrived in Prydz Bay, the drill site had to be moved to an alternate site because pack ice covered much of western Prydz Bay where the primary site was located. An additional 3-nmi displacement of the site was required because a large tabular iceberg was floating directly over the alternate site. The target sedimentary section was thinner and likely a little younger near the base of the section at the final alternate site (i.e., Site 1166) than at the primary site. The drilling at Site 1166 was conducted safely and achieved the desired objective under the sometimes cold and stormy operating conditions.

Drilling at Site 1166 had to be halted temporarily about midway through because of a large storm with wind gusts exceeding 40 kt and swells >2 m, the maximum limit for shallow-water drilling. During the storm, an iceberg approached within 0.6 nmi, and the drill pipe had to be pulled out of the seafloor without a reentry cone in place. The ship was moved away from the site. Following the storm, the ship returned to the site and successfully reentered the hole to continue uninterrupted drilling to a total depth of 381.3 meters below sea floor (mbsf). Recovery at the site was 18.6%; low recovery was due partly to drilling through the upper section (135 mbsf) of diamictites, similar to those sampled at Site 742, and because of sandy fine-grain sediments in the lower part of the hole. Three full logging runs were obtained with excellent data from ~50 mbsf to the bottom of the hole.

The sedimentary section at Site 1166 comprises a diverse suite of strata that from the top down include glacial, early glacial, and preglacial rocks that consist of poorly sorted, sandy, and fine-grained sediments. The ages range from Holocene at the seafloor to Late Cretaceous at the bottom of the hole, with many disconformities throughout.

The sediments are divided into five lithostratigraphic units. Lithostratigraphic Unit I is of late Pliocene to Holocene age and comprises four subunits. The uppermost subunit (Subunit IA; 0.0–2.74 mbsf) is a

biogenic-rich clay interval with pebble-sized clasts. This unit is interpreted as an ice-keel turbate, based in part on iceberg furrows that occur echo-sounder records in this area (O'Brien and Leitchenkov, 1997).

Below Subunit IA are two intervals of diamicton and one of poorly sorted clayey sandy silt. Subunits IB (2.79–106.36 mbsf) and ID (123.0–135.41 mbsf) are separated by a thin interval (Subunit IC; 113.30–117.22 mbsf) of biogenic-rich clayey silt. Subunit IB is predominantly clayey silt with rock pebbles and clasts that include common fibrous black organic matter. Minor (<2 cm thick) sand and granule beds are present. Subunit IC is interbedded dark gray sandy silt with lonestones and greenish gray diatom-bearing clayey silt with dispersed granules. Biogenic-rich intervals are slightly bioturbated. Contacts with the dark silt are sharp. Subunit ID has interbeds of dark gray clast-poor and clast-rich diamicton. Clast lithologies vary and include gneiss, granite, and diorite rocks. The diamictons suggest subglacial deposition; the sandy silt with ice-rafted debris (IRD) is a glaciomarine unit deposited during interglacial periods.

Unit I has lonestones throughout. For Subunits IB and ID, the diamictons suggest subglacial deposition or deposition of a proglacial morainal bank. Sandy silt intervals with shell fragments and microfossils (Subunit IC) suggest current reworking and glaciomarine sedimentation during times of significant glacial retreat. The lonestones signify deposition of IRD. In seismic reflection data, Unit I comprises the topset beds of the seaward-prograding sedimentary section of the outer continental shelf. The contact between lithostratigraphic Units I and II is an abrupt unconformity and was recovered (interval 188-1166A-15R, 8–11 cm [135.63 mbsf]). X-ray diffraction (XRD) data above and below the unconformity show shifts in relative abundances of mica, illite, kaolinite, hornblende, and plagioclase. The shifts suggest increased amounts of weathered terrigenous material within Unit I, just above the unconformity.

Unit II (135.63–156.62 mbsf) is an upper Eocene to lower Oligocene diatom-bearing claystone with thin interbedded sands and lonestones. Carbonate contents range from 0.4 to 3.3 wt%. Sands are poorly sorted and bioturbation is moderate. Rare fibrous black organic clasts are present within the sand beds. The bottom of Unit II has rhythmically interbedded centimeter-thick sand and dark claystone. XRD shows gibbsite and kaolinite in Unit II, suggesting erosion of chemically weathered material produced during soil formation. Unit II is a marine sequence that records ice rafting of pebbles during a marine transgression. At Site 742 (Leg 119), 40 km away, similar or younger-age sediments that were interpreted as proximal glacially influenced proglacial or subglacial deposits were sampled. The contact between lithostratigraphic Units II and III is abrupt and was also recovered (interval 188-1166A-17R, 77–78 cm).

Unit III (156.62–267.17 mbsf) consists of massive and deformed sands with a silty clay matrix. The unit is of late Eocene age based on initial palynological studies (O'Brien et al., in press). Calcium carbonate content ranges from 0.4 to 8.4 wt%. The sands have a uniform fabric, are poorly sorted, and lack internal structure. Pebbles of quartzite and rare fibrous black organic fragments are widely dispersed throughout. Two calcite-cemented intervals are present in the sands. The lower part of Unit III is deformed and folded by soft-sediment deformation of sandy beds and includes black organic-rich material with pieces of wood. The coarse-grained sands record deposition on an alluvial plain or delta, and the deformed beds record some reworking of material

from underlying organic-rich horizons. A similar-looking sequence of carbonaceous material was drilled in the bottom 2 m at Site 742 and was interpreted as fluvial or possibly lacustrine. At Site 742, however, a sequence comparable to the homogeneous coarse sands was not recovered. The coarse sands of Unit III may record a preglacial alluvial plain or a braided delta of a glacial outwash system. The contact between lithostratigraphic Units III and IV was not sampled.

Unit IV (276.44–314.91 mbsf) comprises black highly carbonaceous clay and fine sandy silt with organic-rich laminae and rare to moderate bioturbation. The sandy silt contains abundant mica and some pyrite. The organic-rich laminae have organic carbon (OC) values as high as 9 wt% and contain common occurrences of authigenic sulfides. Calcium carbonate content ranges from 0.3 to 3.7 wt%. Unit IV records deposition in a restricted marine or lagoonal environment. Initial palynological studies indicate a Turonian age for Unit IV (O'Brien et al., in press).

Unit V (342.80–342.96 mbsf) consists of a small sample of undated finely laminated gray claystone that was captured in the core catcher within a thick no-recovery zone at the bottom of the hole. From resistivity and velocity log data, the unit may have a relatively large clay content. The claystone is likely preglacial in origin. The interpretation is based on tentative lithologic and seismic stratigraphic correlation with ODP Site 741, 110 km away, from which Lower Cretaceous gray claystone was recovered (Barron, Larson, et al., 1989). Palynomorphs indicate a Turonian age (86–91 Ma) (O'Brien et al., in press).

Diatoms, radiolarians, foraminifers, and calcareous nannofossils were examined at Site 1166. Diatoms are present in limited intervals of the core and provide the primary biostratigraphic age control. Three distinct diatom assemblages were noted—Quaternary, Pliocene, and late Eocene–early Oligocene age. Extant Quaternary diatoms occur at 2.12–2.92 mbsf (age = <0.66 Ma). Quaternary to upper Pliocene diatoms occur in diamicts to at least 106.37 mbsf. Two layers of diatomaceous clay (~113.95–114.10 and ~114.50–115.15 mbsf) occur, containing the upper Pliocene diatom *Thalassiosira kolbei* (1.8–2.2 Ma) and the *Thalassiosira vulnifica* to *Thalassiosira striata–T. vulnifica* Zones (2.2–3.2 Ma), respectively. Radiolarians suggest an age of >2.4 Ma for the lower bed. The boundary between lithostratigraphic Units I and II is a major disconformity (~30 m.y.). Diatoms in Unit II between 135.73 and 153.48 mbsf are of early Oligocene–late Eocene age (~33–37 Ma). Diatoms were not recovered below Unit II, but several specimens of pollen, spores, dinoflagellates, and wood fragments were noted in lower intervals of the hole. Planktonic foraminifers are common above ~90 mbsf, and their ages generally agree with those for diatoms and radiolarians. Calcareous nannofossils are rare.

Paleomagnetic stratigraphy is difficult because of limited core recovery, but a clear pattern of magnetic polarity intervals is recorded where the recovery is relatively high. A correlation to the geomagnetic polarity time scale (GPTS) is in progress using key biostratigraphic datums. Downhole variations in the concentration-dependent and magnetic mineralogy-dependent parameters show that the main lithostratigraphic units have alternating high and low magnetic mineral concentrations and distinct magnetic signatures. Iron sulfide minerals are present below ~140 mbsf.

Interstitial water profiles document downhole sediment diagenesis and diffusional exchange with bottom seawater. From 0 to 150 mbsf, the oxidation of organic matter reduces sulfate values from 28 to 8 mM and ammonium increases from 177 to 1277 mM. From 0 to 75 mbsf, al-

kalinity decreases from 4.5 to 1 mM, silica decreases from 800 to 200 mM, potassium decreases from 12 to 2 mM, and calcium increases from 10 to 22 mM. The profiles suggest diagenetic silicate reactions are occurring within the sulfate reduction zone. Between 150 and 300 mbsf, calcium and magnesium show minor changes in relative concentration (15 and 24 mM, respectively) suggesting diffusional processes are dominant.

OC contents of the sediments based on 14 samples (selected by dark color) vary according to lithostratigraphic unit. The diamictite (Subunit IB) has OC values of 0.4–1.4 wt%; the massive sand (Unit III) has OC values of 0.2–0.5 wt%, except for one bed near the base of the fluvial/deltaic sand section of Unit III that contains 9.2 wt% OC; the carbonaceous claystone (Unit IV) has 1.5–5.2 wt% OC. Inorganic carbon was low (<0.1 wt%) throughout most of the recovered section. Gas analyses showed only background levels of methane (4–10 ppmv), and no other hydrocarbons were detected. Most samples are enriched in carbon relative to nitrogen, which suggests the input of land-plant organic matter, especially for samples with >1 wt% OC. Rock-Eval pyrolysis analysis shows that the pyrolyzable fraction of the OC is low (hydrogen index values of 50 mg of hydrocarbon per gram of carbon or less), consistent with degraded plant material as the source of the carbon in the more carbonaceous (>2 wt%) samples. Samples with lower carbon contents (<1.4 wt%) may contain a recycled higher thermal maturity component. This recycled organic component is suggested by Rock-Eval T_{max} values that approach 490°C as OC decreases toward values of 0.5 wt%. The diamictites (Unit I) have a greater proportion of recycled organic matter than the carbonaceous units (base of Units III and IV), which contain mostly first-cycle organic matter.

The majority of the sedimentary section has porosities between 20% and 40%, with the exception of Unit II, where the average porosity is 50%. *P*-wave velocities change abruptly at most lithostratigraphic boundaries. The measured shear strengths show that the sediments, especially in Unit I, are overconsolidated, with an overconsolidation ratio of ~2 below 70 mbsf. The overconsolidation record implies at least one or two periods when sediments were either compacted by a 250- to 300-m-thick sediment column, now eroded away, or were loaded by 330- to 420-m-thick nonbuoyant ice during prior glaciations.

Wireline logging was carried out in Hole 1166A with excellent results. Three runs were made using the triple combination (triple combo), sonic/geological high-sensitivity magnetic tool (GHMT), and Formation MicroScanner (FMS) tool from 33 mbsf to the bottom of the hole at 385 mbsf. Six logging units are recognized, and each stratigraphic unit has a distinctive signature and appearance, especially in the resistivity, sonic velocity, and FMS data. The deeper parts of the hole (logging Units 4b, 5a, 5b, and 6, equivalent to lithostratigraphic Units III [lower part], IV, and V) consist of preglacial to early glacial sediments that have large gamma-ray fluctuations indicative of heavy mineral K, Th, and U contents associated in part with the high OC values here. These units also have lower velocity, density, and resistivity than the thick overlying deltaic sands of lithostratigraphic Unit III. All log traces show abrupt shifts at the logging Units 3/4 and 2/3 boundaries (equivalent to lithostratigraphic Units II/III and I/II boundaries) and are recognized as unconformities. The diamictons with interbedded glaciomarine clays and silts of lithostratigraphic Unit I have generally high and variable magnetic susceptibilities that suggest high variability in magnetite concentrations. FMS images clearly show the variability in

the lithostratigraphic units, the presence of lonestones, and the deformation of the organic-rich silt-sand horizons (lithostratigraphic Unit III). The resistivity and velocity logs, along with seismic reflection profiles, suggest the alluvial sands (Unit III) to glaciomarine diatom-bearing claystones (Unit II) transition represents a marine transgression.

Logging while drilling (LWD) was done in Hole 1166B to test the Power Pulse and compensated dual resistivity (CDR) tools and record spectral gamma-ray and resistivity data in the uppermost 42 m of the sediment. This interval could not covered by wireline logging because of the pipe position. Resistivity values increase in linear segments from near zero at the seafloor to the 3.5 Ωm values measured by the wireline logs at the base of the pipe.

A primary objective of Leg 188 was achieved when a set of cores that record intervals in the history of Antarctic paleoenvironments for the Prydz Bay region extending back through the early stage of glaciation to preglacial times was recovered at Site 1166. Drilling during Leg 119 in Prydz Bay recovered a record of early proximal glaciation at Sites 739 and 742 but did not capture the transition to warmer climates as would be indicated by the presence of local vegetation. Correlation of Site 1166 to Site 742 (~40 km apart) by comparison of downhole logs and regional seismic stratigraphy shows that Units I and II at Site 1166 are equivalent to (or older than) similar units at Site 742. Below the level of Unit II, however, Site 1166 samples are stratigraphically lower and record a more temperate alluvial facies than seen at Site 742. The lower part of Unit III (i.e., the deformed organic-rich sands and silts) may have been sampled in the lowermost 2 m of core at Site 742, but confirmation of this awaits further comparison of the two drill sites. If the organic units are the same, then a thick section of sands (Unit III) is missing at Site 742. The deepest unit at Site 1166 (Unit V) lies below a regional seismic unconformity that can be traced to Site 741, ~110 km away, where similar gray claystones like those of Unit V were also sampled. The age of the claystone at Site 741 is Early Cretaceous, which is preglacial.

The paleoenvironmental record inferred from the cores at Site 1166 shows a systematic uphole change from preglacial warm to full-glacial cold climates, such as that envisioned for the Prydz Bay region. The rich carbonaceous strata (undated Unit IV), which overlie Unit V, record a time of more temperate climatic conditions when vegetation existed on Antarctica. The sands (undated Unit III) of the alluvial plain environment may represent the transition into the progressively colder climates that are recorded in the proglacial (late Eocene to early Oligocene Unit II), glaciomarine (Unit II and late Pliocene and younger Unit I), and subglacial (Unit I) sediments. The ages of Units III and IV are late Eocene and Turonian, respectively (O'Brien et al., in press).

BACKGROUND AND OBJECTIVES

Prydz Bay is located at the downstream end of a drainage system that originates in the Gamburtszev Mountains of central East Antarctica (see Fig. F1, p. 29, in the "Leg Summary" chapter). Modeling studies of ice-sheet development indicate that the first glaciers in Antarctica would develop over these mountains, if the mountains were high in the Paleogene (e.g., Huybrechts, 1993). Glacier ice—and entrained debris—flowing down the drainage system would give the earliest sedimentary evidence of a large-scale ice sheet in East Antarctica. The early develop-

ment and growth of the Cenozoic Antarctic Ice Sheet is believed to have started by early middle Eocene to early Oligocene time (Abreu and Anderson, 1998; Barron et al., 1991); however, to date, drilling on the continent and the continental margin has not sampled a stratigraphic section that clearly spans and includes the transition period from preglacial to glacial conditions. Glacial deposits sampled at ODP Site 742 in eastern Prydz Bay were interpreted by Barron et al. (1991) as late middle Eocene to early Oligocene age. Cooper et al. (1991) estimated that these Paleogene sediments continued for 100 m below the total depth of Site 742 and rested above an erosion surface on older sediments. By drilling into the 100 m below Site 742 and into the sediments underlying the unconformity, the older age limit for large-scale glaciation of Prydz Bay could be derived. Sediments in the lower section of the hole would contain paleontological and sedimentological evidence of the preglacial environment.

Site 1166 is situated on the southwestern flank of Four Ladies Bank, ~40 km southwest of Site 742 in the zone of iceberg-scoured seabed mapped by O'Brien and Leitchenkov (1997) (Fig. F1). This site was chosen during Leg 188 after pack ice prevented access to preferred drill sites in western Prydz Bay. Site 1166 lies close to shotpoint 2050 on seismic line BMR 33-23P3. The expected section consists of 150- to 200-m-thick horizontally bedded glacigene diamictons of late Miocene to Pleistocene age, unconformably overlying ~150-m-thick Paleogene-age sediment, which in turn overlies Early Cretaceous–age nonmarine sediments (Fig. F2). The seismic line through Site 1166 shows three erosion surfaces (Fig. F2). The uppermost is the base of the upper horizontal sequence and truncates underlying units at a low angle. The second is an undulating surface in the probable Paleogene section that displays pronounced channeling toward north of the site (Fig. F2). The third surface delineates the top of the Lower Cretaceous sediments of unit PS.2B (Cooper et al., 1991) that were cored at Site 741 (ODP Leg 119). Line BMR 33-23P3 does not show truncation of underlying reflectors at the top of unit PS.2B near Site 1166; however, low-angle truncations can be seen on seismic lines from other parts of the basin.

F1. Location of Site 1166, p. 48.

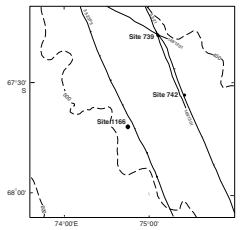

F2. Seismic line BMR 33-23P3 at Site 1166 showing major surfaces, p. 49.

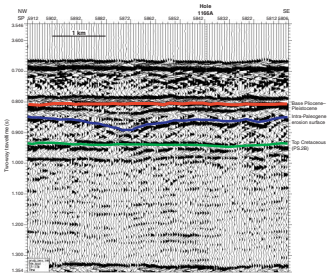

OPERATIONS

Transit to Site 1166

Based on satellite images from the National Ice Center (Washington, D.C.) and reports received from the *Hakurei-Maru,* a research vessel that had been operating in the area a week before our approach, it was unlikely that the primary shelf site (PBS-2A) would be ice free. Our plan was to locate the shelf site as far to the west as the ice would allow by heading for proposed site PBS-9A and to proceed from there to the west toward proposed sites PBS-8A, PBS-7A, and possibly PBS-1A. During the transit into Prydz Bay, with ice floes to either side of the vessel, it became clear that it was unlikely that sites farther to the west would be free enough of ice for drilling. The decision was therefore made to drill at site PBS-9A. Unfortunately, we discovered that a large iceberg was located directly over the selected drill site. As we were rapidly approaching our survey waypoint, we decided to move the site 3 nmi to the northwest along seismic line BMR 33-23P3. Permission for the new drilling location, named PBS-9B, was requested by telephone and fax and granted during approach to the site. A site survey was attempted

but ended before reaching the drill site because one water gun froze up and the other water gun broke an air hose. There was not enough time to fix these problems before nightfall, when the ship had to be on location because of numerous nearby icebergs and ice floes.

Site 1166

Hole 1166A

Hole 1166A was spudded with the rotary core barrel (RCB) at 0745 hr on 16 February. Continuous RCB coring proceeded to a depth of 199.5 mbsf (Tables T1, T2), when the passage of a large low-pressure system led to a deterioration of weather conditions and sea state. Drilling operations were halted at 2130 hr on 17 February because shallow-water operating guidelines went into effect, thereby limiting our operating environment to <2 m heave and wind gusts of <40 kt. When an iceberg came within 0.6 nmi of the ship, the decision was made to pull the drill string clear of the seafloor. A free-fall funnel could not be deployed because of the hard seafloor. The drill string was raised to a safe height, and the vessel was offset 1.0 nmi to avoid the iceberg that moved directly over the vacated drill site. After the iceberg and the low-pressure cell moved across Site 1166, conditions improved enough by 0630 hr on 19 February to deploy the subsea camera and reenter Hole 1166A. The reentry operation took only 13 min and was completed without the aid of a guide cone or funnel. A total of 38 hr was lost because of the storm.

The reentry showed that the seafloor was 6.7 m shallower than identified by the driller's blind tag with the bit at the start of the hole. Observations with the television camera showed a seafloor depth of 468.7 meters below sea level (mbsl). Corrections to the database were not performed (i.e., adding 6.7 m to all subsurface depths). Continuous RCB coring resumed and continued to a depth of 381.3 mbsf. Overall recovery for the hole was 18.6% (Tables T1, T2).

In preparation for logging, the bit was released, the hole was displaced with sepiolite logging mud, and the drill string was tripped to the logging depth of 48.0 mbsf. The hole was logged with a full suite of sensors (triple combo, FMS suite, and GHMT) from 33.0 to 377.3 mbsf. All logging runs were successful. By 0745 hr on 21 February, the logging sheaves had been rigged down and the wireline logging program was completed.

The hole was abandoned with a 21.5-bbl plug of cement, and the drill pipe was pulled clear of the seafloor and tripped back to the ship. At 1600 hr on 21 February, the rotary table was clear, ending Hole 1166A.

Hole 1166B

Hole 1166B was planned to gain LWD logs from the upper section of the hole that was not logged by wireline tools and to get downhole drilling parameters (e.g., weight on bit) in real time by measurement while drilling (MWD).

The drill string was tripped to bottom, and Hole 1166B was spudded at 0020 hr on 22 February. The seafloor depth was determined to be 482.5 mbsf, and the first hard layer was contacted at 485 mbsf. Drilling proceeded very slowly for the first 25 m. Very little weight could be put on the drill string until at least the measurement- and logging-while-

T1. Coring summary, p. 100.

T2. Expanded coring summary that includes length and depths of sections and comments on sampling, p. 101.

drilling (LWD/MWD) tools were buried beneath the seafloor. The hole was terminated at a depth of 40.0 m because the primary objectives of running LWD/MWD had been met and time restraints disallowed further logging.

The hole was displaced with heavy mud, and the drill pipe was pulled clear of the seafloor by 1020 hr. The beacon was released and recovered aboard at 1050 hr. The pipe was back aboard ship and the LWD/MWD tools were rigged down by 1330 hr on 22 February, and the *JOIDES Resolution* was under way for Site 1167.

LITHOSTRATIGRAPHY

Hole 1166A penetrated to a maximum depth of 381.3 mbsf, and a succession of poorly sorted sands, silt(stones), clay(stones), and diamictons was recovered. These sediments are divided into five lithostratigraphic units (Figs. F3, F4). The uppermost unit (Unit I) is composed of diamicton and poorly sorted clay and silt with dispersed clasts and is divided into four subunits. Unit II is composed of claystone and diatom-bearing claystone with sand beds. Unit III is characterized by coarse to very coarse sand supported by a silty clay matrix. Unit IV consists of stratified sandy silt and sand with organic detritus and black highly carbonaceous clay. Unit V consists only of a 16-cm-thick bed of gray claystone with thin planar laminations.

Unit I

Interval: Section 188-1166A-1R-1, 0 cm, through Section 15R-2, 136 cm
Depth: 0.0–135.41 mbsf
Age: Holocene to late Pliocene (0.0–3.2 Ma)

Unit I is composed of poorly sorted sediments with rare to abundant dispersed clasts. Four subunits are identified (Figs. F3, F4). Subunit IA is restricted to the uppermost 2.74 m of the hole and consists of poorly sorted diatom-bearing sandy silty clay with scattered rock clasts. Subunit IB is composed of diamicton. Subunit IC is characterized by interbedded poorly sorted sandy silt with lonestones along with diatom and diatom-bearing clayey silt containing dispersed granules and sand grains. Subunit ID is composed of diamicton and poorly sorted clayey sandy silt with dispersed clasts. The calcium carbonate content of Unit I ranges from 0.07–1.15 wt% (see "Organic Geochemistry," p. 31). A major unconformity occurs between Subunit ID and Unit II (see "Biostratigraphy and Sedimentation Rates," p. 17).

Subunit IA

Interval: Section 188-1166A-1R-1, 0 cm, through Section 1R-2, 124 cm
Depth: 0–2.74 mbsf
Age: Holocene

Subunit IA is composed of homogenous light brownish gray (5Y 4/1) diatom-bearing sandy silty clay with scattered pebble-sized rock clasts. Interval 188-1166A-1R-2, 72–73 cm, is composed of yellowish (5Y 4/3) diatom clay with spicules. Foraminifers are common in intervals 188-

F3. Lithostratigraphic units, subunits, and interpretation, p. 50.

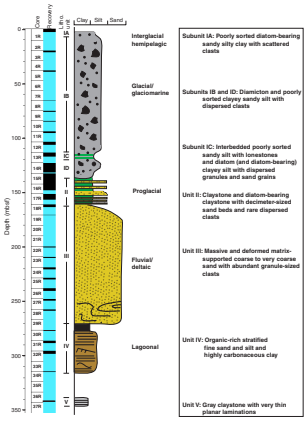

F4. Composite stratigraphic section, p. 51.

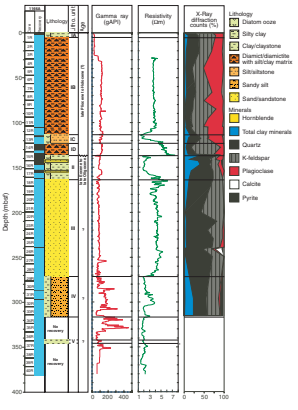

1166A-1R-1, 16–21 cm; 1R-1, 117–122 cm; and 1R-2, 9–12 cm (see "Biostratigraphy and Sedimentation Rates," p. 17). One large (3 cm × 4 cm) granite clast is present in interval 188-1166A-1R-2, 103–108 cm.

Subunit IB

Interval: Section 188-1166A-CC, 0 cm, through Section 12R-CC, 12 cm
Depth: 2.79–106.36 mbsf
Age: Holocene to late Pliocene

Subunit IB is composed of poorly sorted sediments with rare biogenic material. This subunit is characterized by interbeds of homogeneous dark gray (5Y 4/1) to black (5Y 2.5/2) clast-poor and clast-rich diamicton (Fig. F5). Spectrophotometer light reflectance was measured at 2-cm intervals to characterize the poorly sorted sediments cored at this site. The matrix content is predominantly clayey silt. The lithologies of the rock pebbles and rock granules are variable and include garnet-bearing quartzite, dolerite, diorite gneiss, granite, and rare sandstone. Garnet gneiss is a prominent component of pebbles and granules within this subunit. Clast-rich intervals include fibrous black organic clasts and pyrite granules. A large fractured granodiorite boulder is present within interval 188-1166A-3R-1, 0–31 cm. Planktonic foraminifers were identified in intervals 188-1166A-10R-1, 11–13 cm; 10R-CC; and 11R-1, 55–59 cm (see "Biostratigraphy and Sedimentation Rates," p. 17). A bone fragment was observed at Section 188-1166A-11R-1, 49 cm (see "Appendix," p. 46). Minor 1- to 2-cm-thick sand and granule beds are present within the diamicton in interval 188-1166A-11R-1, 71–84 cm.

Subunit IC

Interval: Section 188-1166A-13R-1, 0 cm, through Section 13R-3, 92 cm
Depth: 113.30–117.22 mbsf
Age: Pleistocene to late Pliocene

Subunit IC is characterized by interbedded dark gray (5Y 4/1) sandy silt with lonestones and greenish gray (5G 5/1) diatom and diatom-bearing clayey silt containing dispersed granules and sand grains and a few pebbles (Figs. F6, F7). Greenish gray biogenic-rich intervals are slightly bioturbated. Contacts between the dark gray sandy silt and the biogenic-rich greenish gray clayey silt are sharp. Soft-sediment deformation and flame-like structures are present at lithological contacts and within intervals of dark gray sandy silt.

Subunit ID

Interval: Section 188-1166A-14R-1, 0 cm, through Section 15R-2, 136 cm
Depth: 123.00–135.41 mbsf
Age: Pleistocene to late Pliocene

Subunit ID is composed of poorly sorted sediment with rare biogenic material. The upper portion of this subunit is characterized by interbeds of dark gray (5Y 4/1) clast-poor and clast-rich diamicton (interval 188-1166A-14R-1, 0 cm, to 14R-2, 60 cm; 123.00–125.10 mbsf). The lower

F5. Diamicton typical of Subunit IB, p. 52.

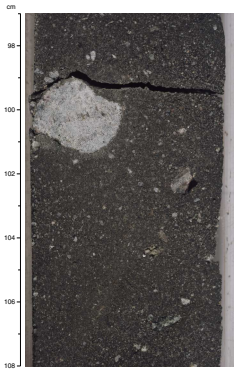

F6. Upper contact of interbedded clays and diatom clays of Subunit IC, p. 53.

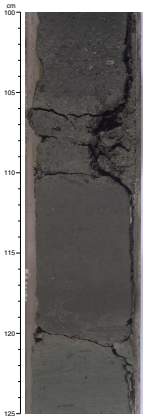

F7. Interbedded clays and diatom clays of Subunit IC, p. 54.

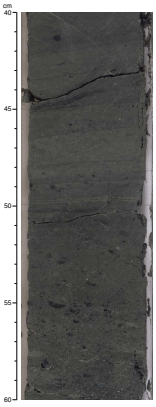

portion of this subunit is composed of dark gray (5Y 4/1) clayey sandy silt with dispersed rock clasts (interval 188-1166A-14R-2, 60 cm, to 15R-2, 136 cm; 125.10–135.41 mbsf). Minor 1- to 2-cm-thick sand and granule beds are present within the diamicton at Sections 188-1166A-14R-1, 52 cm; 14R-1, 56 cm; and 14R-1, 65 cm. Clast lithologies are variable and include gneiss, granite, and diorite rocks. An isolated mudstone clast is present in Section 188-1166A-14R-5, 59 cm. Black fibrous organic clasts and pyrite fragments are common in the diamicton.

Interpretation

The uppermost biogenic-rich interval of Subunit IA records iceberg-turbated hemipelagic sediments deposited on the outer continental shelf during Holocene interglacial conditions similar to the present day (O'Brien and Leitchenkov, 1997) (see **"Background and Objectives,"** p. 6). The presence of scattered pebble-sized clasts suggests deposition of IRD.

The diamicton and poorly sorted clayey sandy silt of Subunit IB suggest subglacial and proximal glaciomarine sedimentation. The rare broken and abraded microfauna contained within this subunit (see **"Biostratigraphy and Sedimentation Rates,"** p. 17) imply homogenization by subglacial deformation or redeposition of ice-proximal sediments. Intervals containing microfossils, shell fragments, and sand beds suggest current reworking and glaciomarine deposition. A major unconformity occurs at the base of Subunit ID (Section 188-1166A-15R-2, 136 cm; 135.41 mbsf) (see **"Biostratigraphy and Sedimentation Rates,"** p. 17; Fig. **F4**). Below the unconformity, XRD data show shifts in the relative abundances of mica, illite, hornblende, kaolinite, and plagioclase (Fig. **F7;** see **"X-Ray Diffraction Mineralogy,"** p. 15). These shifts within the XRD data suggest an increased amount of physically weathered terrigenous material within Unit I just above the unconformity. XRD data indicate the presence of gibbsite and kaolinite below the unconformity, within Unit II (Fig. **F4**). Both minerals indicate erosion of chemically weathered material formed in soils.

Soft-sediment deformation and flame-like structures at lithological contacts within Subunit IC suggest loading and rapid dewatering of the underlying sediments during abrupt fluctuations in the environmental setting. The interbedded sandy silt and biogenic-rich clayey silt of Subunit IC suggest fluctuations in the position of the ice margin. Periods of significant glacial retreat from the margin are marked by increased biogenic deposition. These periods are punctuated by deposition of pulses of coarse ice-proximal sediments. Lonestones within the sandy silt of Subunit IC may record deposition of IRD or glacial debris deposited beneath an ice shelf.

Unit II

Interval: Section 188-1166A-15R-3, 8 cm, through Section 17R-4, 77 cm
Depth: 135.63–156.45 mbsf
Age: early Oligocene to late Eocene

Unit II is composed of claystone and diatom-bearing claystone with decimeter-scale sand beds (Figs. **F3, F4**). The calcium carbonate content of Unit II ranges from 0.40 to 3.34 wt% (see **"Organic Geochemistry,"** p. 31).

The uppermost 17.24 m of Unit II (interval 188-1166A-15R-3, 8 cm, though 17R-1, 150 cm; 135.63–152.90 mbsf) is characterized by dark greenish gray (5GY 4/1) claystone and diatom-bearing claystone with numerous decimeter-thick light yellowish gray sand beds that contain dispersed rock clasts (<5 mm) (Fig. F8). Within interval 188-1166A-15R-3, 8 cm, to 17R-1, 150 cm (135.63–152.90 mbsf), the sands are poorly sorted. Moderate bioturbation is evident within both the claystone and sand beds. Diatoms are present in the lower portion of the unit in interval 188-1166A-15R-5, 67 cm, to 15R-6, 72 cm (see "Biostratigraphy and Sedimentation Rates," p. 17). Shell fragments are found within the greenish gray claystone beds in interval 188-1166A-16R-1, 64–65 cm, and at Section 16R-2, 43 cm. Trace amounts of glauconite are observed in a smear slide of interval 188-1166A-17R-1, 24 cm. Graded sand beds are present in intervals 188-1166A-15R-6, 59–65 cm, and 16R-2, 28–41 cm (Fig. F9). Rare fibrous, black organic clasts are observed within the sand beds.

The lowermost portion of Unit II (interval 188-1166A-17R-2, 0 cm, to 17R-4, 72 cm; 152.90–156.62 mbsf) is composed of centimeter-scale rhythmically interbedded sand and dark gray (5Y 4/1) claystone with dispersed clasts (Fig. F10). The clasts are angular to subangular and are present in both the claystone and the sand beds. Clast lithology is variable and includes metamorphic rocks, dark igneous rocks, and quartzite. Cross-stratification is found in the claystone beds (e.g., intervals 188-1166A-17R-2, 112–116 cm, and 17R-3, 9–14 cm). There is a change in lithology and color at the base of Unit II within a short interval of normal grading (interval 188-1166A-17R-4, 72–77 cm; 156.62–156.57 mbsf).

Interpretation

Unit II is a glaciomarine sequence that records proglacial sedimentation during a marine transgression. The marine transgression interpretation is based on an uphole transition from shallow-water glaciomarine facies to a dominance of diatom-bearing claystones deposited in an open marine environment. At Site 742 (Leg 119), Prydz Bay shelf sediments of similar or younger age (their Unit V) were sampled and the sediments were characterized by homogeneous diamictite (Shipboard Scientific Party, 1989c). The diamictite at Site 742 is interpreted as a proglacial or subglacial deposit. The sediments at Site 742 (Unit V) may be more similar to the lower section of Unit II at Site 1166 than their nomenclature suggests, because different sedimentological classification schemes were used during Legs 119 and 188 (see "Lithostratigraphy," p. 5 in the "Explanatory Notes" chapter) (Shipboard Scientific Party, 1989a).

Unit III

Interval: Section 188-1166A-17R-4, 77 cm, through Section 29R-1, 37 cm
Depth: 156.45–267.17 mbsf
Age: Eocene (see "Biostratigraphy and Sedimentation Rates," p. 17)

Unit III is composed of matrix-supported gray (5Y 5/1) coarse to very coarse sand with abundant granules (Fig. F11). The matrix is composed of silty clay. The calcium carbonate content ranges from 0.35–8.44 wt%

F8. Decimeter-scale interbedded clays and sands of Unit II, p. 55.

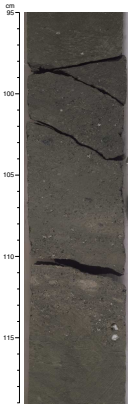

F9. Graded sand bed in the upper portion of Unit II, p. 56.

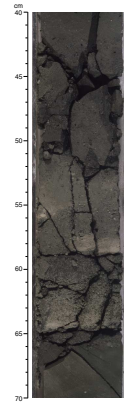

F10. Centimeter-scale interbedded clays and sands of Unit II, p. 57.

(see "Organic Geochemistry," p. 31). An isolated mud lamina is present within the uppermost portion of this unit at Section 188-1166A-17R-4, 81 cm. The remainder of Unit III appears ungraded. Rock clasts (>5 mm) are widely dispersed throughout this unit and are predominantly quartzite and garnet-bearing quartzite. Few fibrous, black organic fragments are present (see "Appendix," p. 46). Sand and silt grains are angular, whereas granules and pebbles are rounded. A sharp contact between overlying coarse sands and underlying very coarse sands occurs at Section 188-1166A-18R-2, 66 cm (163.16 mbsf), in the uppermost part of this unit. Unit III contains two cemented intervals: the first (interval 188-1166A-22R-1, 101–111 cm; 200.51–200.61 mbsf) is characterized by cemented medium to coarse olive-gray (5Y 5/2) sandstone with thin yellowish and dark brown color banding; the second (interval 188-1166A-26R-2, 70–86 cm; 240.10–240.26 mbsf) consists of cemented dark gray silty fine sandstone containing calcite cement.

The lowermost portion of Unit III is deformed and folded by soft-sediment deformation (interval 188-1166A-27R-1, 83 cm, through 29R-1, 37 cm; 248.43–267.17 mbsf) (Fig. F12). This interval is predominantly gray (5Y 5/1) in color; however, color banding (dark brownish gray, yellowish-bluish gray, light gray, and dark gray) is evident within deformed and folded regions. A deformed bed of black organic material is present in interval 188-1166A-28R-1, 36–60 cm (257.56–257.80 mbsf) (Fig. F13), and angular organic fragments are found within interval 188-1166A-28R-1, 59–62 cm (257.79–257.82 mbsf).

Interpretation

The coarse-grained sands of Unit III record deposition on an alluvial plain or delta. These sands are structureless and have a uniform silty clay matrix. The deformed beds of organic material within the lower portion of Unit III record some reworking of material from organic horizons within the alluvial plain or delta. A sequence of similar appearance was drilled in the last 2 m at Site 742 during Leg 119. Interlayered sands and siltstones and interbedded carbonaceous siltstones in the lowermost 2 m of Site 742 are also characterized by soft-sediment deformation (Shipboard Scientific Party, 1989c). These deformed sediments from Site 742 were tentatively interpreted as fluvial and possibly lacustrine; however, a sequence comparable to the homogeneous coarse sands in the upper two-thirds of Unit III at Site 1166 was not sampled at Site 742. Unit III may have been deposited in a proglacial outwash system similar to that of present-day southern Iceland and Alaska (Eyles and Eyles, 1992), or the sands may record a preglacial alluvial plain or braided delta.

Unit IV

Interval: Section 188-1166A-30R-1, 4 cm, through Section 34R-1, 101 cm
Depth: 276.44–314.91 mbsf
Age: Turonian (Late Cretaceous)

The topmost interval of Unit IV (interval 188-1166A-30R-1, 4–14 cm; 276.44–276.54 mbsf) is homogeneous black (5Y 2.5/1) highly carbonaceous clay. This bed is underlain by stratified sandy silt and sand with organic detritus, with rare to moderate bioturbation (Fig. F14). The stratified interval is characterized by decimeter-scale color alternations from

F11. Homogeneous coarse sands typical of the upper portion of Unit III, p. 58.

F12. Deformed coarse sands typical of the lower portion of Unit III, p. 59.

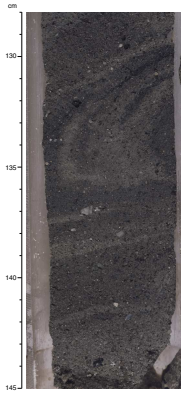

F13. Deformed sands and organic detritus within Unit III, p. 60.

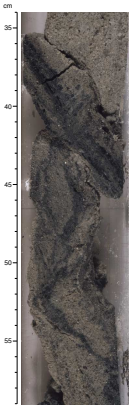

olive brown (2.5Y 4/4) to dark gray (N4) to black (2.5Y N2). The sandy silt contains abundant fine to medium sand-sized mica (Fig. F5) and rare pyrite nodules. Cross-lamination and disturbed and discontinuous laminae are common. A segment of structureless dark gray to black sandy silt with abundant sand-sized mica grains is present in interval 188-1166A-31R-1, 57–139 cm (286.57–287.39 mbsf). Siderite-cemented nodules are present within intervals 188-1166A-32R-1, 82–90 cm (296.12–296.20 mbsf); 32R-1, 96–100.5 cm (296.26–296.30 mbsf); and 32R-1, 114–117 cm (296.44–296.47 mbsf) (see "Physical Properties," p. 32). The calcium carbonate content within this unit ranges from 0.33–3.66 wt%. Organic carbon values of up to 5.2% are found in the carbonaceous bed (see "Organic Geochemistry," p. 31). Turonian palynomorphs were found in this unit (O'Brien et al., in press).

F14. Laminated micaceous silt and organic detritus typical of Unit IV, p. 61.

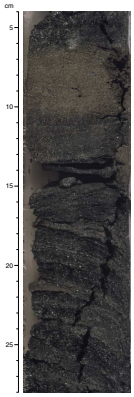

Interpretation

Unit IV records deposition within a restricted marine or lagoonal environment. Slow sedimentation rates under reducing conditions are indicated by the high organic carbon content and the presence of iron sulfides and preserved laminae. Disturbed and discontinuous laminations are common and may represent possible fluid escape structures.

Unit V

Interval: Section 188-1166A-37R-CC, 0–16 cm
Depth: 342.80–342.96 mbsf
Age: Turonian (Late Cretaceous)

Unit V consists of gray (5Y 5/1) claystone with thin light gray laminations and gray fine sandy silt. Only 16 cm of sediment (interval 188-1166A-37R-CC, 0–0.20 cm; 342.80–342.96 mbsf) was recovered from this unit.

Interpretation

It is premature to categorize the depositional environment based on sedimentological observations from 16 cm of core. Postcruise pollen analysis of Site 1166 core-catcher sediments indicates a Turonian age for these sediments. From regional seismic stratigraphic correlations, Unit V was recovered below a seismic unconformity that can be traced to Leg 119 Site 741, 110 km away. At Site 741, gray claystone deposits lithologically equivalent to Unit V (Site 1166) were observed. Pollen analysis of the fine-grained light gray siliciclastic sediments at Site 741 indicate an Early Cretaceous (Albian?) age. The sediments from Site 741 were interpreted as sediments deposited on a low-relief alluvial plain (Shipboard Scientific Party, 1989b), and a similar setting is likely for Unit V at Site 1166, although Unit V at Site 1166 is younger than the sediments at Site 741.

Smear-Slide Analysis

Smear slides were routinely prepared from the fine-grained matrix of silt and sand lithologies downhole. Diatoms, radiolarians, and sponge spicules are present only from 0 to 151.64 mbsf. Quartz is ubiquitous downhole, and no major fluctuations are evident. Heavy minerals such as amphibole are omnipresent in amounts of ≤5%, without a recogniz-

able trend in percentages. Feldspars were identified in a number of slides as minor components, but no significant trend emerged (e.g., Samples 188-1166A-6R-CC [47.30 mbsf]; 15R-6, 64 cm [140.69 mbsf]; 30R-1, 10 cm [276.50 mbsf]) (see "X-Ray Diffraction Mineralogy," p. 15) (Fig. F4). Coal and plant fragments are found in a few slides below 200 mbsf (e.g., Samples 188-1166A-22R-1, 62 cm [200.12 mbsf]; 23R-1, 69 cm [209.79 mbsf]).

A significant trend is discernible in mica (particularly muscovite) percentages. A plot (Fig. F15) of the combined percentages of muscovite and biotite shows that the total abundance remains <5% to a depth of 200 mbsf. In contrast, percentages increase sharply to the range of 20%–35% below 270 mbsf. The large size (up to sand size) of the mica flakes invariably leads to overestimates of mica abundance. Nevertheless, the overall trend is clear and is confirmed by XRD and chemical analyses (see "X-Ray Diffraction Mineralogy," p. 15, and "Inorganic Geochemistry," p. 29). A similar increase in opaque minerals below 270 mbsf is indicated by a few slides.

The high diatom content in the first few meters of Unit I (Subunit IA) reflects the marine origin of the sediment. Similarly, the marine or glaciomarine nature of the sediments of Subunit IC and Unit II is indicated by relatively high (up to ~20%) percentages of diatoms. This relatively high diatom content also causes the low grain densities and increased porosity of Unit II (see "Physical Properties," p. 32). The terrestrial (fluvial) to lagoonal depositional environments of Units III (lower part) through V are characterized by high mica content. Muscovite flakes are conspicuous and suggest derivation from granitic and/or gneissic bedrock lithologies in the source areas of the Lambert Glacier drainage system.

F15. Combined percentages of muscovite and biotite mica, p. 62.

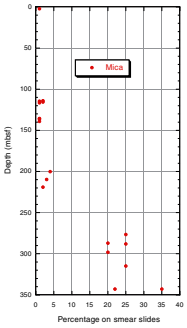

X-Ray Diffraction Mineralogy

At Site 1166, 32 samples were analyzed for bulk mineralogy and six samples were analyzed for clay minerals. The six clay-mineral samples were taken from clay and claystone, overlying clast-poor diamicton and clayey silt with dispersed clasts, and from two clayey matrix-rich sandstones in lower portions of the hole. The bulk mineral samples are primarily composed of quartz, plagioclase, K-feldspar, and a mixture of clay minerals, plus minor hornblende (Fig. F4). Total clay content in the upper 135 mbsf (Unit I) is lower than in deeper portions of the hole (Units II–IV); however, poor recovery, especially between 40 and 60 mbsf, makes determination of downhole trends difficult. The interval between 105 and 136 mbsf in Unit I has a slightly higher total clay content than sediments from the upper part of the hole. From 136 mbsf downhole, the relative abundance of plagioclase decreases as the abundance of clay minerals and quartz increases, except for a claystone-rich interval between 135.6 and 152.9 mbsf, where total clay content is higher compared to total quartz content. Downhole from 152.9 mbsf, the sediments show an increase in quartz content and plagioclase becomes a minor component; however, K-feldspar content remains constant to the bottom of the hole.

Four samples were taken from Cores 188-1166A-12R through 15R to determine clay mineralogy changes between Unit I and Unit II across the Neogene/lower Oligocene unconformity. A very fine grained diatom-bearing silty claystone at 114.73 mbsf in Unit I (Sample 188-1166A-13R-1, 143–145 cm) contains illite, very minor kaolinite and some clay-sized quartz, plagioclase, and K-feldspar (Fig. F16). The clay

F16. X-ray diffractograms of clay-sized fractions of sediment from Cores 188-1166A-12R and 13R, p. 63.

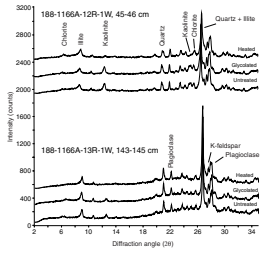

fraction of the overlying clast-poor diamicton (Sample 188-1166A-12R-1, 45–46 cm) has similar clay-mineral distribution to the claystone, but minor chlorite is also present and the illite content is relatively low (Fig. F16). The clayey silt with dispersed clasts of Unit I at 127.20 mbsf (Sample 188-1166A-14R-3, 120–121 cm) exhibits similar clay minerals as the sediments above, except the relative abundances of kaolinite and illite are higher and minor amounts of chlorite are present. In Unit II, an olive-green claystone directly below the upper Pliocene/lower Oligocene unconformity (Sample 188-1166A-15R-3, 24–25 cm) shows a distinctive change in clay-mineral content as kaolinite forms a major component with some mixed-layer clays and illite. Aluminum hydroxide is present in the form of gibbsite. After heating to 550°C, the kaolinite structure collapsed and gibbsite lost its water content and formed a new phase, as evidenced by the disappearance of distinctive peaks for these minerals on the diffractogram (Fig. F17).

The silty clay matrix of gray sand in Unit III at 219.77 mbsf (Sample 188-1166A-24R-1, 107–108 cm) contains predominantly kaolinite and a minor amount of clay-sized quartz and K-feldspar (Fig. F8). In the dark gray sandy silt at 295.55 mbsf (Sample 188-1166A-32R-1, 25–26 cm), the predominant clay mineral is kaolinite (Fig. F18). Minor gibbsite and clay-sized quartz are also present.

The presence of kaolinite and gibbsite in Unit II marine sediments suggests that the source rocks for these sediments were chemically weathered under a warm, temperate, humid climatic regime. In addition, an abundance of K-feldspar and absence of plagioclase in Unit II and older sediments may indicate chemical weathering of the source rocks. Increased humid conditions in East Antarctica are thought to have prevailed during the late Paleocene to early Eocene (e.g., Robert and Maillot, 1990). An absence of kaolinite in the upper Pliocene section suggests that less chemical weathering occurred in the sediment-source area. By the late Pliocene, most of the chemically weathered crust had been transported to depositional sites and less weathered or unweathered source rocks were exposed. Furthermore, the good preservation of chemical weathering indicators such as kaolinite and gibbsite, along with the absence of other clays in Unit II, may suggest that these components were not transported long distances or that proglacial conditions prevailed during Unit II deposition in the Lambert Glacier drainage system. Cold climatic conditions are characterized by illite- and chlorite-dominated clay mineral assemblages observed in the upper Pliocene.

Environmental Interpretation

Despite poor recovery (18.6%) at Site 1166, sediments cored at this site reveal important insights into the sedimentary history of the Prydz Bay outer continental shelf. Unit I records a period of proximal and distal glaciomarine sedimentation on the shelf from the late Pliocene to Holocene. The youngest sediments recovered record interglacial hemipelagic sedimentation subjected to subsequent reworking by iceberg turbation. Periods of proximal glaciomarine and possibly subglacial conditions are recorded within Subunits IB and ID. Intervals of glacial retreat and advance can be identified within the glaciomarine sediments of Subunit IC.

A major unconformity exists between the Pliocene sediments in Unit I and the underlying lower Oligocene/upper Eocene sediments of Unit II. A marine transgression is recorded in the proglacial clays and sands

F17. X-ray diffractograms of clay-sized fractions of sediment from Cores 188-1166A-14R and 15R, p. 64.

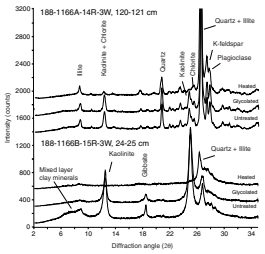

F18. X-ray diffractograms of clay-sized fractions of sediment from Cores 188-1166A-24R and 32R, p. 65.

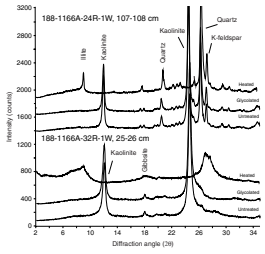

of Unit II, and this early Oligocene- to late Eocene-age event may have been close to the time of the onset of continentwide ice-sheet development in Antarctica. The initial transgression is likely recorded in the uppermost sands of Unit III (see "Downhole Measurements," p. 36), culminating in a maximum flooding surface in Unit II. Homogeneous diamictites of similar or slightly younger age (Oligocene to Eocene) than Unit II sediments were penetrated at Site 742 during Leg 119 (Shipboard Scientific Party, 1989c). The diamictites at Site 742 were interpreted as a proximal glaciomarine deposit (Shipboard Scientific Party, 1989c), which is consistent with a proglacial shallow marine interpretation for the sediments observed at Site 1166.

The fluvial-deltaic sands of Unit III may record a downhole transition to sediments deposited in warmer, more temperate conditions in Prydz Bay. The deformed beds of organic material within the lower portion of Unit III resemble the deformed interlayered sands and siltstones drilled in the lowermost 2 m at the base of Site 742 during Leg 119. If the lowermost 2 m at Site 742 is equivalent to the lowermost part of Unit III at Site 1166, then the overlying thick coarse sands sampled at Site 1166 are missing at Site 742. The coarse sands at Site 1166 may indicate a preglacial or early glacial alluvial plain or braided delta. Alternatively, the Unit III deposits recovered at Site 1166 may record a more complete distal glacial outwash system.

Unit IV records deposition within a restricted marine or lagoonal environment. Palynomorphs indicate a Late Cretaceous (Turonian) age. The 16 cm of recovered sediments within Unit V makes interpretation of depositional processes and paleoenvironment speculative; however, the laminated gray claystone of Unit V resembles Lower Cretaceous preglacial fluvial deposits recovered at Site 741 during Leg 119 (Shipboard Scientific Party, 1989b).

BIOSTRATIGRAPHY AND SEDIMENTATION RATES

Introduction

Hole 1166A samples a section of ~360 m that is divided into five primary lithostratigraphic units. Fossil recovery is sporadic through the drill core, and well-constrained biostratigraphic age control is presently limited to narrow intervals. Units I and II are assigned Quaternary–late Pliocene and early Oligocene–late Eocene ages, respectively. Unit III contains late Eocene palynomorphs and Units IV and V contain Late Cretaceous (Turonian) pollen.

Unit I (0 to ~135 mbsf) is subdivided into four lithostratigraphic subunits. Subunit IA consists of poorly sorted sandy silty clay that is Holocene to possibly late middle Pleistocene in age. Subunit IB consists largely of diamicton and is assigned a broad age of Quaternary to late Pliocene because of poor biostratigraphic control. Subunit IC consists of interbedded poorly sorted sandy silt with lonestones and diatom-bearing clayey silt with dispersed granules and sand grains of late Pliocene age. Subunit ID consists of unfossiliferous diamicton and is not biostratigraphically constrained.

Unit II (~135 to ~160 mbsf) consists of interbedded diatom-bearing claystones and sands. Rich diatom assemblages recovered in this interval are assigned an age of earliest Oligocene–late Eocene.

Units III and IV (~160 to ~315 mbsf) contain sand, silt, and clay and include plant material and coal. No macrofossil material was identified in Unit V (~342.8–342.96 mbsf).

Numerous shipboard samples were taken from Units II–V (~135–343 mbsf) for shorebased palynological investigation. Well-preserved pollen and dinocryst assemblages were observed in initial analysis of this material. Detailed palynological results and age interpretations from Hole 1166A will be available in the *Scientific Results* volume and/or journal publications. Preliminary results give good age indications for these units.

Biostratigraphic zonal assignments and paleoenvironmental interpretations for Site 1166 are based on shipboard analysis of diatoms, radiolarians, foraminifers, and calcareous nannofossils. The results of these initial investigations are summarized in Table **T3** and Figure **F19** and are described below.

T3. Diatom and radiolarian biostratigraphic datums from Hole 1166A, p. 102.

F19. Core recovery, lithostratigraphic units, magnetostratigraphy, and biostratigraphic zones for Hole 1166A, p. 66.

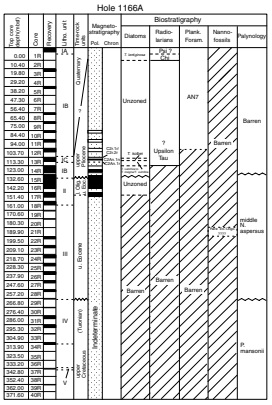

Planktonic Foraminifers

Introduction

The Neogene section in Hole 1166A yielded moderately abundant faunas of planktonic foraminifers from Cores 188-1166A-1R through 12R. Samples 188-1166A-1R-CC, 2R-CC, and below 11R-CC are barren of foraminifers.

Planktonic faunas are dominated by *Neogloboquadrina pachyderma* (Ehrenberg), indicating that the entire section down to Sample 188-1166A-12R-1, 18–20 cm, is upper Miocene or younger (*N. pachyderma* Zone AN7, of Berggren et al., 1995). These faunas are those commonly found on a fully marine open shelf. Dissolution of specimens is not evident, but some specimens of *N. pachyderma* from the shallower parts of the section have some physical abrasion. Other than the abrasion, there is no evidence of reworking or biostratigraphic mixing of faunas.

Planktonic foraminifers are relatively common (several tens of specimens) in samples from Sections 188-1166A-1R-1 and 1R-2 but not from Sample 188-1166A-1R-CC. Four- and five-chambered forms of *N. pachyderma* were recorded separately in this interval. Planktonic foraminifers are also present but much less abundant in Section 188-1166A-3R-2 (base of section), where few specimens of *N. pachyderma* (Ehrenberg) are present, and in Sample 188-1166A-4R-CC. These specimens are gray in color and are slightly abraded but do not show any evidence of dissolution.

Both four- and five-chambered forms of *N. pachyderma* are dominant in Sample 188-1166A-5R-CC. This association is common in modern shelf faunas in the region (Quilty, 1985).

Samples 188-1166A-6R-CC, 7R-CC, and 9R-CC contain *N. pachyderma,* with or without *Globigerina falconensis,* but in low abundance. Sample 188-1166A-8R-CC is barren of foraminifers.

Several samples from Samples 188-1166A-5R-CC through 10R-CC contain small planktonic species in the 63- to 125-µm fraction.

Samples 188-1166A-10R-1, 11–13 cm; 10R-CC; 11R-1, 47–50 cm; and 11R-CC contain relatively diverse planktonic foraminiferal faunas, the best available in the Neogene at this site. These assemblages are dominated by the normal four-chambered form of *N. pachyderma,* and a few five-chambered forms are present. A small five-chambered form of *Globorotalia* (*Tenuitella*) (sensu Kennett and Srinivasan, 1983) is repre-

sented by several specimens, and a single specimen of *Globigerinita parkerae* (Bermudez) was recorded.

The deepest sample in Hole 1166A bearing planktonic species is Sample 188-1166A-12R-1, 18–20 cm. It contains a few specimens of *N. pachyderma*.

Samples of *N. pachyderma* and shell fragments from Sample 188-1166A-11R-1, 47–50 cm, have been selected for Sr dating and will provide adequate material for oxygen isotope studies.

Benthic Foraminifers

The Neogene section in Hole 1166A yielded moderately abundant benthic foraminifers from Core 188-1166A-1R to Sample 188-1166A-12R-1, 18–20 cm.

The records presented here are likely to underestimate the benthic foraminiferal fauna because more delicate agglutinated forms (e.g., what appears to be *Haplophragmoides* sp.) were observed during examination of sediment samples under hand lens and stereobinocular microscope. These do not survive vigorous processing. Only the more robust forms were therefore recorded.

Benthic faunas are dominated by members of the Cassidulinacea (forms with granular crystalline walls): *Globocassidulina, Cassidulina,* and *Ehrenbergina*. Lagenid/nodosariid forms are absent, and other forms are rare. Three species of *Globocassidulina* are recognized here: *Globocassidulina crassa* (d'Orbigny), *Globocassidulina subglobosa* (Brady), and *Globocassindulina biora* (Crespin). The latter of these species is here classed as a separate species rather than incorporated into *G. crassa,* as was done by Milam and Anderson (1981).

Although Sample 188-1166A-1R-CC was barren of foraminifers, scattered specimens of *Globocassidulina* are present throughout the length of Core 188-1166A-1R. These are present in the lowest abundance of the three species recognized. Selected samples from this core, such as Samples 188-1166A-1R-1, 16–21 cm; 1R-1, 117-122 cm; and 1R-2, 9–11 cm, all contained benthic faunas, including sporadic specimens of *Angulogerina earlandi* (Parr).

Small faunas are present in Section 188-1166A-3R-2 (base of section) and in Samples 188-1166A-4R-CC; 5R-1, 26–31 cm; 5R-CC; 6R-CC; 7R-CC; 8R-1, 42–45 cm; and 9R-CC. Samples 188-1166A-10R-1, 11–13 cm; 10R-CC; and 11R-1, 47–50 cm, however, contain much larger, more diverse benthic faunas.

Several samples contain *Uvigerina bassensis* (Parr), which is present as single gray and slightly abraded specimens. It likely came from the same source as the planktonic specimens in these samples. The presence of the uvigerinids is evidence of some infauna, but their numbers are too low to draw meaningful conclusions about environmental significance.

Sample 188-1166A-10R-CC contained two species of *Astrononion* in addition to the species discussed in the preceding paragraphs.

Paleoenvironment in the Neogene

Several samples contain enough foraminifers to allow planktonic percentage to be used as a depth indicator. Planktonic percentage in these samples is ~50%–80%, suggesting water depths corresponding to the outer continental shelf or deeper. Faunas with high globocassidulinid content (especially *Globocassidulina*) are widespread in the mod-

ern Prydz Bay in shallower, better oxygenated environments such as the Four Ladies Bank (Quilty, 1985). The outer continental shelf association also is consistent with the deep-shelf calcareous assemblage of Milam and Anderson (1981). These faunas are not expected from samples representing deeper parts of the region where siliceous mud and ooze (SMO of Harris et al., 1997) dominate. The agglutinated fauna normally found in SMO was not indicated in any of the faunas studied from Site 1166. A solitary sample, Sample 188-1166A-13R-1, 71–73 cm, contains a very small >63-µm residue—typical of that from SMO samples. This sample, however, yielded no foraminifers.

Two predominant lithologies are identified in Neogene cores at this site: massive diamicts and silty clays. An attempt was made to relate foraminiferal faunas to these different lithologies, but the faunal distributions bear little relationship to the lithologic changes.

On the basis of foraminiferal faunas, the Neogene section can be divided into three intervals:

1. Top of Core 188-1166A-1R down to Sample 188-1166A-1R-2, 9–12 cm, with common and diverse foraminiferal faunas, both planktonic and benthic;
2. Samples 188-1166A-1R-CC through 9R-CC, consisting of barren zones with few foraminifers; and
3. Samples 188-1166A-10R-1, 11–13 cm, through 11R-CC, in which foraminifers are abundant and diverse.

Calcareous Nannofossils

Nearly all core-catcher samples from Cores 188-1166A-1R through 39R were barren of calcareous nannofossils. Sample 188-1166A-21R-CC contained a very rare, poorly preserved specimen of a middle Eocene to earliest Miocene taxon, *Reticulofenestra daviesii*. A single specimen of *Coccolithus pelagicus* and two heavily overgrown specimens of *Reticulofenestra* sp. were also noted. It cannot be determined whether these specimens are in situ, reworked, or possible contaminants. A probable contaminant specimen of the Oligocene–Miocene taxon, *Reticulofenestra hesslandii,* was also noted in Sample 188-1166A-31R-CC.

The absence of nannofossils at this locality is consistent with that reported by Wei and Thierstein (1991) for the lower part of the nearby Prydz Bay Site 742 (Shipboard Scientific Party, 1989c; ODP Leg 119). Diatoms are present in the upper part of the section in Hole 1166A, which indicates that conditions were conducive to marine phytoplankton productivity at this site through at least some intervals of the late Eocene–earliest Oligocene and Pliocene. However, during these periods, nearshore surface waters were not favorable for nannoplankton production.

Diatoms

Introduction

Quaternary, Pliocene, and lowermost Oligocene–upper Eocene diatom assemblages are recognized in Hole 1166A. Fossil diatom occurrence, however, is generally sporadic throughout the section, with abundant and well-preserved assemblages present only in limited intervals.

Initial biostratigraphic analysis for diatoms was carried out primarily on core-catcher samples. Because of a high degree of lithologic varia-

tion over narrow intervals (see "Lithostratigraphy," p. 9), discrete core intervals containing fine-grained sediments were preferentially sampled in an effort to identify more fossiliferous horizons. Coarser grained facies were also examined in some intervals, but these samples generally contained very rare poorly preserved diatoms.

Three distinct siliceous microfossil assemblages are noted in Hole 1166A: Quaternary sediments were recovered in Core 188-1166A-1R, upper Pliocene marine diatoms are present in two silt beds interbedded with poorly sorted silts with lonestones in Core 188-1166A-13R, and lowermost Oligocene–upper Eocene marine sediments are identified in Cores 188-1166A-15R and 16R. A major disconformity (~30 m.y.) within Section 188-1166A-15R-2 is interpreted to separate upper Pliocene and lowermost Oligocene–upper Eocene strata.

Below Sample 188-1166A-17R-2, 58–59 cm (153.48 mbsf), no diatoms were recovered. Diatoms may be absent in this interval because of a lack of marine diatom productivity during deposition or because of dissolution. Alternatively, these strata represent estuarine or nonmarine facies deposited in an environment not inhabited by diatoms.

The diatom zonation of Harwood and Maruyama (1992) and Winter and Harwood (1997) was applied to Quaternary and Pliocene cores of Hole 1166A, and the Paleogene cores are currently left unzoned. Diatom zonal datums recognized in Hole 1166A are listed in Table T3.

Quaternary Assemblages

Core 188-1166A-1R is characterized by silt-rich sediments that contain poorly preserved diatoms; however, an abundant and well-preserved diatom assemblage is present in a biosiliceous sponge-spicule horizon in Sample 188-1166A-1R-2, 72–73 cm (2.22 mbsf). This assemblage consists entirely of extant Southern Ocean diatoms. The absence of the fossil species *Actinocyclus ingens* in this sample (last occurrence [LO] = 0.66 Ma) indicates that the interval above 2.22 mbsf is within the Holocene–middle to upper Pleistocene *Thalassiosira lentiginosa* Zone. This sample also contains abundant sea ice–associated *Fragilariopsis curta,* which is abundant in modern surface-sediment samples near Site 1166 (Stockwell et al., 1991; Taylor et al., 1997).

Moderately abundant and well-preserved diatoms are present in Sample 188-1166A-1R-CC (3.02 mbsf). This sample is also assigned to the *T. lentiginosa* Zone, based on the absence of *A. ingens*. Diatoms in this sample represent an extant assemblage, except for the common occurrence of well-preserved *Thalassiosira torokina* ("late" form). The LO of this taxon is documented at 1.8 Ma in the Southern Ocean (Harwood and Maruyama, 1992) but is known to range into the *T. lentiginosa* Zone (0–0.66 Ma) in the CRP-1 drill core in the southeastern Ross Sea (Bohaty et al., 1998). The observed occurrence of *T. torokina* in *T. lentiginosa* Zone sediments in Hole 1166A and CRP-1, therefore, represents a diachronous LO between Antarctic shelf (Prydz Bay and Ross Sea) and Southern Ocean (Kerguelen Plateau) locations. At the current time, the presence of *T. torokina* in this sample can be taken only to indicate that the assemblage is not entirely extant.

The absence of *Rouxia* spp. in Samples 188-1166A-1R-2, 72–73 cm, and 1R-CC further suggests a latest Quaternary age for this interval. The LO of *Rouxia* spp., however, on the Antarctic shelf is not well constrained. Bohaty et al. (1998) record the presence of *Rouxia leventerae* in (lower?) *T. lentiginosa* Zone sediments in the CRP-1 drill core. In Southern Ocean sections, Abbott (1974) and Akiba (1982) document a LO of

Rouxia spp. at ~0.35 Ma and Pichon (1985) notes a LO within Stage 6 (~0.15 Ma).

Sample 188-1166A-1R-CC contains more abundant *Fragilariopsis kerguelensis* specimens than are found in surface sediments near Site 1166 today. This could represent either more open-water conditions or an increase in the influence of winds affecting the Prydz Bay gyre that may have pushed the open-water assemblage farther into the shelf than today.

Site 1166 was overridden by grounding ice during the last glacial maximum (LGM) (Domack et al., 1998). The change in diatom assemblages between the sandy silty clay above 2.92 mbsf (e.g., Sample 188-1166A-1R-2, 72–73 cm [2.22 mbsf]) and the diamict below (e.g., Sample 188-1166A-1R-CC [3.02 mbsf]) may represent a disconformity as a result of this glacial advance. If this is the case, the sandy silty sediment above 2.92 mbsf represents deposition since the LGM.

Diatoms are low in abundance and are predominantly broken within diamict between 3.02 and 113.84 mbsf. These may be glacially reworked diatoms in lodgment till, or alternatively, they could be reworked or deposited in situ within waterlain till. Detailed sedimentological analysis may enable identification of these facies and allow comment on the mode of diatom deposition. Nevertheless, the presence of diatoms within the diamict helps constrain the age of these deposits. Sample 188-1166A-2R-CC (10.64 mbsf) contains *F. kerguelensis* (first occurrence [FO] = 3.1 Ma), indicating that the diamict above 10.64 mbsf is <3.1 Ma in age. Further work on rare diatoms in Sample 188-1166A-12R-CC (106.37 mbsf) may also provide biostratigraphic information enabling age constraint for the diamicts above this level.

Pliocene Assemblages

Upper Pliocene marine diatoms are present in two greenish gray silt horizons in Core 188-1166A-13R that are interbedded with poorly sorted sandy siltstones. The lighter gray-colored silt horizons in this core contain abundant and well-preserved diatoms (e.g., Samples 188-1166A-13R-1, 70–71 cm [114.00 mbsf]; and 13R-2, 8–10 cm [114.88 mbsf]). The upper silt bed (~113.95 to ~114.10 mbsf) is placed within the *T. kolbei* Zone of Harwood and Maruyama (1992), as indicated by the presence of *T. kolbei* (LO = 1.9 Ma) and the absence of *T. vulnifica* (LO = 2.3 Ma). *T. kolbei* Zone sediments were previously recovered nearby from Site 742 (Mahood and Barron, 1996) and may represent a correlative horizon to that recovered in Hole 1166A.

The age of the lower silt bed (~114.50 to ~115.15 mbsf) is constrained by the presence of *T. vulnifica* (FO = 3.2 Ma). In the Southern Ocean zonal scheme, the full range of *T. vulnifica* represents the top of the *T. vulnifica* Zone and the base of the *Thalassiosira insigna–T. vulnifica* Zone (of Harwood and Maruyama, 1992). The presence of *T. insigna* would further indicate that the *T. vulnifica* Zone is disconformably absent, placing this interval in the *T. insigna–T. vulnifica* Zone. The absence of the subzonal datum *Fragilariopsis weaveri* (LO = 2.8 Ma) also constrains this interval to the *T. insigna–T. vulnifica* Subzone "b." The absence of the *T. vulnifica* Zone, therefore, suggests a disconformity between ~114.10 and ~114.50 mbsf. Sharp lithologic contacts occur with changes in grain size at 114.40 mbsf and sediment color at 114.50 mbsf; these levels may represent erosive events indicated by the absence of the *T. vulnifica* Zone.

The full range of *T. vulnifica,* alternatively, represents the top of the *T. vulnifica* Zone and the base of the *T. striata–T. vulnifica* Zone, which is defined from Antarctic Shelf cores in the Ross Sea (Winter and Harwood, 1997). These zones are divided by the LO of *T. striata*. Using this zonation, the absence of *T. striata* and the presence of *T. vulnifica,* therefore, place the interval between ~114.50 and ~115.15 mbsf within the *T. vulnifica* Zone (of Winter and Harwood, 1997), indicating that the "upper" and "lower" silt horizons are conformable.

The conflict between the two zonal interpretations for the "lower" silt bed arises from the biostratigraphic application of the LO of *T. insigna*. The range of this taxon does not overlap with *T. vulnifica* in the Ross Sea but does so in the Southern Ocean (Winter and Harwood, 1997) and in Hole 1166A. In Hole 745B (ODP Leg 119), the LO of *T. insigna* occurs above the LO of *T. vulnifica* (Baldauf and Barron, 1991). Further work is required to investigate the biostratigraphic range of *T. insigna* and validate its use as a zonal marker. Additionally, some taxonomic confusion exists between *T. insigna* and other morphologies, such as *Thalassiosira insigna/inura* (transitional form), which was observed as high as 114.00 mbsf (Sample 188-1166A-13R-1, 70–71 cm) within *T. kolbei* Zone sediments. Diatoms similar in appearance to *T. insigna/inura* (transitional form) were also illustrated from the *T. kolbei* Zone of Hole 742A but were included under the designation of *Thalassiosira oliverana* (Mahood and Barron, 1996).

Thalassiosira elliptipora also appears to have a different range on the Antarctic shelf than in more northerly deep-sea sections. On the Kerguelen Plateau, the FO is nearly contemporaneous with the LO of *T. vulnifica* at 2.3 Ma (Harwood and Maruyama, 1992). At Site 1166, however, *T. elliptipora* occurs in moderate abundance within the range of *T. vulnifica*. This is consistent with observations from the Ross Sea, where the range of *T. elliptipora* is entirely within the *T. vulnifica* and *T. striata–T. vulnifica* Zones (Winter and Harwood, 1997)

From preliminary observations, the upper Pliocene diatom assemblages in Hole 1166A appear to contain a relatively higher component of *Eucampia antarctica* var. *recta* winter intercalary valves than winter terminal valves. The opposite is found in Prydz Bay today (Fryxell, 1991). The ratio between these valves has been used to reconstruct winter sea-ice conditions in marine sediments from the Kerguelen Plateau (Kaczmarska et al., 1993). At Site 1166, this ratio may suggest a lower winter sea-ice concentration during the late Pliocene than today. Also consistent with this observation is a low relative abundance of the sea-ice-associated taxon *F. curta,* which suggests a lower summer sea-ice concentration than today.

An interval of diamict is present between Samples 188-1166A-14R-CC (131.88 mbsf) and 15R-2, 118–120 cm (135.23 mbsf). This interval is barren of diatoms and consequently has been left unzoned.

Oligocene–Eocene Assemblages

A major change in lithology and mineralogical composition (see **"Lithostratigraphy,"** p. 9) occurs at Section 188-1166A-15R-2, ~8 cm (~135.65 mbsf); this level is interpreted as representing a major disconformity. Abundant and well-preserved lowermost Oligocene–upper Eocene diatom assemblages occur below this level between 135.73 and 151.60 mbsf.

The diatom assemblage between the lower part of Core 188-1166A-15R and the upper part of Core 17R is characterized by the presence of

the following taxa: *Distephanosira (Melosira) architecturalis, Eurossia irregularis, Hemiaulus caracteristicus, Hemiaulus dissimilis, Hemiaulus incisus, Kannoa hastata, Pterotheca danica, Pyxilla reticulata, Stictodiscus kittonianus, Stephanopyxis grunowii, Stephanopyxis oamaruensis, Stephanopyxis splendidus, Stephanopyxis superba,* and *Vulcanella hannae*. In addition, a number of characteristic ebridian, silicoflagellate, and chrysopphytecyst taxa were identified in this assemblage, including *Archaeosphaeridium tasmaniae, Archaeosphaeridium australensis, Ammodochium ampulla* (double loricate skeleton), *Ebriopsis crenulata* (loricate skeleton), *Ebriopsis crenulata* (nonloricate skeleton), *Ebrinula paradoxa, Parebriopsis fallax,* and *Pseudammodochium dictyoides* (single skeleton).

The age of the interval between 142.45 and 148.26 mbsf is partially constrained by the presence of *H. caracteristicus,* which indicates an age of greater than ~33 Ma, based on its LO within Chron C13n in Hole 744B on the southern Kerguelen Plateau (Baldauf and Barron, 1991). The absence of several taxa characteristic of the middle Eocene, such as *Trinacria cornuta* and *Craspedodiscus moellerii* (Gombos, 1983), further suggests a lower age limit of less than ~37 Ma. The lowermost Oligocene–upper Eocene section of Hole 1166A is left unzoned at the present time; there are very few Southern Ocean reference sections that contain well-preserved middle to upper Eocene diatom assemblages, and zonal schemes are under development.

Similar lowermost Oligocene–upper Eocene assemblages are present in the interval from ~366 to ~500 mbsf in the CIROS-1 drill core in McMurdo Sound (Harwood, 1989) and in Hole 739C in Cores 119-739C-25R through 38R in Prydz Bay (Barron and Mahood, 1993; Mahood et al., 1993). Siliceous-microfossil taxa common to assemblages in all three of these sections include *E. crenulata* (loricate skeleton), *E. irregularis, H. caracteristicus, Kisseleviella* sp. G (of Scherer et al., in press), *P. dictyoides* (single skeleton), *P. danica, S. splendidus, S. kittonianus,* and *V. hannae*. The assemblage present in Hole 1166A, however, does not contain *Rhizosolenia oligocaenica, Skeletonema utriculosa, Skeletonemopsis mahoodii,* or *Sphynctolethus pacificus,* which are present in CIROS-1 and in Hole 737C. This suggests the interval recovered in Hole 1166A may be slightly older than the CIROS-1 and Hole 739C sections. The presence of *Pseudorutilaria monile* (absent in CIROS-1 and Hole 739C) and the common presence of *P. danica* and *D. architecturalis* further support this assumption, but further detailed analyses of additional samples will be required to completely characterize the assemblage and confirm the absence of specific taxa in Hole 1166A.

Lowermost Oligocene–upper Eocene assemblages documented in Cores 188-1166A-15R through 17R are almost exclusively neritic/planktonic in character, suggesting paleowater depths of >50 m. Additionally, the high abundance of planktonic diatoms, particularly in Samples 188-1166A-15R-CC and 188-1167A-16R-4, 130–131 cm, indicates an open-marine environment. The high biogenic opal content of these sediments also suggests that the surface-water conditions were euphotic and that turbidity, due to terrigenous sediment influx, was low. These conditions differ from those in a marine setting proximal to river mouth or polythermal/wet-based glaciers, which would be influenced by a high sediment influx. Diatom assemblages in this interval, therefore, indicate that the site was located at a distal position relative to the ice margin—that is, if glaciers were present at the time of deposition.

Radiolarians

Radiolarian faunas are present in only a few samples in Hole 1166A. The radiolarian zones proposed by Lazarus (1990, 1992) for Neogene high-latitude sections (see **"Radiolarians,"** p. 15, in the "Explanatory Notes" chapter) were applied to the radiolarian-bearing samples from this hole. The radiolarian zones and associated datums recognized in Hole 1166A are outlined in Table **T3** and Figure **F19.**

Sample 188-1166A-1R-2, 70–72 cm, contains moderately preserved radiolarians and is assigned to the Chi to Psi Zones (1.9–0.0 Ma). *Triceraspyris antarctica* (Haecker) and *Lithelium nautilodes* Popofsky both appear in the lower part of the Chi Zone (Lazarus, 1992), and both taxa are common in this sample. Absent from the sample, however, are *Cycladophora pliocenica,* which has a LO in the middle of the Chi Zone, and *Pterocanium c. trilobum,* which has a LO at the top of the Chi Zone (or bottom of the Psi Zone), thus suggesting that this sample could be constrained to the Psi Zone. Also present in this sample are *Spongotrochus*? *glacialis, Antarctissa denticulata, Antarctissa cyclindrica,* and *Phorticum clevei,* all high-latitude species consistent with assignment to the Chi and/or Psi Zones.

Radiolarians in Samples 188-1166A-13R-1, 150 cm, and 13R-2, 5 cm, are very rare and poorly preserved, but *Antarctissa strelkovi* is present. This taxon ranges from the base of the Tau Zone (6.1 Ma) to the top of the Upsilon Zone (2.4 Ma); therefore, these samples are assigned to the Tau or Upsilon Zones (Lazarus, 1992).

It is not likely that radiolarian biostratigraphic resolution will improve in Hole 1166A, as the more promising samples from within the core have already been processed (e.g., 15 samples from Cores 188-1166A-1H, 13H, and 15H) and are barren of radiolarians.

Palynology

Preliminary palynological examination of Site 1166 found palynomorphs of the middle *Nothofagidites aspersus* Zone of the Gippsland Basin of southeastern Australia in Units II and III and of the *Phyllocladidites mawsonii* Zone from the Gippsland Basin in Units IV and V (O'Brien et al., in press). These palynomorphs date Units II and III as mid to late Eocene and Unit IV as Turonian. Additionally, Unit V is of Turonian-Santonian(?) age.

Paleontological Summary

Initial micropaleontological analysis of Hole 1166A was carried out for diatoms, radiolarians, foraminifers, and calcareous nannofossils. Diatoms are present in limited core intervals and provide the primary basis for initial biostratigraphic age estimates. Three distinct diatom assemblages were noted of Quaternary, Pliocene, and late Eocene–earliest Oligocene age. Extant Quaternary diatoms are present at 2.12 mbsf and indicate an age of <0.66 Ma. This assemblage may extend down to a lithological contact at 2.92 mbsf. Two upper Pliocene horizons of diatomaceous clay are present from ~113.95 to ~114.10 mbsf and from ~114.50 to ~115.15 mbsf. Diatoms in these intervals belong to the *T. kolbei* (1.8–2.2 Ma) and *T. vulnifica* (Antarctic shelf) or *T. insigna–T. vulnifica* (Southern Ocean) Zones (2.2–3.2 Ma), respectively. In support of these assignments, preliminary radiolarian data constrain the age of the lower Pliocene bed to >2.4 Ma.

A distinct change in lithology occurs at ~135.65 mbsf, which most likely represents a major disconformity. Diatoms beneath this change, between 135.73 and 153.48 mbsf, are early Oligocene–late Eocene in age (~33 to ~37 Ma). No diatoms were recovered below 153.48 mbsf.

Planktonic foraminifers are common in two intervals in the upper ~90 m of Hole 1166A, and these assemblages are consistent with age interpretations derived from diatom and radiolarian biostratigraphy. Foraminiferal populations indicate that during intervals in the late Pliocene sea-ice concentrations were less than today. Diatoms suggest that marine conditions existed at Site 1166 during intervals in the earliest Oligocene to late Eocene; the dominance of planktonic diatoms in this interval also suggests that waters were >50 m deep at distal position relative to the ice margin (that is, if glaciers were present). Calcareous nannofossils were largely absent in Hole 1166A.

Initial postcruise analyses of palynofloras document well-preserved dinoflagellate and pollen assemblages in Units II–V. These results indicate a middle to late Eocene age for Units II and III and Late Cretaceous (Turonian-Santonian) age for Units IV and V.

Sedimentation Rates

Figure F20 is a plot of age vs. depth for Hole 1166A. Seven diatom and six radiolarian datums were used (Table T3), along with one paleomagnetic polarity tie, to construct this age model. Four intervals of Quaternary, late Pliocene, earliest Oligocene–late Eocene, and Turonian age are recognized. A linear sedimentation rate is not assumed between the well-constrained sections because unconformities may exist in these intervals.

F20. Age-depth plot for Hole 1166A, p. 67.

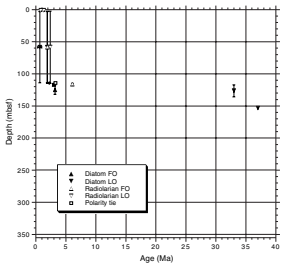

PALEOMAGNETISM

Methods

Analyses were conducted to provide an initial characterization of the paleomagnetic and mineral magnetic properties at Site 1166 and to develop a preliminary magnetic polarity zonation for the core. Forty-three RCB archive core halves from Hole 1166A were measured with the shipboard pass-through cryogenic magnetometer. Natural remanent magnetization and remanent magnetization after alternating field (AF) demagnetization were measured at 4-cm intervals. Three AF steps at 10, 20, and 30 mT were used for all core sections. A total of 111 oriented discrete samples (standard 8-cm^3 cubes) were collected from the working halves, from both coarse and fine lithologies. Sixty-three discrete samples were AF demagnetized at successive peak fields of 10, 20, 30, 40, 50, 60, 70, and 80 mT to verify the reliability of the whole-core measurements on the archive halves. Best-fit lines were calculated for the progressive demagnetization data and were evaluated by principal component analysis (PCA) (Kirschvink, 1980). The maximum angular deviation was calculated to provide an estimate of the precision for each best-fit line.

Mineral magnetic analyses were conducted on a set of representative discrete samples after they had been subjected to AF demagnetization (see "Paleomagnetism," p. 16, in the "Explanatory Notes" chapter). The low-field magnetic susceptibility (k) was routinely measured for 65 samples, and the data was compared with the whole-core susceptibility

log. For these samples, the frequency-dependent susceptibility, *fd*(%), was also evaluated. An anhysteretic remanent magnetization (ARM) was imparted on 63 samples using a 100-mT AF with a superimposed 0.05-mT bias field. Twenty-seven samples were subjected to isothermal remanent magnetization (IRM) imparted in a direct-current field of 1.3 T. IRM was then demagnetized by inverting the sample and applying a backfield of 300 mT to determine the S-ratio ($-IRM_{-0.3T}/IRM_{1T}$) (e.g., Verosub and Roberts, 1995). Moreover, on selected samples we investigated

1. The progressive acquisition of the IRM up to 1.3 T,
2. The coercivity of remanence (B_{cr}), and
3. Stepwise thermal demagnetization of a composite IRM (Lowrie, 1990). The low-field susceptibility (at low frequency) was monitored after each thermal step to detect any possible mineralogical changes.

Results

Rock Magnetism

Despite poor core recovery in Hole 1166A (18.6%), enough material was obtained to establish a rock magnetic stratigraphy for the sequence. Downhole variations of the concentration-dependent parameters, including k, ARM, and IRM intensities, reveal alternating intervals of high and low magnetic mineral concentration that mirror the main lithostratigraphic units (Fig. **F21**). In particular, intervals of increased magnetic mineral concentration are present within Subunit IB and the uppermost part of Unit II. Conversely, intervals of decreased ferrimagnetic concentration are found in lithostratigraphic Subunit IC, Units II (lower half), III, and IV (with the exception of an increase at ~285 mbsf in black clay).

Preliminary analyses of mineralogy–dependent parameters (e.g., S-ratio, B_{cr}, and thermal unblocking temperature) indicate that high-coercivity minerals (e.g., hematite or goethite) are not present in samples from much of the core. Plots of IRM acquisition have steep slopes at low magnetic induction, with saturation isothermal magnetization reached at fields of 0.2–0.3 T (Fig. **F22**). The thermal demagnetization of the three orthogonal IRMs confirms that most of the remanence is held by the soft coercive fraction. Above ~140 mbsf, the intensity decays in a quasi-linear fashion from room temperature to the Curie temperature of magnetite (580°C), with curve slope changes observed between 330° and 360°C (Fig. **F23**). During thermal treatment, the magnetic susceptibility progressively decreases from 20° to 700°C. Below ~140 mbsf, the contribution of the soft coercivity fraction is almost completely removed in the 330°–360°C range. A weak residual remanence that dissipates at 580°C was observed in Samples 188-1166A-17R-1, 127 cm, and 27R-1, 44 cm (152.67 and 248.04 mbsf, respectively) (Fig. **F23**). The bulk susceptibility of these samples begins to increase at 330°–360°C during thermal treatment, probably because of thermochemical alteration of clay minerals or sulfides. The presence of iron sulfides below ~140 mbsf is strongly supported by geochemical analyses that indicate a major drop in dissolved sulfate below ~150 mbsf (see **"Inorganic Geochemistry,"** p. 29). Additional evidence supporting the presence of iron sulfides comes from the magnetic behavior of the discrete samples during AF demagnetization. For some samples (~135–146

F21. Downhole variation of concentration-dependent parameters in Hole 1166A, p. 68.

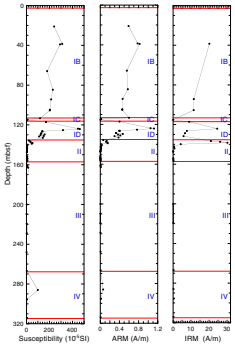

F22. IRM acquisition curves for four representative samples from Hole 1166A, p. 69.

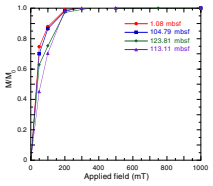

F23. Thermal demagnetization of a composite three-axis IRM for two representative samples, p. 70.

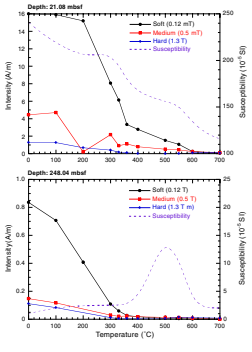

mbsf), the AF cleaning at steps >50 mT was obscured by the simultaneous acquisition of a gyromagnetic remanence (Fig. F24). This is probably due to the irreversible flip of the single-domain grain moments during AF demagnetization (Stephenson, 1980, 1981). These features, also observed during Leg 161 (Shipboard Scientific Party, 1996) and Leg 174A (Shipboard Scientific Party, 1998), have recently been theorized to provide proof of the presence of iron sulfides (e.g., Snowball, 1997; Hu et al., 1998; Sagnotti and Winkler, 1999).

Paleomagnetic Behavior and Magnetostratigraphy

Poor core recovery makes magnetic polarity interpretation difficult for Hole 1166A. For this reason, we will only describe the magnetic polarity stratigraphy deduced for the interval between 112 and 160 mbsf, where recovery is relatively high.

As at Site 1165, the lack of azimuthal orientation does not pose a problem for magnetostratigraphic studies because the field has a steep inclination (±78.4°) at the Site 1166 latitude (67.7°S). Consequently, the magnetic polarity zonation was determined from the paleomagnetic inclinations obtained after 30-mT AF steps, from long-core measurements, and from PCA of characteristic remanence components of discrete samples.

For 50% of the discrete samples, stable paleomagnetic behavior was evident in the vector component diagram, with characteristic direction of magnetization (ChRM) generally tending toward the origin and maximum angular deviation lower than 10°. These directions are in excellent agreement with the long-core measurements. For the remaining samples, demagnetization behavior is complex and reliable ChRMs are difficult or impossible to determine.

The inclination of ChRM from discrete samples and long-core measurements has a distinct bimodal distribution that demonstrates the dominance of the two stable polarity states (Fig. F25). As expected at this high-latitude site, steep-normal and steep-reverse inclinations are dominant. In conjunction with evidence from vector component diagrams (Fig. F24), this indicates that secondary magnetization components have been removed.

A good magnetostratigraphic signal is recorded in the sediments between 80 and 160 mbsf (Fig. F26). Unfortunately, it is difficult to correlate this record with the GPTS (Cande and Kent, 1992, 1995; Berggren et al., 1995) because of limited biostratigraphical datums (see "Biostratigraphy and Sedimentation Rates," p. 17). Upper Pliocene marine diatoms, including *T. kolbei* (LO = 1.8–1.9 Ma) and *T. vulnifica* (range 2.2/2.3 to 2.8/3.2 Ma), are found in two greenish gray silt beds in Core 188-1166A-13R. The presence of these taxa constrains the age of the reversed-normal-reversed polarity pattern that occurs between 113.40–117.10 mbsf to the C2r.1r (possibly C2r.2r), C2An.1n, and C2An.1r Subchrons. The correlation of the upper reversed magnetozone to Subchron C2r.1r implies that a disconformity exists at ~114.80 mbsf, indicating a significant interval of missing time (>0.441 Ma), including Subchrons C2r.1n and C2r.2r.

In the stratigraphic interval from seafloor to 113.40 mbsf, magnetostratigraphic interpretation is difficult. In addition to extremely poor recovery, microfossils (especially diatoms) are low in abundance at intermittent intervals and are not age diagnostic. The only interval characterized by an abundant and well-preserved diatom assemblage indicating a late Quaternary age (<2.22 mbsf) (see "Biostratigraphy

F24. Vector component diagrams of demagnetization behavior of four samples from Hole 1166A, p. 71.

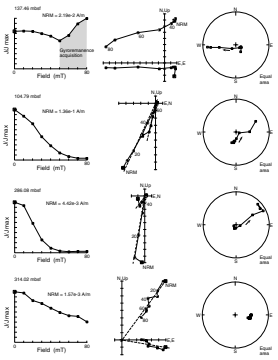

F25. Histogram of paleomagnetic inclinations from Hole 1166A, p. 73.

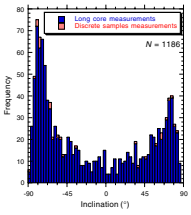

F26. Magnetostratigraphic record from Hole 1166A, p. 74.

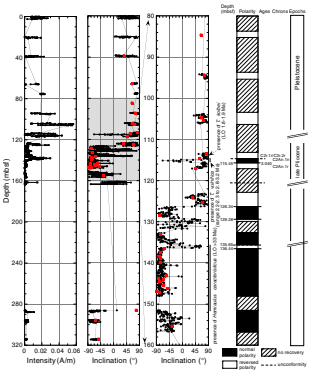

and Sedimentation Rates," p. 17) conflicts with the reversed-polarity magnetostratigraphic evidence, indicating an age older than 0.78 Ma. Upper sections of the core show "soupy" drilling disturbance (see "Lithostratigraphy," p. 9), suggesting that the observed remanence is drilling induced and does not represent the primary remanence. Furthermore, the paleontological samples were taken from a distinct in situ sponge spicule–rich bed and are unlikely to be contaminated.

The polarity record from 117.10 to 135.65 mbsf lacks biostratigraphic constraints, which makes the correlation with the GPTS difficult.

A major change in lithology occurs within Section 188-1166A-15R-2 (at 135.63 mbsf), from dark gray diamictons (Unit I) above to olive-gray diatom-bearing claystones (Unit II) below (see "Lithostratigraphy," p. 9). Below this boundary, a thin reversed-polarity interval is followed downcore by a thick interval of normal polarity (between 142.45 and 148.25 mbsf). The age of the interval between 142.45 and 148.26 mbsf is partially constrained by the presence of the diatom *H. caracteristicus,* which indicates an age older than ~33 Ma, based on its LO within Chron C13n in Hole 744B on the southern Kerguelen Plateau (see "Biostratigraphy and Sedimentation Rates," p. 17).

INORGANIC GEOCHEMISTRY

Sixteen interstitial water samples were collected from Hole 1166A and analyzed according to the procedures outlined in "Inorganic Geochemistry," p. 19, in the "Explanatory Notes" chapter (Table T4). The sampling protocol called for the gathering of one 10-cm-long whole-round interval from each core to total depth. The shallowest sample was taken from 1.45 mbsf and the deepest from 296.7 mbsf, ensuring coverage of diagenetic processes throughout the complete cored section.

T4. Interstitial water chemistry from shipboard measurements, p. 103.

Sulfate and Ammonium

Downcore profiles of sulfate and ammonium typically reflect the degradation of organic matter. Sulfate values decrease linearly (R^2 = 0.9939) downhole from an initial seafloor value of 28 to 8 mM at ~150 mbsf; however, sulfate values do not reach zero at this site (Fig. F27). Below 150 mbsf, sulfate values increase slightly to 14.2 mM at 287.4 mbsf and decrease again to 11.6 mM at 296.7 mbsf. Because sulfate does not become exhausted at this site and because there is no discernible methane in the sediment, we can conclude that coring did not penetrate the carbon dioxide (methanic) reduction zone (cf. Site 1165). Concomitant with decreasing sulfate, ammonium values increase from 117 µM near the seafloor to a maximum value of 1277 µM at 296.7 mbsf (Fig. F27). At both 75 and 150 mbsf, the downcore ammonium profile changes, possibly reflecting differing abundances of organic matter. Typically, alkalinity follows a trend similar to ammonium; however, at this site alkalinity appears to be more a function of mineral transformation than of sulfate reduction processes (see "Silica, Alkalinity, Potassium, and Phosphate," p. 30).

F27. Downcore profiles of sulfate and ammonium, p. 75.

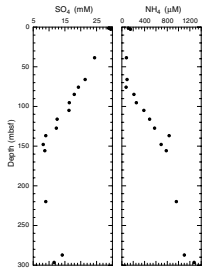

Calcium, Magnesium, Strontium, Lithium and Manganese

Concentration profiles of calcium, magnesium, and strontium (Fig. F28) typically reflect processes of carbonate dissolution and precipitation. Generally, in interstitial waters the magnesium concentration is inversely related to calcium concentration. This pattern is preserved above ~75 mbsf, as calcium increases from 12 mM near the seafloor to 21 mM at 75.9 mbsf and magnesium decreases from 51 to 33 mM over the same interval. Below ~75 mbsf, both calcium and magnesium concentrations decrease to their minimum values of ~22 and 15 mM, respectively, near the base of the hole. Strontium shows a near-linear increase from 94 µM immediately below the seafloor to 301 µM at 296.70 mbsf. Lithium shows clear highs of 26 and 68 µM at the sea floor and 287.40 mbsf, respectively, but is routinely <11 µM throughout the rest of the hole. Manganese reaches a high of 123.1 µM near the seafloor, then decreases to 15.4 µM at 38.64 mbsf before declining slowly to ~2 µM at 296.70 mbsf.

F28. Downcore profiles of calcium and magnesium, strontium, lithium, and manganese, p. 76.

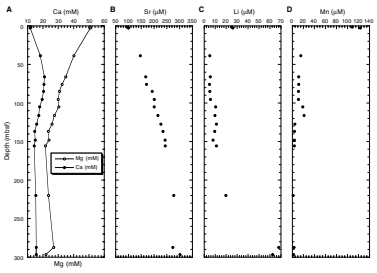

Silica, Alkalinity, Potassium, and Phosphate

Downhole profiles of silica, alkalinity, potassium, and phosphate at Site 1166 decrease rapidly from relatively high concentrations near the seafloor to minimum values between 50 and 100 mbsf (Fig. F29). Silica concentration in the interstitial waters just below the mudline is 750 µM, which corresponds directly to a silica-rich interval in the sediment (see **"Biostratigraphy and Sedimentation Rates,"** p. 17). Between the seafloor and 100 mbsf, silica values decrease to 170 µM. Between 100 and 150 mbsf, the silica concentration varies repeatedly from ~500 to 100 µM. From 150 to 300 mbsf, the silica concentration remains fairly constant (77–126 µM).

Similar trends were observed downcore for both alkalinity and potassium. Alkalinity values range between 3 and 4.5 mM near the seafloor and then decrease to 1.23 mM at 75 mbsf. Below 150 mbsf, alkalinity remains relatively constant (2.2–2.7 mM) to 300 mbsf. Similarly, the maximum concentration of potassium (12.72 mM) occurs near the seafloor (1.5 mbsf) and decreases to ~2 mM between 75 and 85 mbsf. Below 150 mbsf, the potassium concentration remains fairly constant at 5 mM. Phosphate concentrations peak at 17 µM near the seafloor. Below 40 mbsf, the phosphate concentration remains below detection limits, except for a single analysis at 116.2 mbsf that reaches 3 µM.

It is likely that clay mineral reactions are responsible for the downhole silica, potassium, alkalinity, and phosphate profiles.

F29. Downcore profiles of silica, alkalinity, potassium, and phosphate, p. 77.

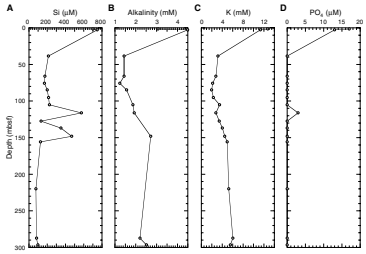

Sodium, Chloride, and Salinity

Concentrations of sodium and chloride (Fig. F30) approximate modern seawater values near the seafloor in Hole 1166A. By 2.74 mbsf, sodium and chloride values have risen sharply to 493 and 566 mM, respectively. Concentrations remain consistently high to ~75 mbsf. Between 95 and 137 mbsf, sodium increases slightly and chloride shows a small decrease in concentration. Salinity at Site 1166 steadily decreases from 35.5 to 32.5 at the base of the hole.

F30. Downcore profiles of sodium, chloride, and salinity, p. 78.

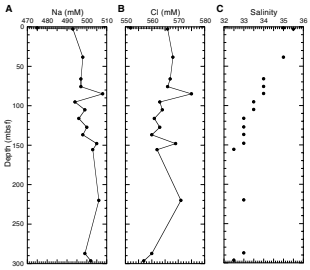

ORGANIC GEOCHEMISTRY

Shipboard organic geochemical studies of cores from Hole 1166A included monitoring of hydrocarbon gases, carbonate and organic carbon, total sulfur and total nitrogen content, and Rock-Eval pyrolysis characterization of organic matter. Procedures are summarized in "Organic Geochemistry," p. 20, in the "Explanatory Notes" chapter.

Hydrocarbon Gases

Cores recovered from Hole 1166A were monitored by the headspace method for hydrocarbon gases. All reliable analyses of cores were at background levels (4–10 parts per million by volume [ppmv]) for methane, and no other hydrocarbons were detected.

Carbon and Elemental Analyses

Thirty-seven sediment samples were analyzed for calcium carbonate (inorganic carbon; IC), and 14 selected (darker colored) samples from Hole 1166A were analyzed for total carbon, OC (by difference), total nitrogen (TN), and total sulfur (TS). The results are reported in Table T5. IC and OC contents are plotted against depth of burial in Figure F31. Carbonate content is generally low (0.01–0.15 wt% IC), with scattered beds having between 0.2 and 0.5 wt% IC and one sample with 1 wt% IC.

OC content varies according to lithostratigraphic unit sampled. The upper diamicton (Unit IB) contains 0.4–1.4 wt% OC. Samples from the massive sand (lithostratigraphic Unit III) contain 0.2–0.5 wt% OC, except for a carbonaceous bed near the base of Unit III, which has 9.2 wt% OC. The carbonaceous claystone (lithostratigraphic Unit IV), from 280 to 315 mbsf, contains 1.5–5.2 wt% OC.

TN content is generally between 0.01 and 0.27 wt%, and carbon/nitrogen (C/N) values range from 7 to 50, except for the sample with 9.2 wt% OC, which has a C/N ratio of 93. Most of the samples are enriched in carbon relative to nitrogen, which suggests input of terrestrial organic matter, especially for samples containing >1% OC.

TS content is similarly scattered, with many analyzed samples showing sulfur below detection limits. When TS is related to OC, most samples are sulfur deficient compared with average marine sediments. The one sample with more sulfur (5.9 wt%) than carbon (4.5 wt%) was from the core catcher, and contamination is suspected.

Organic Matter Characterization

Ten samples from Hole 1166A were characterized by Rock-Eval pyrolysis (Table T6). Samples with >0.5 wt% OC were selected for analysis. Pyrolyzable hydrocarbons (S_2 yields) range from 0.13 to 4.3 mg hydrocarbon/g of sediment. The pyrolyzable fraction of the OC is low (hydrogen index values ≤48 mg hydrocarbon/g of carbon), which is consistent with degraded plant material as a possible source of organic matter in the more carbonaceous (>2% OC) samples. The T_{max} values and the broad S_2 peak shapes in the pyrograms (not shown) indicate that some samples contain mixtures of small amounts of primary organic matter with variable amounts of possibly recycled and degraded thermally mature organic matter. The samples from lithostratigraphic Unit I at 75.4,

T5. Carbon, nitrogen, and sulfur analyses of sediments, p. 104.

F31. Weight percent of inorganic carbon and organic carbon in sediments, p. 79.

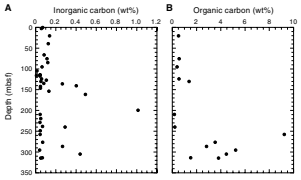

T6. Organic carbon and Rock-Eval pyrolysis on selected samples, p. 105.

124.2, and 130.2 mbsf have lower OC content (0.56–1.39 wt%) and higher T_{max} values (462°, 477°, and 438°C, respectively), indicating greater proportions of recycled organic matter. The samples from lithostratigraphic Unit IV and the base of Unit III, with OC contents of 2.8 to 9.2 wt%, have T_{max} values of 420°–425°C. These preglacial shelf sediments appear to contain mostly primary (first cycle) organic matter, whereas younger glacial tills (Unit I) contain ~0.5% recycled higher maturity organic matter, with lesser but variable amounts of primary organic matter. The presence of recycled organic material within Unit I is suggested by Rock-Eval T_{max} values that approach 480°C as organic carbon decreases toward 0.5 wt%.

PHYSICAL PROPERTIES

Multisensor Track

At Site 1166, natural gamma-ray (NGR) activity was measured at intervals of 12 cm. Magnetic susceptibility (MS) and gamma-ray attenuation (GRA) bulk density were measured at 4-cm intervals. All measurements were taken on whole-round samples (see **"Physical Properties,"** p. 21, in the "Explanatory Notes" chapter). No *P*-wave measurements were made on the cores because of the many air gaps in the whole-core sections.

Because of the low recovery, only a few cores were available for multisensor track (MST) measurement. For information on available raw data, see the **"Related Leg Data"** contents list. The quality of the MST measurements was degraded by incompletely filled core liners that were a result of the RCB drilling method, and direct interpretation of the raw GRA and MS data is not possible at this stage. General trends might be inferred from the NGR data. Extensive postcruise work is needed to carefully edit the data. For higher quality continuous physical properties data, refer to **"Downhole Measurements,"** p. 36.

The core recovery was such that an insufficient number of measurements were taken to allow reliable binned NGR spectra to be produced. The NGR data do, however, show a trend similar to the mineralogy values (Fig. **F32**). The number of NGR counts indicates the relative concentration of the total clay-mineral content plus the K-feldspars. Lithostratigraphic Subunits IC and ID and Unit II have a somewhat higher NGR activity than the diamicts of Subunits IA and IB and the sands in Unit III, which indicates that Subunits IC and ID probably have a higher total clay content plus K-feldspars than those units above and below. Unit IV has a high mica content (see **"Lithostratigraphy,"** p. 9), a mineral that contributes significantly to the potassium content (and therefore to the content of radioactive ^{40}K) in the sediments.

Moisture and Density Measurements

Gravimetric and volumetric determinations of moisture and density were made for 56 samples from Hole 1166A (Cores 188-1166A-1R through 40R). One sample was taken, where possible, from each section of each core. Wet mass, dry mass, and dry volume were measured; from these measurements, percentage water weight, porosity, dry density, bulk density, and grain density were calculated (see **"Physical Properties,"** p. 21, in the "Explanatory Notes" chapter; also see the **"Related Leg Data"** contents list for available raw data).

F32. Bulk mineralogy from XRD and NGR vs. depth, p. 80.

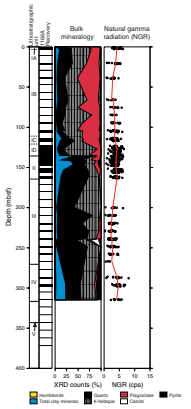

The grain densities measured at Site 1166 are shown in Figure F33. Twenty-one determinations of grain density were obtained from lithostratigraphic Unit I (0–135.41 mbsf), giving an average value of 2.70 g/cm³, with a range of 2.60–2.75 g/cm³. Within Unit I, the measured values show three decreasing-downward cycles: 0–66, 75–117, and 124–135 mbsf. The lowermost cycle (124–135 mbsf) corresponds to lithostratigraphic Subunit ID. One possible reason for the decreasing-downward trend in each cycle may be a decreasing clay/quartz ratio, although the NGR data (see "Multisensor Track," p. 32, and "Downhole Measurements," p. 36) do not show a corresponding variation. The cycles also suggest a cyclic depositional history and may represent three advances and retreats of the continental ice sheet. Further explanation of these cycles requires postcruise investigation.

Fourteen determinations of grain density were made in lithostratigraphic Unit II (135.63–156.62 mbsf). The mean value is 2.61 g/cm³, with a range of 2.48–2.73 g/cm³. Unit II has a relatively lower grain density than either the unit above or below, probably because of a higher content of diatomaceous material (see "Lithostratigraphy," p. 9). Siliceous tests of diatoms have a density of 2.0–2.25 g/cm³ (Klein and Hurlbut, 1977), and the addition of 10%–20% diatomaceous material to a predominantly clay material would explain the measured grain densities.

Within lithostratigraphic Unit III (156.62–267.17 mbsf), 14 determinations of grain density were made, giving an average value of 2.68 g/cm³, with a range of 2.65–2.74 g/cm³. The measured values are relatively uniform with depth, showing no particular trend.

Within lithostratigraphic Unit IV (156.62–267.17 mbsf), seven determinations of grain density were made, giving an average value of 2.72 g/cm³, with a range of 2.51–3.48 g/cm³. The measurement of 3.48 g/cm³ at 297.75 mbsf was made on a nodule of siderite (see "Lithostratigraphy," p. 9), which was present only sporadically in the section and was therefore not plotted on Figure F33. If that measurement is excluded, then the average grain density within Unit IV is 2.59 g/cm³. The measurements show a relatively broad scatter (2.51–2.67 g/cm³), within which there is no apparent trend. The generally lower values of grain density in Unit IV than in Unit III are likely traceable to the higher OC content in Unit IV (1.6%–9.3%) (see "Organic Geochemistry," p. 31) than in Unit III (<0.5%).

The porosities measured at Site 1166 are shown in Figure F33B. A total of 21 determinations of porosity were made in lithostratigraphic Unit I. The average porosity value is 30.6%, with a range of 22.8%–57.5%. The values show no trend with depth within the unit, except that lithostratigraphic Subunit ID contains a cluster of values with an average value of 23.8%, which ranges from 124.19 to 133.25 mbsf.

Fourteen determinations of porosity were made in lithostratigraphic Unit II. Within the unit, the average porosity value is 49.5%, with a range of 33.5%–57.9%. A possible explanation for the relatively higher porosity of Unit II compared to Units I and III is the higher biogenic silica content of the unit, which could inhibit compaction as described by Bryant and Rack (1990). Within lithostratigraphic Unit III, 14 determinations of porosity were calculated. Within the unit, the average value of porosity is 24.5%, with a range of 18.0%–31.6%. Neither Unit II nor Unit III displays any trend in porosity with depth.

Seven determinations of porosity were made in lithostratigraphic Unit IV. Within the unit, the average value of porosity is 31.6%, with a

F33. Grain density and porosity from discrete measurements, p. 81.

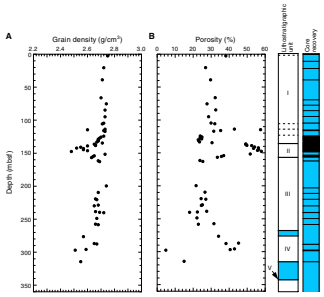

range of 4.8%–45.2%. The measurement of 4.8% was made on a nodule of siderite at 297.75 mbsf (see "Lithostratigraphy," p. 9). If that measurement is excluded, then the average porosity within Unit IV is 36.0%. The measurements appear to show a downward increase in the upper portion of Unit IV, but this may be simply an artifact of scatter in the few data points available for the unit. The porosity of Unit IV is higher than that of Unit III, which may be related to the higher OC content of Unit IV (1.6%–9.3%, as compared to <0.5% in Unit III) (see "Organic Geochemistry," p. 31).

No measurements of grain density were made in lithostratigraphic Unit V.

Other parameters that are derived from the measured data include bulk density, dry density, water content, and void ratio. Bulk-density and dry density values are presented in Figure F34. A total of 56 determinations of bulk and dry density were made on samples from Hole 1166A. Through lithostratigraphic Unit I, the average is 2.19 g/cm³. In Unit II, the value of bulk density drops abruptly to 1.83 g/cm³. The relatively low value of bulk density of Unit II is a function of the low grain density (2.5–2.6 g/cm³) and high porosity (50%–60%), both of which are attributed to the diatom-bearing claystones found in the unit (see "Lithostratigraphy," p. 9). The bulk density rises abruptly to 2.28 g/cm³ in Unit III. Excluding the measurement on the siderite nodule at 297.75 mbsf, the average value of bulk density in lithostratigraphic Unit IV is 2.0 g/cm³. In Unit IV, there is relatively more scatter in the measurements than in the other units, giving a range in Unit IV of 1.91–2.33 g/cm³.

Water content (as a percentage of dry mass corrected for salt content) and void ratio are presented in Figure F35. These plots show trends similar to those observed in the porosity data.

Velocimetry

At Site 1166, *P*-wave velocities on split cores were measured at a frequency of one measurement per recovered section. The velocity probes *P*-wave sensor (PWS1 and PWS2), which allow measurements in z- and y-directions in soft sediments, were used only on Core 188-1166A-1R. Below this core, the sediments became too stiff to insert the probes, and *P*-wave velocities were measured in the x-direction (through the core liner) using probe PWS3. In some intervals, the sediments were consolidated or lithified enough to cut out blocks and measure the *P*-wave velocity in x-, y-, and z-directions using PWS3. The laboratory velocity measurements presented here (Fig. F36) were not corrected to in situ temperature and pressure conditions. Velocity data are compiled in Table T7 (see the "Related Leg Data" contents list).

At Site 1166, a velocity of 1792 m/s (z-direction) was measured at 3 mbsf in lithostratigraphic Subunit IA (Fig. F36). From 20 to 123 mbsf (lithostratigraphic Unit I), velocities range from 2000 to 2150 m/s. Within this zone, an interval of greenish gray clayey silt at 113–114 mbsf (lithostratigraphic Subunit IC) is characterized by a much lower velocity of ~1640 m/s. At the base of Unit I (114–136 mbsf), velocities display a steep increase from 1980 to 2395 m/s. Velocities then decrease abruptly back to ~2000 m/s (x-direction) in lithostratigraphic Unit II (136–157 mbsf). Furthermore, the dark greenish gray claystone found in Unit II displays a velocity anisotropy with velocities in the x-direction ~5% higher than the corresponding velocities in the z-direction,

F34. Bulk density and dry density from discrete measurements, p. 82.

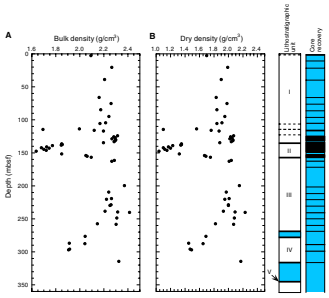

F35. Water content and void ratio from discrete measurements, p. 83.

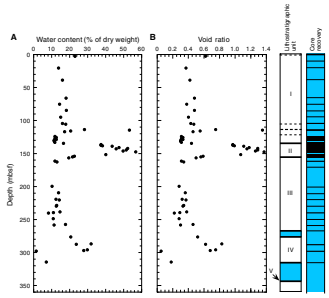

F36. Discrete velocity measurements obtained with the PWS, p. 84.

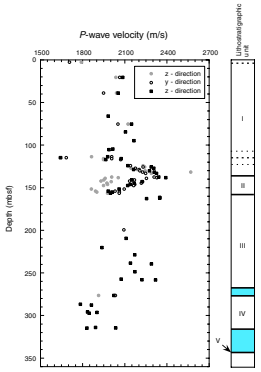

T7. Discrete *P*-wave measurements, p. 106.

which is most likely caused by the alignment of clay minerals parallel to the bedding plane. Because core recovery was poor, only a few velocity measurements cover lithostratigraphic Unit III (157–267 mbsf). The coarse sands in this unit have velocities ranging from 2100 to 2400 m/s with values increasing downhole. Below 267 mbsf, an abrupt decrease in velocity to values of ~1850 m/s is associated with a change in lithology from coarse sand to black claystone. Within lithostratigraphic Unit IV (276–315 mbsf), several highly lithified thin layers of siderite with velocities of up to 5740 m/s (not shown in Fig. F36) were found.

Undrained Shear Strength

The measured undrained shear strengths are tabulated in Table T8 and plotted in Figure F37. The shear strengths of the sediments show a firm upper part (Subunit IA) with a shear strength (C_u) of 53 kPa, underlain by a harder Subunit IB with shear strengths of at least 400 kPa (Fig. F37). Shear strengths through Subunit IB all have about the same value. The scatter in the measured values increases downcore into Subunit IC but indicates a trend of increasing shear strengths that continues down through the underlying units into the top of Unit II. In Unit II, the values exceed 900 kPa, the upper limit for the measurement tools on the ship.

The recorded depths of the cores (in mbsf) are 6.7 m too shallow, a result of missing the initial 6.7 m of the mudline sediments with the first RCB core (see "Operations," p. 7). Effective overburden stresses were computed to account for this missing portion of the sediment column. The shear strengths of normally consolidated clays normalized by the effective overburden pressure (p'_0) are expected to give C_u/p'_0 ratios of between 0.25 and 0.35 (Brooker and Ireland, 1965; Andresen et al., 1979). Figure F38 shows that for Site 1166, this value is exceeded for nearly all the measurements made. The uppermost sample, 2.63 mbsf, falls within the range expected for normally consolidated marine sediments. The upper few meters of marine sediments experiences a small degree of overconsolidation due to the same interparticle bonds that cause flocculation.

The C_u/p'_0 ratios (1.3–1.9) for the sample from 20.5 mbsf are the result of loading by an overburden greater than that of the present. Empirical relationships (Brooker and Ireland, 1965; Andresen et al., 1979) show that this previous load was 7–12 times the current overburden stress (295 kPa). Similarly, the values at 38.8 mbsf give a total previous overburden stress 3.5 times the present. The decreasing trend of C_u/p'_0 ratio with depth indicates that one previous load applied above 20 mbsf can account for the overconsolidation/compaction profile in Subunit IB. The normalized shear strengths (Fig. F38) exhibit another possible downhole increase into Subunit IC. This shows a possible second horizon at ~100 mbsf on which loading of ~3700 kPa, or three times the present overburden stress, has occurred and below which the sediments are further overcompacted.

The shear strengths in the upper 150 mbsf thus reveal a depositional history that includes at least one or two periods during which the sediments were compacted either by a thicker sediment column (removed by erosion), a glacier, or a combination of both. The loads needed are equivalent to ~2950 kPa at 20.5 mbsf (which corresponds to a sediment column 250 m thick or 330 m of nonbuoyant ice) and 3700 kPa at 100 mbsf (which corresponds to a sediment column 300 m thick or 420 m

T8. Measurements of undrained shear strength, p. 107.

F37. Measurements of undrained shear strength using the fall cone and pocket penetrometer, p. 85.

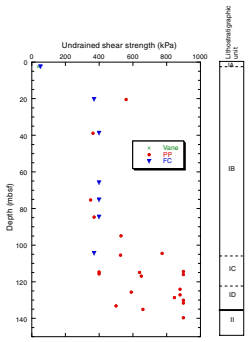

F38. Normalization of undrained shear strength with respect to effective overburden pressure, p. 86.

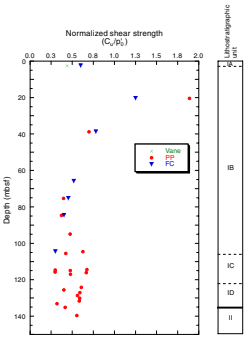

of nonbuoyant ice). It should also be noted that the stress history that can be deduced from sediment properties is limited to the maximum load that the sediment has experienced in the past. Therefore, the normalized shear strength profile (Fig. F38) does not exclude compaction episodes in the interval between 20 and 100 mbsf (e.g., at the breaks in the grain density vs. depth profile). It does, however, limit the past effective load to one less than or equal to that of the episode at 20 mbsf and thereby the corresponding thickness of eroded sediments or nonbuoyant ice.

Thermal Conductivity

Thermal conductivity was measured using both a full-space and a half-space needle probe, as appropriate to the strength of the core recovered. Measurements were made only on selected sections because of limited core recovery and core disturbance. It was frequently not possible to measure thermal conductivity because there were no pieces in the core long enough to use the half-space needle probe and the core was too strong to insert the full-space needle probe (see "Physical Properties," p. 21, in the "Explanatory Notes" chapter; also see the "Related Leg Data" contents list).

Table T9 presents the thermal conductivity measurements made at Site 1166, and Figure F39 shows the data plotted against depth. Eleven thermal conductivity measurements were made. The average thermal conductivity is 1.423 W/(m·°C), with a range of 0.938–2.159 W/(m·°C). There is no discernible difference in the thermal conductivities measured in lithostratigraphic Units I and II nor is there any trend with depth.

The measured values of thermal conductivity are in the range expected for soils (0.25–2.5 W/[m·°C]; Mitchell, 1993). Thermal conductivity in sediments is, as a first approximation, a linear combination of the conductivities of the grains and the interstitial water. It therefore depends upon porosity or bulk density and lithology. The thermal conductivity of water is ~0.6 W/(m·°C) and is much higher for most sediment-forming minerals. Thus, thermal conductivity should increase as dry density increases. The covariance of thermal conductivity and dry density is illustrated in Figure F39, where dry density is plotted with the measured thermal conductivities. The lower values of thermal conductivity measured at 115 and 146 mbsf are clearly reflected in the lower values of dry density measured at the same depths.

T9. Measurements of thermal conductivity, p. 108.

F39. Thermal conductivity measurements and dry densities, p. 87.

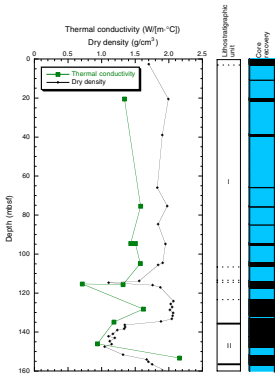

DOWNHOLE MEASUREMENTS

Operations

Wireline logging operations were conducted in Hole 1166A, and LWD/MWD was done in Hole 1166B (Fig. F40). For wireline logging, the drill string was placed at 41.2 mbsf to prevent borehole collapse and was raised to 32.0 mbsf as the tool string approached on its way up the hole. The depth to the seafloor for Hole 1166A was determined to be 480.0 mbrf, based on a drop in total gamma-ray emission to zero at that depth.

Three tool strings were run during wireline operations: the triple combo (resistivity, density, porosity, and natural gamma), the GHMT-Sonic combination (magnetic field, susceptibility, sonic wave velocities,

F40. Logging summary diagram showing log, pipe, and seafloor depths, p. 88.

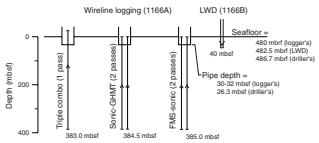

and natural gamma), and the FMS (resistivity images and natural gamma) (Table T10).

The combination of the dipole shear imager sonic (DSI) and GHMT into a single tool string is new and was run for the first time in Hole 1166A. Advantages of this combination over the usual arrangement, in which the FMS and Sonic tools are combined, are (1) the Sonic tool is able to record ~10 m lower in the hole because the GHMT is much shorter than the FMS tool; (2) both the DSI sonic tool and the FMS acquire data at high resolution, which limits the logging speed because there is a limit to the data transmission rate up the logging cable; and (3) the GHMT alone is relatively light, which makes it less likely to be able to pass through obstructions in the borehole.

Hole 1166B was logged using Anadrill LWD/MWD logging tools located a few meters above the drill bit. Only low weight on bit could be applied to drill the upper part of the hole because the hard sediments at shallow depth greatly increased the risk of snapping the LWD tools off the end of the heavier drill collars above. Consequently, drilling was slow and time constraints permitted only 40 m of LWD logs to be obtained.

The CDR LWD tool measured spectral gamma-ray and resistivity, which were recorded and stored within the tool's memory. The Power Pulse MWD tool measured weight on bit and downhole torque, and it transmitted these data, along with some of the CDR data, up to the ship in real time via pressure pulses in the borehole fluid (12 Hz; 3 bits/s).

T10. Logging operations summary, p. 109.

Data Quality

The caliper log on the triple combo shows that the borehole diameter varies from ~13 to >19 in. For the most part, the hole is smooth and <16 in wide, but there are two intervals where washouts (widenings) of the borehole are found: 163–193 and 103–142 mbsf (Fig. F41). In the wider washouts, the density and porosity tools loose contact with the borehole wall, causing poor data quality. The location of the washouts is typically controlled by the lithology. The MS and resistivity logs are relatively insensitive to borehole size.

The DSI sonic tool was run in *P* and *S* and dipole shear acquisition mode for the first pass and in the *P* and *S* mode (with more waveforms recorded) in the second pass. *P*-wave velocities were generally good for both passes, but both contain occasional erroneous spikes. The shear-wave velocity log from the dipole shear acquisition mode was good, but shear-wave velocities were not resolved from the *P* and *S* mode.

F41. Density, porosity, resistivity, and sonic velocity logs, with the logging units marked, p. 89.

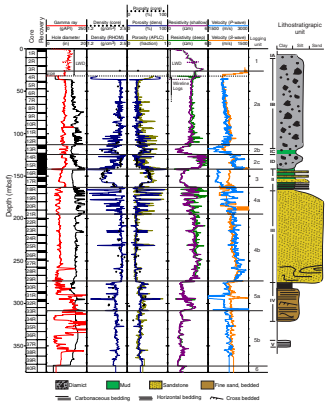

F42. Total gamma-ray, potassium, thorium, uranium, photoelectric effect, and magnetic susceptibility logs, p. 90.

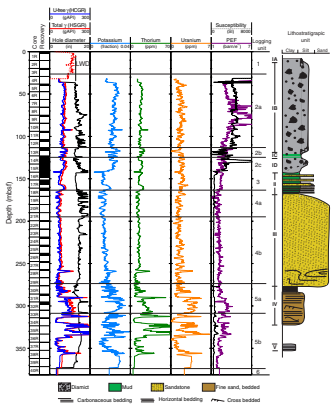

Logging Units

Although the logging units were chosen independent of lithology, they closely match the lithostratigraphic units (see "Lithostratigraphy," p. 9; Figs. F41, F42).

Unit 1 (0–25 mbsf)

Unit 1 covers most of the LWD section and is characterized by a steady increase in resistivity from near zero at the surface to 5 Ωm in the lowermost 3 m of the unit. High resistivities, such as 5 Ωm, close to the surface are typical of diamict. Apart from low gamma-ray values in the uppermost 2 m, the natural gamma log is fairly steady at ~130 gAPI.

The base of the unit is defined by a sharp decrease in natural gamma and resistivity.

Unit 2 (25–141 mbsf)

Logging Unit 2 corresponds to lithostratigraphic Unit I. Overall, Unit 2 is characterized by high bulk-density, low neutron porosity, and high gamma-ray values. Unit 2 has higher potassium values than the underlying Units 3 and 4, whereas the thorium values are only slightly higher than in the underlying two units. This likely reflects the relative abundance of potassium-rich K-feldspars and micas throughout this unit, as noted by XRD analysis (see "Lithostratigraphy," p. 9). If the drop in potassium values was caused by lower clay content, there would be a corresponding drop in the thorium log. Unit 2 is also characterized by high magnetic susceptibility, reflecting the presence of metamorphic and igneous clasts in the diamict.

Subunit 2a (25–112 mbsf)

This Subunit is marked by a relatively constant resistivity of ~4 Ωm and total gamma-ray values of ~125 gAPI. The low porosity of this subunit (~25%) results in high bulk-density, resistivity, and sonic velocity values. An increase in photoelectric effect (PEF) from 55 to 90 mbsf possibly reflects an increase in heavy mineral concentration, although this interpretation is not supported by the natural gamma logs. The increase could possibly reflect an increase in carbonate clasts, although the PEF rises higher than the carbonate value of 5 barn/e^-. XRD analysis from Core 188-1166A-9R (76 mbsf) suggests the presence of heavy minerals at concentrations of 1%–5%. The FMS image of this subunit shows the presence of numerous relatively small resistive clasts supported by a mixed sand/clay matrix, again in agreement with the observation of diamict in the cores (Fig. F43).

Subunit 2b (112–125 mbsf)

The prominent features of Subunit 2b are a lowering of resistivity to ~2 Ωm, a sharp decrease in magnetic susceptibility, and a decrease in *P*-wave velocity. A slight decrease in bulk density and a minor increase in total gamma-ray counts occur at the same time. These changes point to a clay-rich interval, as observed in the cores. Clays are generally of higher porosity than coarser grained lithologies, with clay beds supported by a "cardhouse" alignment of platy grains, whereas coarser grains are more densely packed. In addition, a sediment consisting of similar-sized grains has a higher porosity than a poorly sorted sediment (e.g., diamict), whose smaller grains fill the spaces left between the larger grains. The increase in gamma-ray values suggests that the lithology is clay rather than sand (in the absence of biogenic dilution). The sharp decrease in magnetic susceptibility relative to the subunits above and below indicates the lack of the reworked clasts bearing magnetic minerals in this subunit. The FMS image of Subunit 2b reveals a layered lithology with relatively low resistivity.

Subunit 2c (125–142 mbsf)

The resistivity values in Subunit 2c are the highest of the entire log; porosity and bulk-density values exceed those of Subunit 2a. The FMS image clearly shows the presence of larger and more frequent clasts than in the diamict of Subunit 2A (Figure F43). The high resistivity values probably reflect the larger and more frequent clasts.

F43. Representative examples of FMS images from Hole 1166A, p. 91.

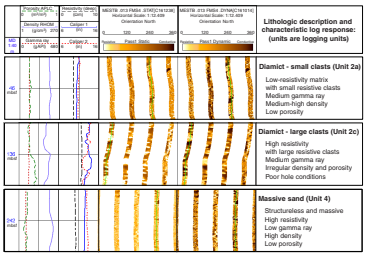

Unit 3 (142–163 mbsf)

The upper part of Unit 3 has low resistivity, density, and *P*-wave velocity values. However, the *S*-wave velocity remains quite high and the caliper log indicates a smooth borehole wall, which is not usually associated with high porosities. Thus, it appears that the sediments are highly cemented yet retain a high porosity. The core recovered from this unit (lithostratigraphic Unit II) is a hard claystone. The FMS images reveal a layered unit, lacking clasts.

There is a step increase in the gamma-ray values in the lower third of the unit. This step in gamma-ray counts corresponds to a similar increase in density, resistivity, and *P*-wave velocity, a decrease in neutron porosity, and a slight increase in susceptibility. Diatoms, radiolarians, and sponge spicules are present only in the upper half of Hole 1166A from 0 to 151.6 mbsf. The increase in bulk density and velocity with a corresponding increase in gamma-ray counts and magnetic susceptibility in the lower part of Unit 3 is likely related to a significant reduction in the amount of siliceous microfossils relative to the upper part.

Unit 4 (163–273 mbsf)

This unit is divided into two distinct subunits, the upper subunit showing alternations between high and low density and porosity and the lower subunit showing much less variation. The lower subunit corresponds to the massive sandstone of lithostratigraphic Unit III. The sandy texture of this subunit is apparent in the FMS images (Fig. **F43**). From the logs, we infer interbedded sandstone and claystones for the upper subunit; the negligible core recovery in this interval means the lithologies cannot be determined directly from core.

Subunit 4a (163–194 mbsf)

Subunit 4a contains a number of alternations between high and low density, porosity, resistivity, and velocity, in contrast to the uniform Subunit 4b. The low density and high porosity values are partly the result of bad contact because of borehole washouts, which may themselves be partly lithologically controlled. The alternating log character is consistent with an interbedded sand/clay lithology. In the velocity log, fluctuations appear to vary between a clay "baseline" velocity of Unit 3 and a sand "baseline" value for Subunit 4b, further suggesting interbedding of the sands and clays (Fig. **F44**). Poor core recovery in this part of the section prevented direct observation, however. The FMS image for Subunit 4a is also affected by washouts but indicates a generally sandier lithology than the base of Unit 3.

F44. Detail of the *P*-wave velocity log in logging Units 3 and 4, p. 93.

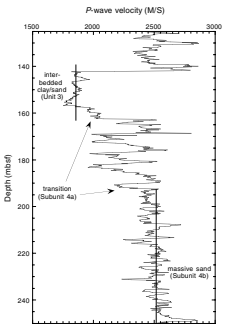

Subunit 4b (194–273 mbsf)

The logs of Subunit 4b show little variation, very low porosities (~20%), and a slight compaction trend with depth. Only three thin intervals with higher porosities and lower density and resistivity are displayed. The FMS images have a gritty texture and are interpreted as massive sands with occasional large clasts (Fig. **F43**). Toward the bottom of the unit, the images contain variably inclined bedding (Fig. **F43**), which confirms a similar observation of deformed beds in the core.

Unit 5 (273–373 mbsf)

Unit 5 shows a baseline shift to higher porosity and lower density, resistivity, and velocity values. Gamma-ray values start to increase rap-

idly, exceeding 300 gAPI in parts of the unit. Analysis of the gamma-ray log shows increases in all three components, particularly in thorium and uranium; the increase in potassium is proportionately less. Thorium is as high as 70 ppm in places, uranium peaks at around 7 ppm, and potassium peaks at 4%. Potassium values of Unit 5 are only slightly higher than those observed in the diamictites of Unit 2, which were K-feldspar rich.

The only possible sources of such large thorium and uranium values are heavy minerals such as zircon or monazite, derived from erosion of a continental igneous or metamorphic body and concentrated by sedimentary processes. Zircon was observed in low concentrations in the cores (see "Lithostratigraphy," p. 9). The thorium content of zircon ranges from 100 to 2500 ppm, and its uranium content ranges from 300 to 3000 ppm; the thorium content of monazite ranges from 4% to 12% (Rider, 1996). Taking the midpoints of these ranges, it would require ~0.2% zircon and ~0.03% monazite to generate the observed uranium and thorium increases above the background values (3 and 30 ppm, respectively).

The magnetic susceptibility mimics the gamma-ray log through this unit, suggesting that the concentration of magnetic minerals (likely to be magnetite) covaries with the concentration of heavy minerals.

Unit 5 corresponds to lithostratigraphic Unit IV, which is identified as sandy silts and organic-rich, laminated dark silty sands. The FMS shows the distinction between the two lithologies (Figs. F43). The porosity in this unit is low, which is consistent with a mudstone and suggests that the lithology remains the same to the bottom of the unit.

Subunit 5a (273–308 mbsf) differs from Subunit 5b (308–373 mbsf) primarily in the resistivity signal. Subunit 5a shows a gradual increase of resistivity followed by a rapid return to lower values at the top of Subunit 5b. Throughout Subunit 5b, the resistivity stays fairly constant but with an occasional spike.

Unit 6 (373–total depth)

This short interval was only reached by the GHMT, resistivity, and FMS tool strings. It is defined based on the resistivity and FMS values. The resistivity log shows a baseline increase, and the FMS log shows indications of a layered claystone with more clasts than the overlying unit. Without more data it is difficult to say whether this interval is distinct from Unit 5 or represents just a brief change.

Synthetic Seismogram

A synthetic seismogram was created using the IESX seismic software, part of Schlumberger Geoquest's Geoframe package. The *P*-wave slowness log from the second pass of the Sonic-GHMT tool string was converted to a velocity log. Bulk density was not used with the velocity to calculate an impedance log because the density log contained spikes caused by hole washouts. A subjective correction of these spikes could have led to more artifacts in the synthetic than would be generated by just using the velocity log alone. Thus, a reflection coefficient series was created from the velocity log (Fig. F45) and converted to two-way traveltime using a depth–two-way traveltime relation also derived from the velocity log.

A minimum phase source wavelet was extracted from the 20 traces centered on the projection of the site location on the seismic line BMR-

F45. *P*-wave slowness log, source wavelet, and synthetic seismogram for Hole 1166A, p. 94.

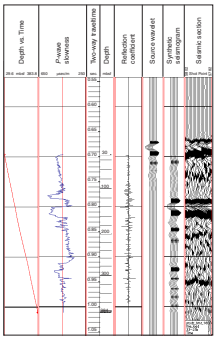

33-23B. This wavelet was convolved with the reflection coefficient series to produce the synthetic seismogram displayed in Figures F45 and F46.

Site 1166 lies ~1 km southeast of the seismic line 33-23B. Thus, the match between synthetic seismogram and seismic survey data was unlikely to be exact; however, the overlay (Fig. F46) gives an indication of what is causing the reflection pattern in the seismic.

The first large positive reflection at 0.785 s two-way traveltime is caused by the increase in velocity from logging Unit 2b to 2c (clays to clast-rich diamict). The reflection at 0.855 s is probably caused by the contact between logging Units 4a and 4b, although the offset between borehole and seismic line make this correlation tentative. The reflection at 0.95 s appears to be a negative polarity reflection, which might correlate with the drop in sonic velocity between logging Units 4 and 5 (although the synthetic seismogram would locate this reflection 0.03 s shallower in the section).

An interesting detail in the synthetic seismogram is that the unconformity reflection in the section (0.855 s) seems to be caused by the contrast between Units 4a and 4b, rather than the contrast between Units 3 and 4 (lithostratigraphic Units II and III). The unconformity would then separate what appears to be a proglacial outwash sand (below) from a lowstand and transgressive unit (above), speculatively indicating melting and recession of the initial glacial advance to the Prydz Bay margin and concomitant sea level rise.

F46. The synthetic seismogram and *P*-wave slowness log overlaid on seismic line BMR33-23B, p. 95.

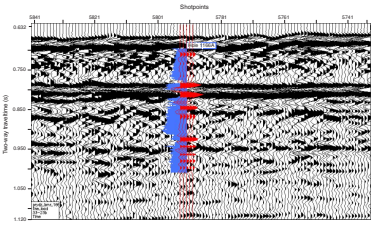

Correlation with Site 742

There is a close similarity in the resistivity and sonic logs for Sites 742 and 1166, which are separated by ~40 km (Fig. F47). Both the shape and the amplitude of the logs are very similar in logging Unit 2, indicating that the upper diamict (logging Subunit 2a), the clay-rich interval (logging Subunit 2b), and the lower diamict (Subunit 2c) are continuous across a wide area of Prydz Bay. Subunit 2a is about the same thickness at both sites, whereas Subunits 2b and 2c are about twice as thick at Site 742. The unconformity between Units 2 and 3 is well represented at both sites by an abrupt change in the resistivity log values; below this, the log-based correlation between the two sites becomes speculative.

F47. Correlation of resistivity and sonic velocity logs between Sites 1166 and 742, p. 96.

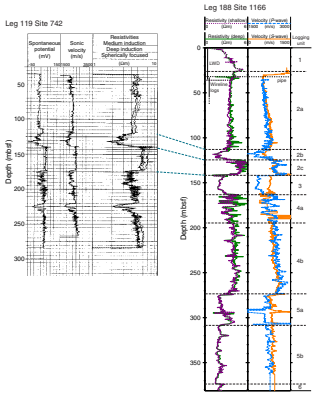

Magnetic Logs

Total magnetic field and magnetic susceptibility logs were recorded by the GHMT tool string. Under favorable conditions, a magnetic polarity stratigraphy can be derived from such logs. A correlation analysis of the logs (see "GHMT Tool String," p. 30, in "Downhole Measurements" in the "Explanatory Notes" chapter) was performed postcruise by the ODP wireline logging services GHMT processing center and interpreted by the logging staff scientist (Fig. F48).

The remanent component of the total field log was determined by removing the background field at the site (~53,380 nT), the field caused by the pipe, and the field caused by the induced magnetization of the sediment (calculated from the susceptibility) from the total field log. The correlation analysis of the remanent and induced components appears to have been successful in determining the polarity stratigraphy at the site. The GHMT polarity is consistent with the available core polarity (Fig. F48).

F48. Processed GHMT logs, p. 97.

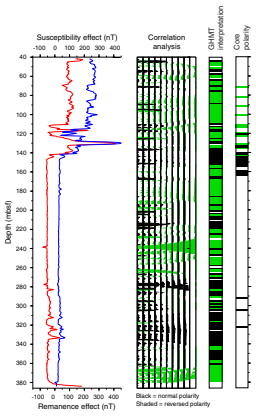

Dating based on the GHMT polarity stratigraphy is made difficult by the discontinuous sedimentation at the site and by the inherent uncertainties in the GHMT polarity determination (which should be used with caution). However, the lowermost part of the log (below 361 mbsf) seems to be clearly reversed polarity, and hence, not within the long Cretaceous normal superchron (83–118 Ma) (Cande and Kent, 1995).

Temperature Log

The Lamont-Doherty Earth Observatory temperature-acceleration-pressure tool recorded the temperature of the fluid in Hole 1066A as part of the triple combo tool string (Fig. F49). These measurements underestimate the formation temperature, as the fluid temperature does not have time to equilibrate to the formation temperature. A temperature of 6°C was recorded at the bottom of the hole (383 mbsf). The downgoing and upgoing curves have an offset of ~1°C, owing to the continuing borehole reequilibration during acquisition.

F49. Temperature of the borehole fluid vs. depth, p. 99.

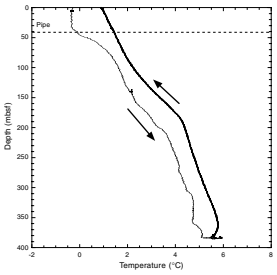

Summary and Conclusions

An excellent correlation exists between the downhole logs and the lithostratigraphy at Site 1166. The logs fill the gaps in the section where core recovery was poor. Most of the logs displayed high amplitude changes coincident with changes in lithology. For example, diamicts and sands have lower porosity and higher density, resistivity, and velocity than the clay-rich lithologies. The FMS was able to image individual clasts in the diamict and massive sands, clay layering, sand beds, and lithologic boundaries throughout the drilled section. The susceptibility drops by an order of magnitude as the lithology changes from diamict to clays and sands. Potassium values are high in the diamictite where K-feldspars and micas are abundant, but they drop in the clays and sands with the decrease in potassium-bearing minerals. Thorium and uranium values increase to very high values in the lower mudstone unit, indicating the presence of heavy minerals such as zircon and monazite.

REFERENCES

Abbott, W.H., 1974. Temporal and spatial distribution of Pleistocene diatoms from the southeast Indian Ocean. *Nova Hedwigia Beih.,* 25:291–346.

Abreu, V.S., and Anderson, J.B., 1998. Glacial eustasy during the Cenozoic: sequence stratigraphic implications. *AAPG Bull.,* 82:1385–1400.

Akiba, F., 1982. Late Quaternary diatom biostratigraphy of the Bellingshausen Sea, Antarctic Ocean. *Rep. Tech. Res. Cen. J.N.O.C.,* 16:31–74.

Andresen, A., Berre, T., Kleven, A., and Lunne, T., 1979. Procedures used to obtain soil parameters for foundation engineering in the North Sea. *Norw. Geotech. Inst. Publ.,* 129:1–18.

Baldauf, J.G., and Barron, J.A., 1991. Diatom biostratigraphy: Kerguelen Plateau and Prydz Bay regions of the Southern Ocean. *In* Barron, J., Larsen, B., et al., *Proc. ODP, Sci. Results,* 119: College Station, TX (Ocean Drilling Program), 547–598.

Barron, J., Larsen, B., et al., 1989. *Proc. ODP, Init. Repts.,* 119: College Station, TX (Ocean Drilling Program).

Barron, J.A., Baldauf, J.G., Barrera, E., Caulet, J.-P., Huber, B.T., Keating, B.H., Lazarus, D., Sakai, H., Thierstein, H.R., and Wei, W., 1991. Biochronologic and magnetochronologic synthesis of Leg 119 sediments from the Kerguelen Plateau and Prydz Bay, Antarctica. *In* Barron, J., Larsen, B., et al., *Proc. ODP, Sci. Results,* 119: College Station, TX (Ocean Drilling Program), 813–847.

Barron, J.A., and Mahood, A.D., 1993. Exceptionally well-preserved early Oligocene diatoms from glacial sediments of Prydz Bay, East Antarctica. *Micropaleontology,* 39:29–45.

Berggren, W.A., Kent, D.V., Swisher, C.C., III, and Aubry, M.-P., 1995. A revised Cenozoic geochronology and chronostratigraphy. *In* Berggren, W.A., Kent, D.V., Aubry, M.-P., and Hardenbol, J. (Eds.), *Geochronology, Time Scales and Global Stratigraphic Correlation*. Spec. Publ.—Soc. Econ. Paleontol. Mineral. (Soc. Sediment. Geol.), 54:129–212.

Bohaty, S.M., Scherer, R.P., and Harwood, D.M., 1998. Quaternary diatom biostratigraphy and palaeoenvironments of the CRP-1 drillcore, Ross Sea, Antarctica. *Terra Antart.,* 5:431–453.

Brooker, E.W., and Ireland, H.O., 1965. Earth pressures at rest related to stress history. *Can. Geotech. J.,* 2:1–15.

Bryant, W.R., and Rack, F.R., 1990. Consolidation characteristics of Weddell Sea sediments: results of ODP Leg 113. *In* Barker, P.F., Kennett, J.P., et al., *Proc. ODP, Sci. Results,* 113: College Station, TX (Ocean Drilling Program), 211–223.

Cande, S.C., and Kent, D.V., 1992. A new geomagnetic polarity time scale for the Late Cretaceous and Cenozoic. *J. Geophys. Res.,* 97:13917–13951.

————, 1995. Revised calibration of the geomagnetic polarity timescale for the Late Cretaceous and Cenozoic. *J. Geophys. Res.,* 100:6093–6095.

Cooper, A., Stagg, H., and Geist, E., 1991. Seismic stratigraphy and structure of Prydz Bay, Antarctica: implications from Leg 119 drilling. *In* Barron, J., Larsen, B., et al., *Proc. ODP, Sci. Results,* 119: College Station, TX (Ocean Drilling Program), 5–26.

Domack, E., O'Brien, P.E., Harris, P.T., Taylor, F., Quilty, P.G., DeSantis, L., and Raker, B., 1998. Late Quaternary sedimentary facies in Prydz Bay, East Antarctica and their relationship to glacial advance onto the continental shelf. *Antarct. Sci.,*10:227–235.

Eyles, N., and Eyles, C.H., 1992. Glacial depositional systems. *In* Walker, R.G., and James, N.P. (Eds.), *Facies Models: Response to Sea-level Change*. Geol. Assoc. Can., 73–100.

Forsberg, C.F., Solheim, A., Elverhøi, A., Jansen, E., Channell, J.E.T., and Andersen, E.S., 1999. The depositional environment of the western Svalbard margin during the late Pliocene and the Pleistocene: sedimentary facies changes at Site 986. *In*

Raymo, M.E., Jansen, E., Blum, P., and Herbert, T.D. (Eds.), *Proc. ODP, Sci. Results,* 162: College Station, TX (Ocean Drilling Program), 233–246.

Fryxell, G.A., 1991. Comparison of winter and summer growth stages of the diatom *Eucampia antarctica* from the Kerguelen Plateau and south of the Antarctica convergence zone. *In* Barron, J., Larsen, B., et al., *Proc. ODP, Sci. Results,* 119: College Station, TX (Ocean Drilling Program), 675–686.

Gombos, A.M., Jr., 1983. Middle Eocene diatoms from the South Atlantic. *In* Ludwig, W.J., Krasheninnikov, V.A., et al., *Init. Repts. DSDP,* 71 (Pt. 1): Washington (U.S. Govt. Printing Office), 565–582.

Harris, P.T., Taylor, F., Domack, E., DeSantis, L., Goodwin, I., Quilty, P.G., and O'Brien, P.E., 1997. Glaciomarine siliciclastic muds from Vincennes Bay, East Antarctica: preliminary results of an exploratory cruise in 1997. *Terra Antart.,* 4:11–20.

Harwood, D.M., 1989. Siliceous microfossils. *In* Barrett, P.J. (Ed.), *Antarctic Cenozoic History from the CIROS-1 Drillhole, McMurdo Sound*. DSIR Bull. N.Z., 245:67–97.

Harwood, D.M., and Maruyama, T., 1992. Middle Eocene to Pleistocene diatom biostratigraphy of Southern Ocean sediments from the Kerguelen Plateau, Leg 120. *In* Wise, S.W., Jr., Schlich, R., et al., *Proc. ODP, Sci. Results,* 120: College Station, TX (Ocean Drilling Program), 683–733.

Hu, S., Appel, E., Hoffmann, V., Schmahl, W.W., and Wang, S., 1998. Gyromagnetic remanence acquired by greigite (Fe_3S_4) during static three-axis alternating field demagnetization. *Geophys. J. Int.,* 134:831–842.

Huybrechts, P., 1993. Glaciological modelling of the Late Cenozoic East Antarctic ice sheet: stability or dynamism. *Geograf. Ann.,* 75A:221–238.

Kaczmarska, I., Barbrick, N.E., Ehrman, J.M., and Cant, G.P., 1993. Eucampia index as an indicator of the Late Pleistocene oscillations of the winter sea-ice extent at the Leg 119 Site 745B at the Kerguelen Plateau. *Hydrobiologia,* 269/270:103–112.

Kennett, J.P., and Srinivasan, M.S., 1983. *Neogene Planktonic Foraminifera: A Phylogenetic Atlas:* Stroudsburg, PA (Hutchinson Ross).

Kirschvink, J.L., 1980. The least-squares line and plane and the analysis of palaeomagnetic data. *Geophys. J. R. Astron. Soc.,* 62:699–718.

Klein, C., and Hurlbut, C.S., Jr., 1977. *Manual of Mineralogy, after James D. Dana:* New York (John Wiley & Sons).

Lazarus, D., 1990. Middle Miocene to Recent radiolarians from the Weddell Sea, Antarctica, ODP Leg 113. *In* Barker, P.F., Kennett, J.P., et al., *Proc. ODP, Sci. Results,* 113: College Station, TX (Ocean Drilling Program), 709–727.

————, 1992. Antarctic Neogene radiolarians from the Kerguelen Plateau, Legs 119 and 120. *In* Wise, S.W., Jr., Schlich, R., et al., *Proc. ODP, Sci. Results,* 120: College Station, TX (Ocean Drilling Program), 785–809.

Lowrie, W., 1990. Identification of ferromagnetic minerals in a rock by coercivity and unblocking temperature properties. *Geophys. Res. Lett.,* 17:159–162.

Mahood, A.D., and Barron, J.A., 1996. Late Pliocene diatoms in a diatomite from Prydz Bay, East Antarctica. *Micropaleontology,* 42:285–302.

Mahood, A.D., Barron, J.A., and Sims, P.A., 1993. A study of some unusual, well-preserved Oligocene diatoms from Antarctica. *Nova Hedwigia Beih.,* 106:243–267.

Milam, R.W., and Anderson, J.B., 1981. Distribution and ecology of Recent benthic Foraminifera of the Adelie-George V continental shelf and slope, Antarctica. *Mar. Micropaleontol.,* 6:297–325.

Mitchell, J.K., 1993. *Fundamentals of Soil Behavior* (2nd ed.): New York (John Wiley & Sons).

O'Brien, P.E., and Leitchenkov, G., 1997. Deglaciation of Prydz Bay, East Antarctica, based on echo sounder and topographic features. *In* Barker, P.F., and Cooper, A.K. (Eds.), *Geology and Seismic Stratigraphy of the Antarctic Margin* (Pt. 2). Am. Geophys. Union, Antarct. Res. Ser., 71:109–125.

O'Brien, P.E., Cooper, A.K., Richter, C., Macphail, M., Truswell, E.M., and Leg 188 Shipboard Scientific Party, in press. Results from ODP Leg 188—glacial onset and late Neogene fluctuations. *AGU 2000 Fall Meeting Abstract.*

Pichon, J.J., 1985. Les diatomees traceurs de le'evolution climatique et hydrologique de l'Ocean Austral cours du dernier cycle climatique [Ph.D. dissert.]. Univ. of Bordeax.

Quilty, P.G., 1985. Distribution of foraminiferids in sediments of Prydz Bay, Antarctica. *Spec. Publ. S. Aust. Dep. Mines Energy,* 5:329–340.

Rider, M., 1996. *The Geological Interpretation of Well Logs* (2nd ed.): Caithness (Whittles Publishing).

Robert, C., and Maillot, H., 1990. Paleoenvironments in the Weddell Sea area and Antarctic climates, as deduced from clay mineral associations and geochemical data, ODP Leg 113. *In* Barker, P.F., Kennett, J.P., et al., *Proc. ODP, Sci. Results,* 113: College Station, TX (Ocean Drilling Program), 51–70.

Sagnotti, L., and Winkler, A., 1999. Rock magnetism and palaeomagnetism of greigite-bearing mudstones in the Italian peninsula. *Earth Planet. Sci. Lett.,* 165:67–80.

Scherer, R.P., Bohaty, S.M., and Harwood, D.M., in press. Oligocene and lower Miocene siliceous microfossil biostratigraphy of Cape Roberts Project core CRP-2/2A, Victoria Land Basin, Antarctica. *Terra Antart.*

Shipboard Scientific Party, 1989a. Explanatory notes. *In* Barron, J., Larsen, B., et al., *Proc. ODP, Init. Repts.,* 119: College Station, TX (Ocean Drilling Program), 15–44.

————, 1989b. Site 741. *In* Barron, J., Larsen, B., et al., *Proc. ODP, Init. Repts.,* 119: College Station, TX (Ocean Drilling Program), 377–395.

————, 1989c. Site 742. *In* Barron, J., Larsen, B., et al., *Proc. ODP, Init. Repts.,* 119: College Station, TX (Ocean Drilling Program), 397–458.

————, 1996. Site 979. *In* Comas, M.C., Zahn, R., Klaus, A., et al., *Proc. ODP, Init. Repts.,* 161: College Station, TX (Ocean Drilling Program), 389–426.

————, 1998. Site 1071. *In* Austin, J.A., Jr., Christie-Blick, N., Malone, M.J., et al., *Proc. ODP, Init. Repts.,* 174A: College Station, TX (Ocean Drilling Program), 37–97.

Snowball, I.F., 1997. Gyroremanent magnetization and the magnetic properties of greigite-bearing clays in southern Sweden. *Geophys. J. Int.,* 129:624–636.

Stephenson, A., 1980. Gyromagnetism and the remanence acquired by a rotating rock in an alternating field. *Nature,* 284:48–49.

————, 1981. Gyroremanent magnetization in a weakly anisotropic rock sample. *Phys. Earth Plant. Inter.,* 25:163–166.

Stockwell, D.A., Kang, S.-H., and Fryxell, G.A., 1991. Comparisons of diatom biocoenoses with Holocene sediment assemblages in Prydz Bay, Antarctica. *In* Barron, J., Larsen, B., et al., *Proc. ODP, Sci. Results,* 119: College Station, TX (Ocean Drilling Program), 667–674.

Taylor, F., McMinn, A., and Franklin, D., 1997. Distribution of diatoms in surface sediments of Prydz Bay, Antarctica. *Mar. Micropaleontol.,* 32:209–229.

Verosub, K.L., and Roberts, A.P., 1995. Environmental magnetism: past, present, and future. *J. Geophys. Res.,* 100:2175–2192.

Wei, W., and Thierstein, H.R., 1991. Upper Cretaceous and Cenozoic calcareous nannofossils of the Kerguelen Plateau (southern Indian Ocean) and Prydz Bay (East Antarctica). *In* Barron, J., Larsen, B., et al., *Proc. ODP, Sci. Results,* 119: College Station, TX (Ocean Drilling Program), 467–494.

Winter, D.M., and Harwood, D.M., 1997. Integrated diatom biostratigraphy of late Neogene drillholes in Southern Victoria Land and correlation to Southern Ocean records. *In* Ricci, C.A. (Ed.), *The Antarctic Region: Geological Evolution and Processes.* Terra Antart. Publ., 985–992.

APPENDIX

Accessory Components

Accessories observed from residues prepared for examination of foraminifers are summarized in Table AT1. Samples below Sample 188-1166A-12R-CC are not included unless they contain accessories of significance. In this case, coal is common in Sample 188-1166A-14R-CC and wood is common in Sample 17R-CC, which is the uppermost limit of woody fragments that are commonly present below this depth. The presence of what appears to be bone in Sample 188-1166A-11R-1, 47–50 cm, is noteworthy. Sponge spicules and echinoid spines are indicators of fully marine conditions even in the absence of other marine indices such as foraminifers. Pyrite consists of crystalline aggregates and appears to be detrital in origin, as some is found in detrital sandstone grains. Black coal is probably detrital and is likely derived from the Permian Amery Group coals of the Prince Charles Mountains or underlying Lower Cetaceous sediment. Wood is taken to be from nearby sources or in situ, a component of the local depositional environment. Residues usually are large and of terrigenous material in this section. Most are moderately sorted, and a comment on sorting is made only if it is notably poor or good.

AT1. Summary of accessory components identified in foraminiferal residues, p. 110.

Sponge Spicules

Sponge spicules are conspicuous in modern sediments of Prydz Bay. However, with the exception of the 63- to 125-µm size fraction in Samples 188-1166A-1R-CC and 2R-CC and a horizon rich in sponge spicules (with simple diactinellid monaxon spicules to ~10 mm long) that occurs in Sample 188-1166A-2R, 72–73 cm, sponge spicules are either absent or very minor constituents at this site.

Bone

Sample 188-1166A-11R-1, 47–50 cm, contains what appears to be fragmented bone. Stereobinocular microscope examination of a fragment suggests that it has significant detail and deserves separate examination during shore-based studies. The fragments need to be reassembled, as the drilling process seems to have shattered the original into several tens of fragments.

Pre-Neogene Terrestrial Vegetation

Black coal fragments are present throughout the sequence, and based on observation, most are genuine coal that probably originated in the Permian Amery Group sequence of the Prince Charles Mountains region. A few trilete and bisaccate pollen or spores were recovered from diatom preparations of Samples 188-1166A-16R-2, 140–141 cm, and 16R-CC. The bisaccate forms are likely to be Permian; however, the source of the trilete is not as clear. They could be from the same source as the wood fragments in Sample 188-1166A-17R-CC.

Wood fragments, <0.5 mm long, first appear downhole at Sample 188-1166A-17R-CC (the top of lithostratigraphic Unit III) and in several samples below that. Under the microscope, the small fragments retain flexibility and orange-brown color when wet. Wood and cuticle details are clearly visible in mounted slides of the material. These wood frag-

ments are different in color and preservation from the woody structure that is visible in some of the black coal fragments that accompany most samples.

In Sample 188-1166A-25R-2, 0–5 cm, there are fragments as large as 8–9 mm in diameter of dark brown lignified wood, which contrasts strongly with the Permian black coal. Woody structures are well preserved. Sample 188-1166A-27R-CC consists mostly of wood in fragments as large as 20 mm. The rest is quartz sand and mica, suggesting deposition in a swamp environment. There is ample wood that is well enough preserved to allow reconstruction of the vegetation at the time.

The wood fragments provide clear evidence of coeval terrestrial vegetation during deposition of Samples 188-1166A-17R-CC to 28R-CC, which immediately underlie material that is dated on other bases as latest Eocene–earliest Oligocene in age.

The features of this material contrast with descriptions of Lower Cretaceous coals recovered from Hole 741A during Leg 119, Cores 119-741A-5R to 14R in the interval 23.9–128.1 mbsf, indicating strongly that the lignitic matter encountered in Hole 1166A is Tertiary (or possibly Upper Cretaceous) material close to its origin. The woody tissue is very well preserved in many samples.

Descriptions of the Lower Cretaceous coals encountered during Leg 119 indicate that they are different (Turner and Padley, 1991). The core descriptions in the Leg 119 *Initial Reports* volume (Barron, Larsen et al., 1989) give much more information. The coals recovered during Leg 119 are black, apparently rich in charcoal, and lack obvious woody tissues. The Leg 119 Shipboard Scientific Party (1989b) summary of the occurrence recorded the coal as allochthonous "finely disseminated organic matter and carbonized plant fragments" and referred to "dark, organic-rich sediment." In Hole 1166A material, woody material is very abundant, still flexible when wet, and brown lignitic rather than black coal.

Figure F1. Location of Site 1166, slightly offset from seismic line BMR 33-23P3 and ~40 km southwest of ODP Site 742. The site is in 475 m of water, and the seafloor is extensively ploughed by icebergs.

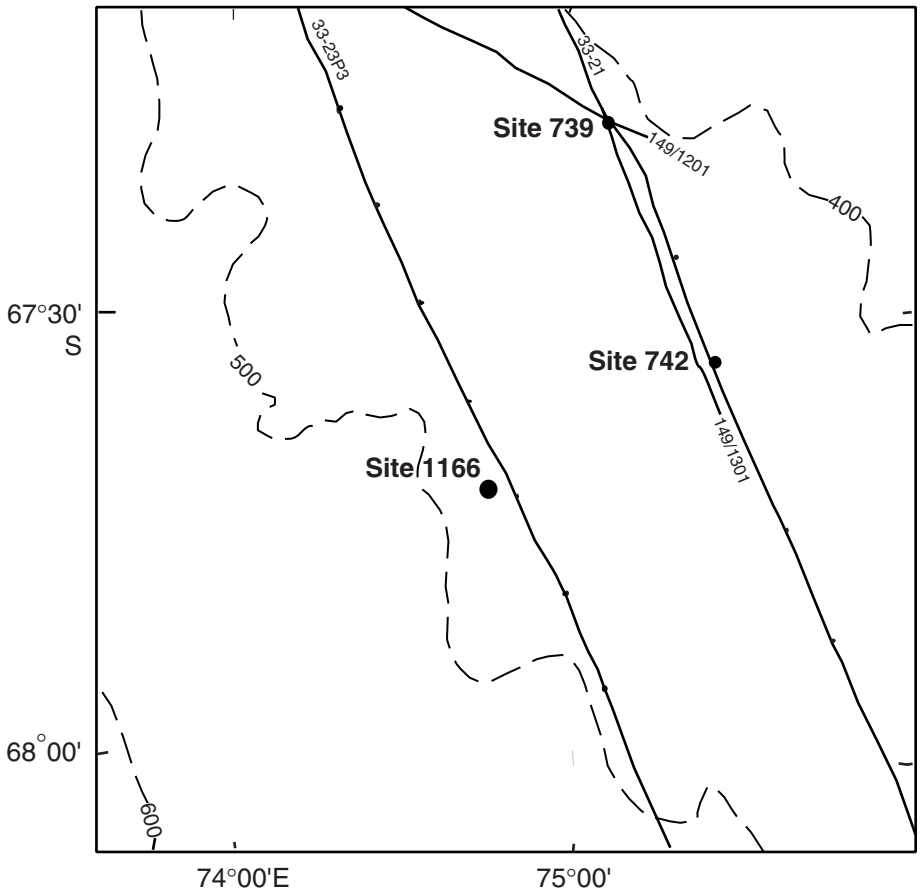

Figure F2. Seismic line BMR 33-23P3 at Site 1166 showing major surfaces. From top to bottom: base of the Pliocene–Pleistocene, intra-Paleogene erosion surface, and top of the Cretaceous (PS.2B). SP = shotpoint.

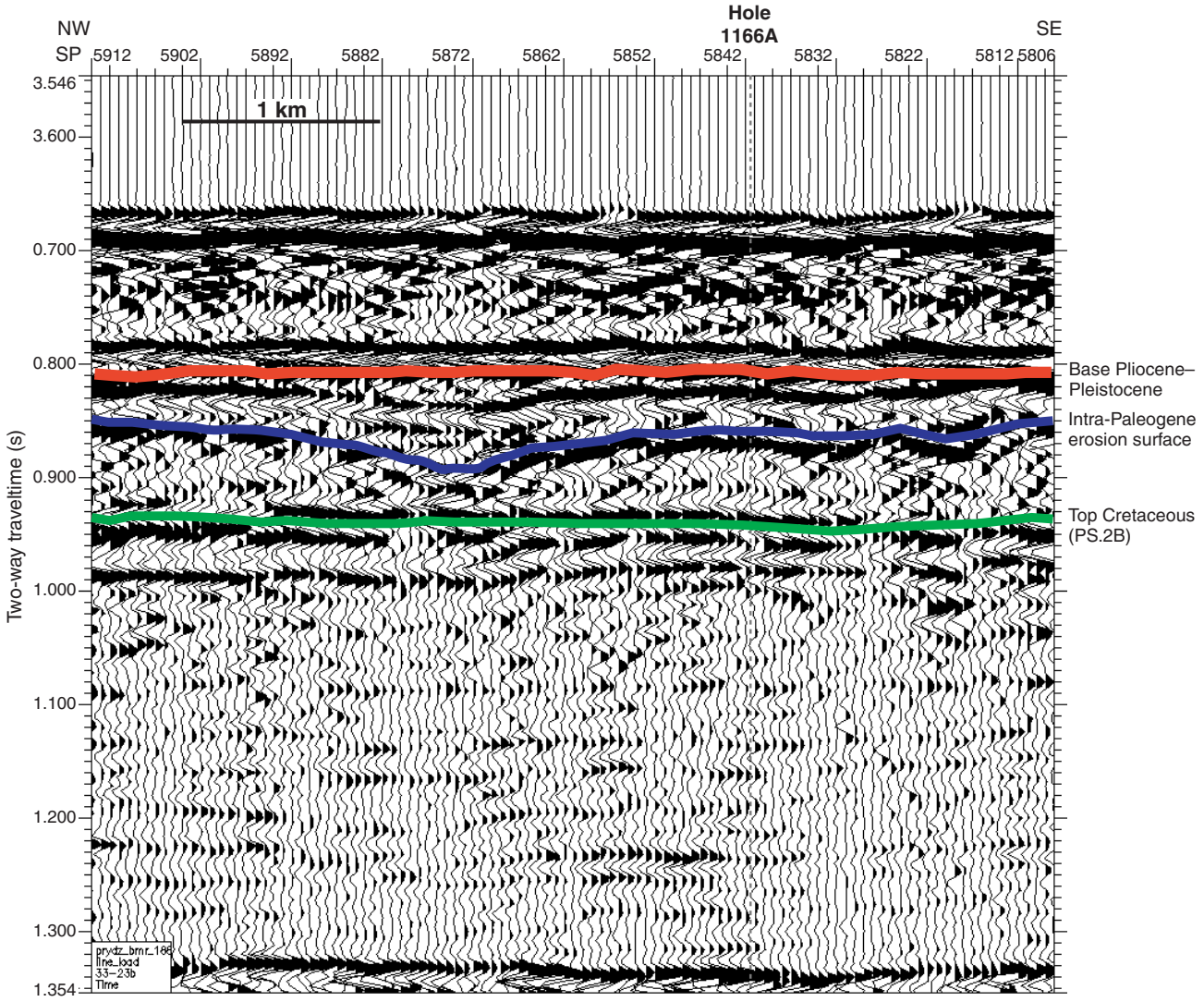

Figure F3. Site 1166 lithostratigraphic units, subunits, and interpretation.

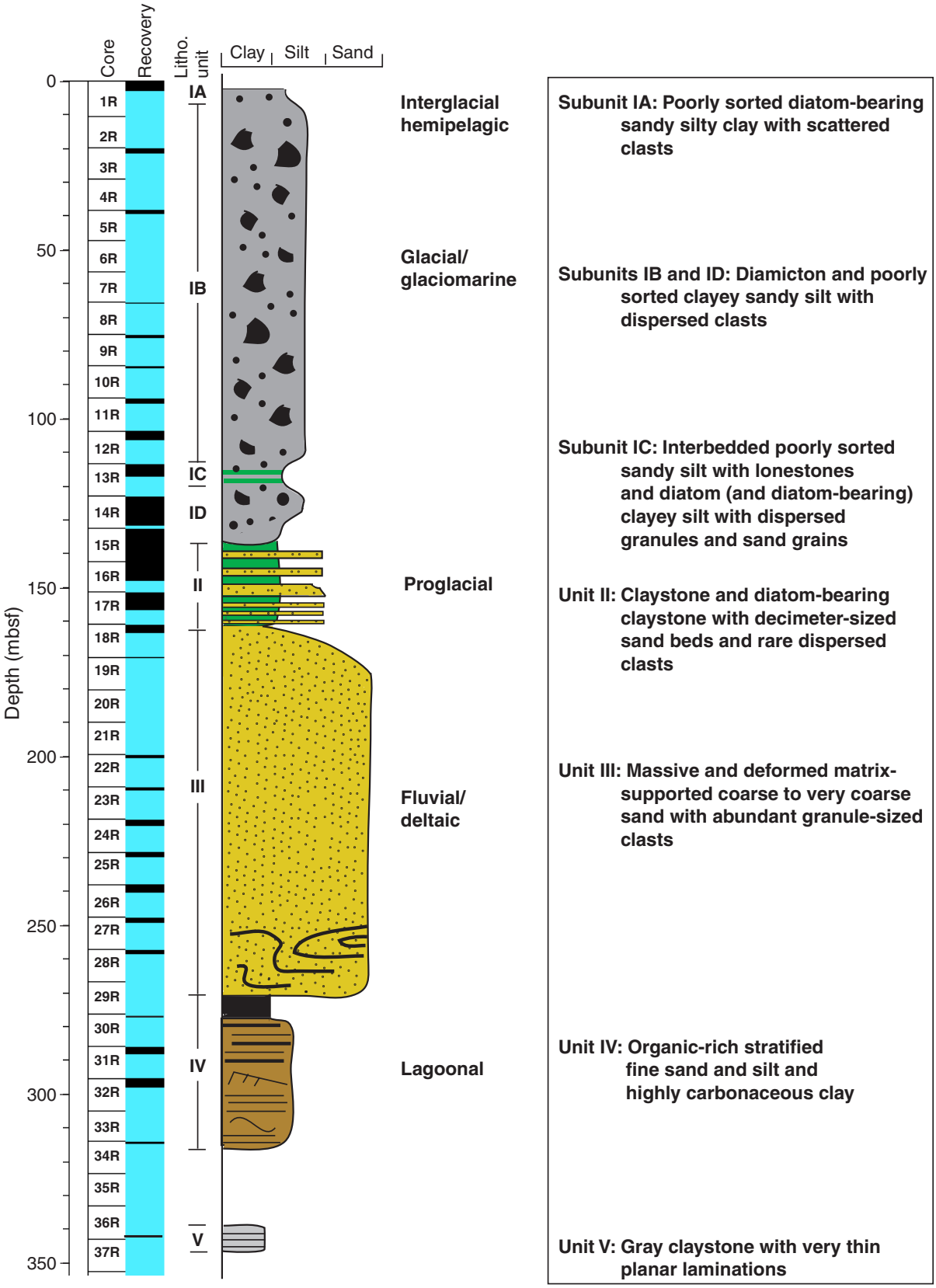

Figure F4. Composite stratigraphic section for Site 1166 showing core recovery, a simplified summary of lithology, lithologic unit boundaries, and age. Gamma-ray and resistivity curves are derived from wireline logs (see **"Downhole Measurements,"** p. 36) along with minerals identified by XRD. XRD shows the percentage of most abundant minerals. This graph was plotted using the methods of Forsberg et al. (1999).

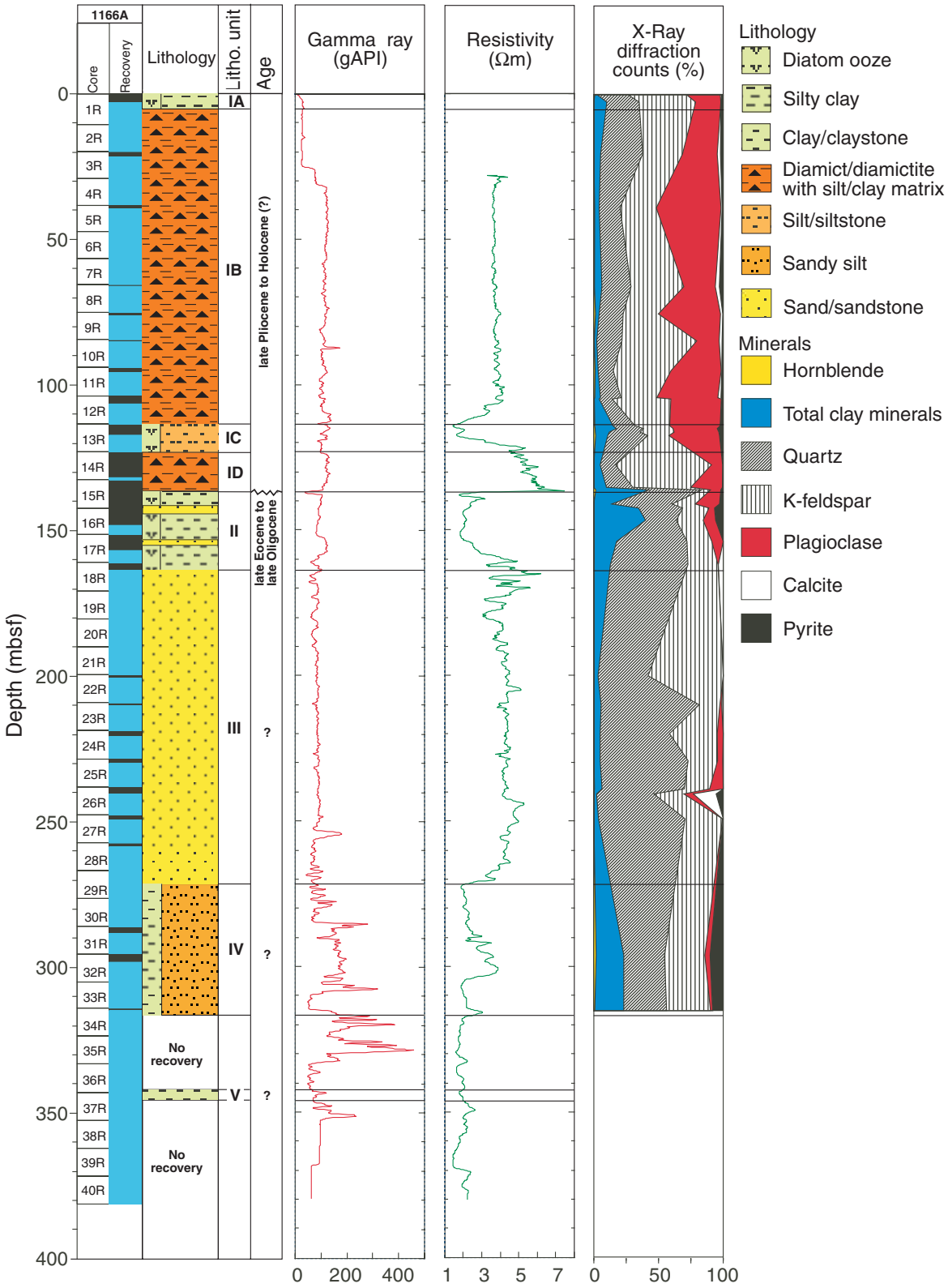

Figure F5. Diamicton typical of Subunit IB (interval 188-1166A-3R-1, 97–108 cm).

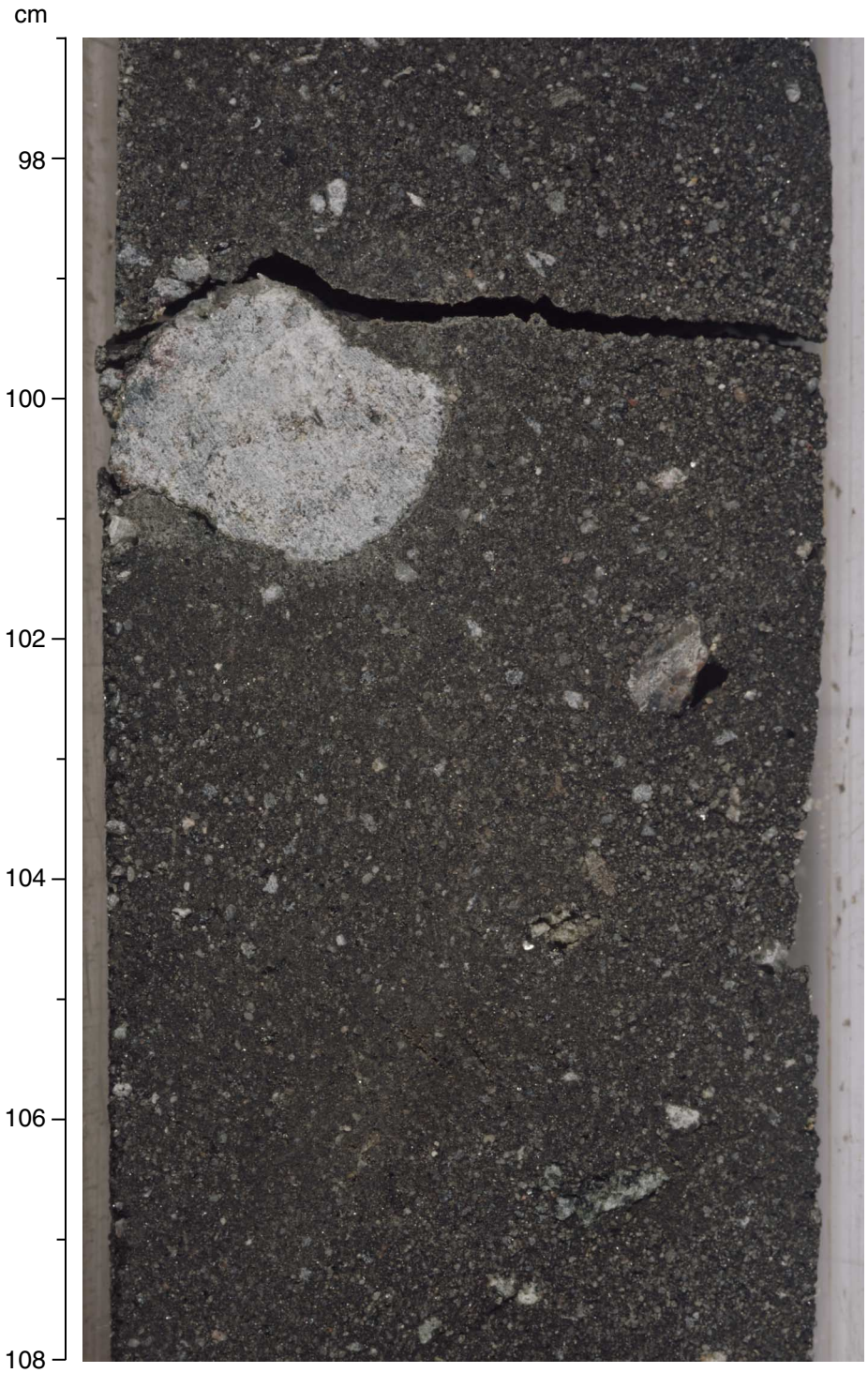

Figure F6. Upper contact of interbedded clays and diatom clays of Subunit IC (interval 188-1166A-13R-1, 100–125 cm).

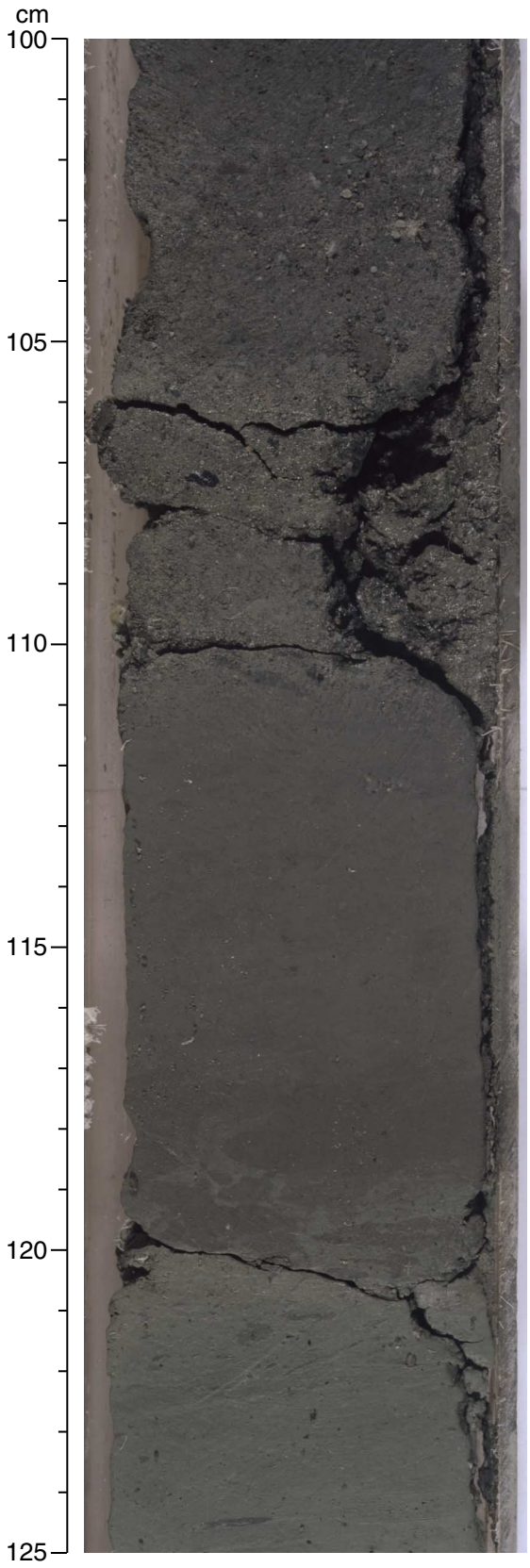

Figure F7. Interbedded clays and diatom clays of Subunit IC (interval 188-1166A-13R-2, 40–60 cm).

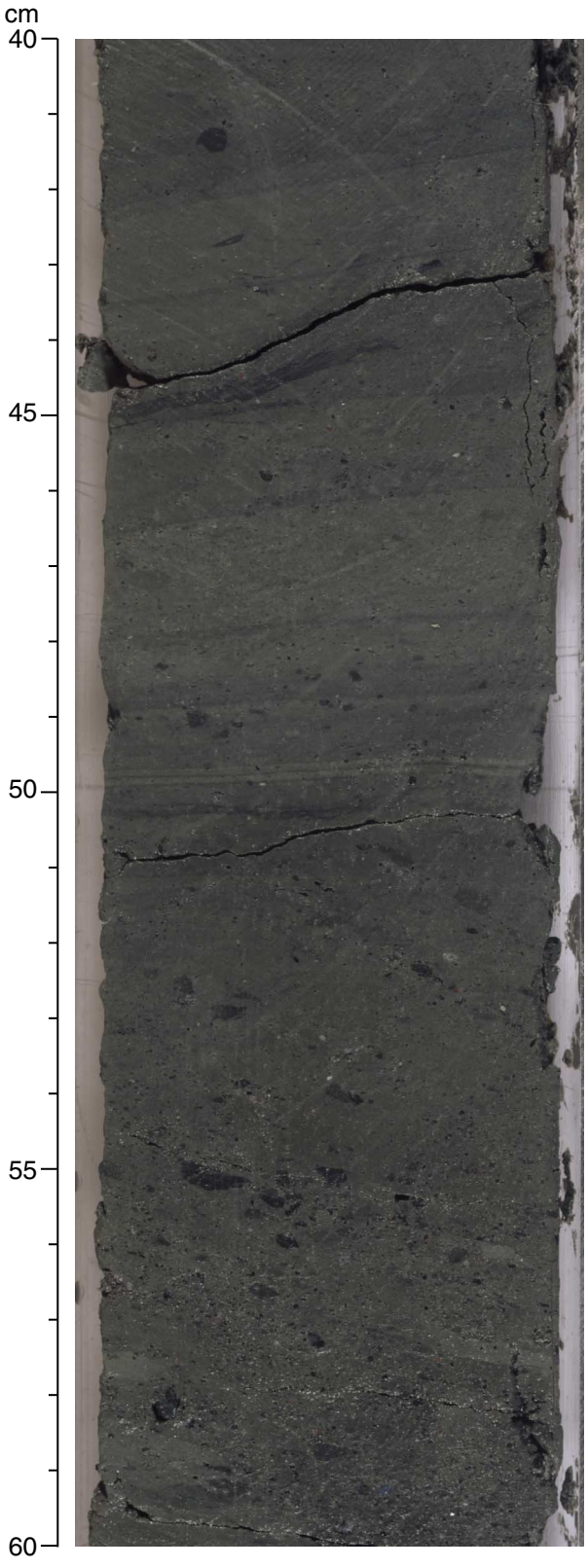

Figure F8. Decimeter-scale interbedded clays and sands of Unit II (interval 188-1166A-16R-2, 95–119 cm).

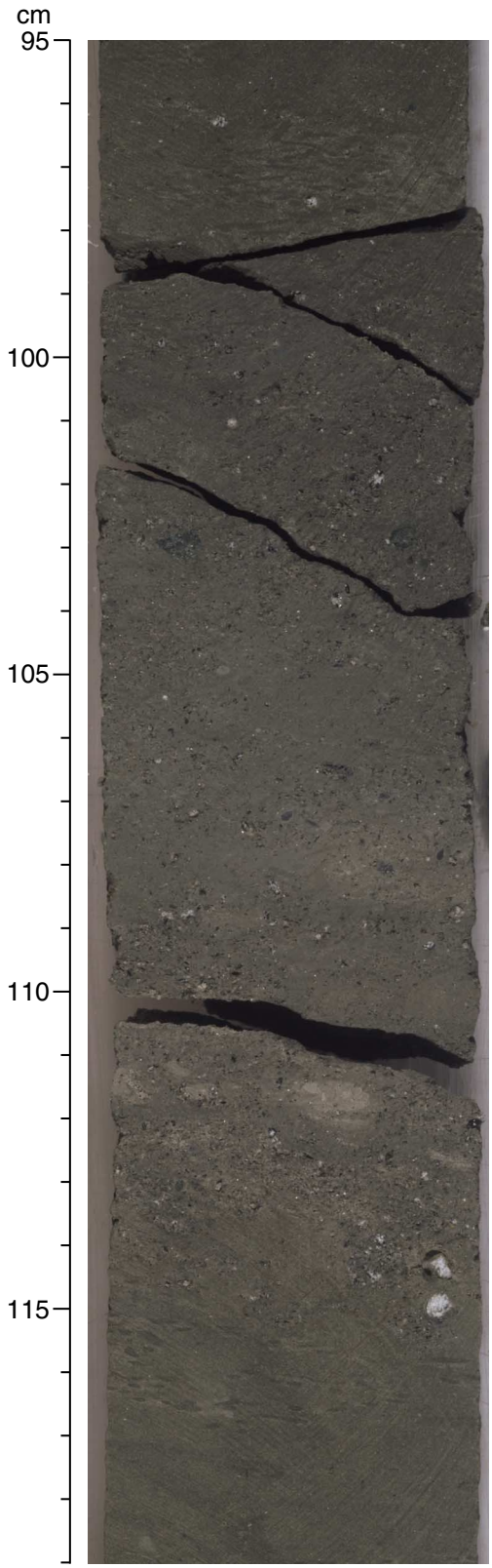

Figure F9. Graded sand bed in the upper portion of Unit II (interval 188-1166A-15R-6, 40–70 cm).

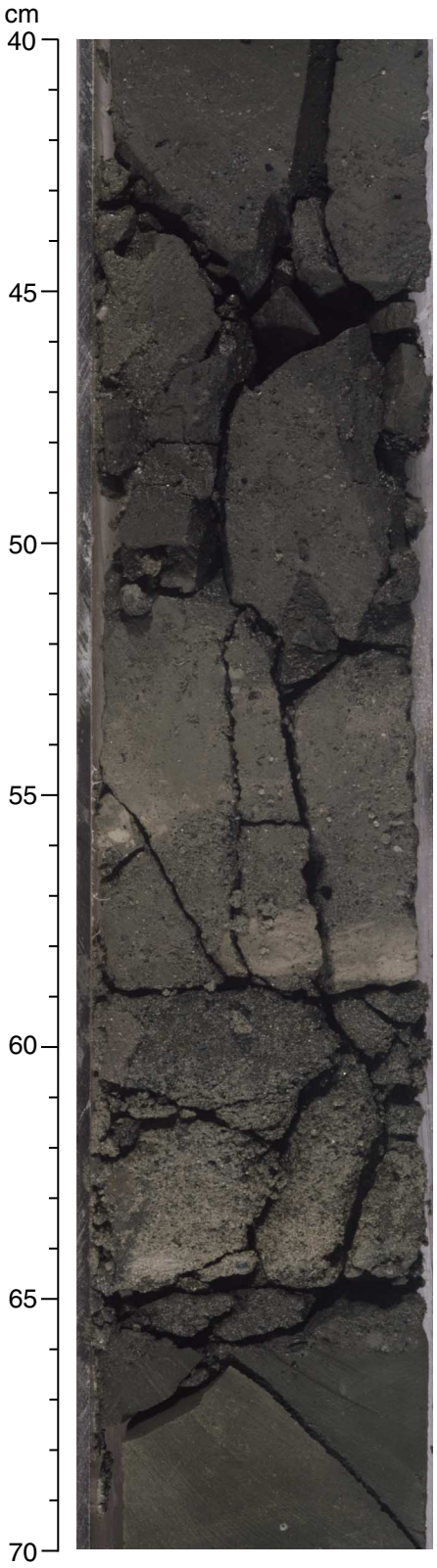

Figure F10. Centimeter-scale rhythmically interbedded clays and sands of Unit II (interval 188-1166A-17R-3, 23–43 cm).

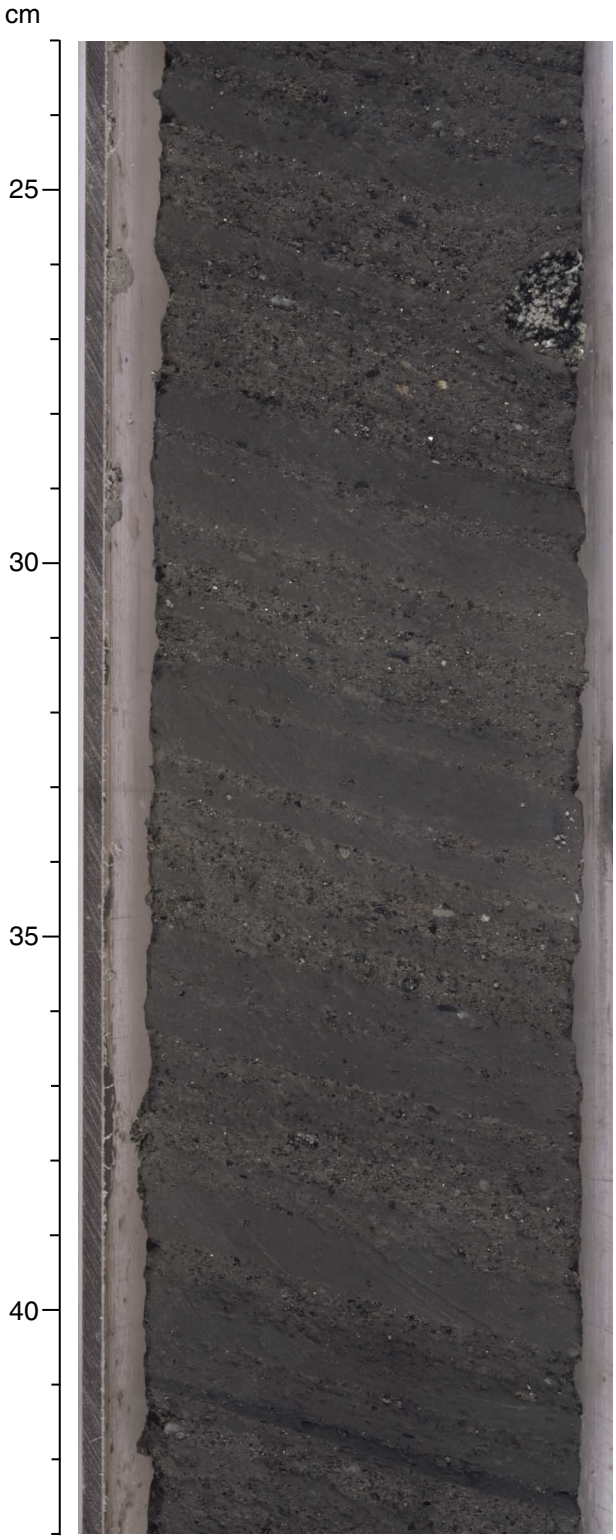

Figure F11. Homogeneous coarse sands typical of the upper portion of Unit III (interval 188-1166A-18R-1, 55–75 cm).

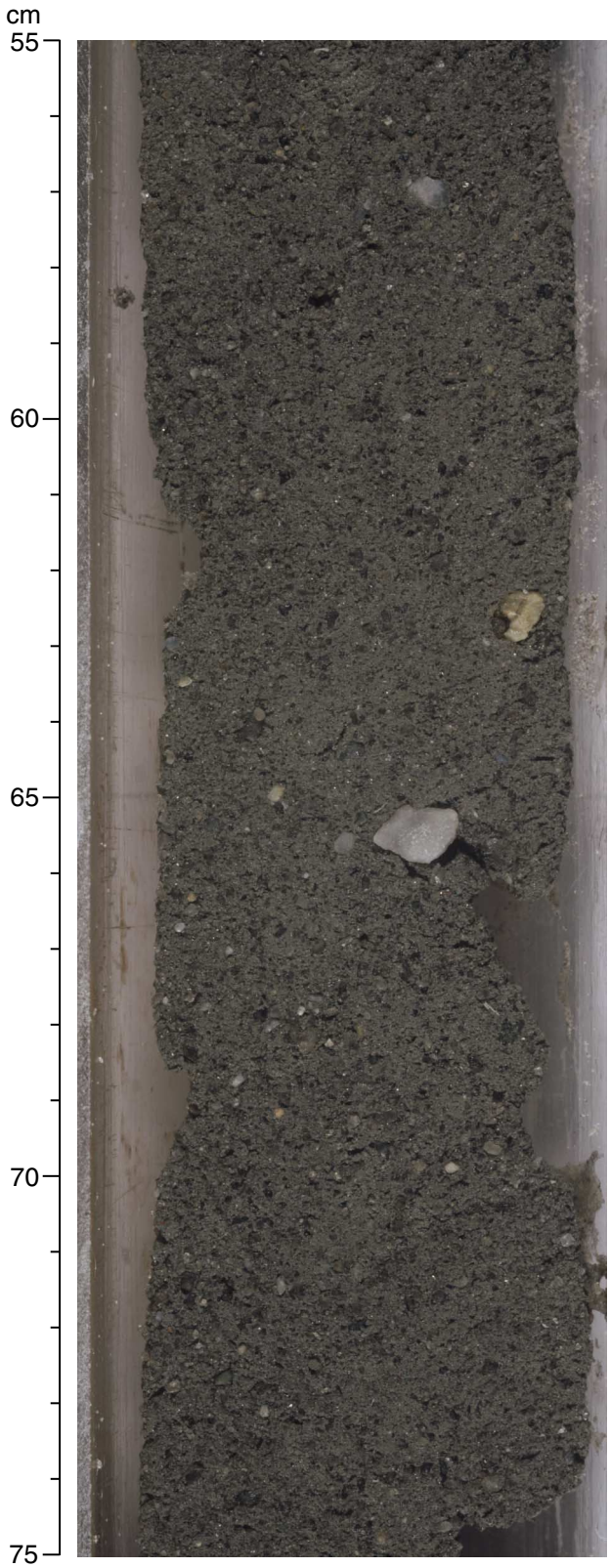

Figure F12. Deformed coarse sands and color banding typical of the lower portion of Unit III (interval 188-1166A-28R-1, 128–145 cm).

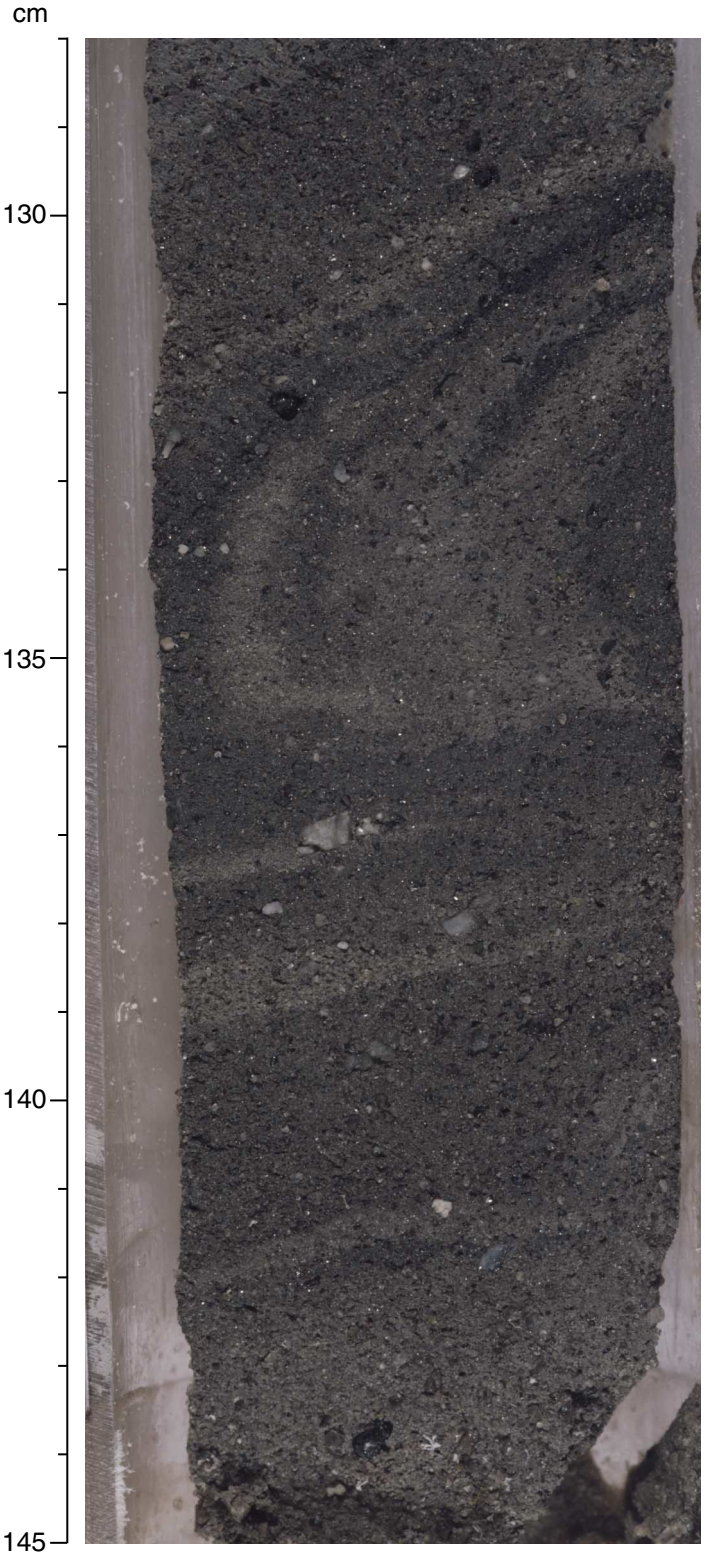

Figure F13. Deformed coarse sands and organic detritus within Unit III (interval 188-1166A-28R-1, 34–59 cm).

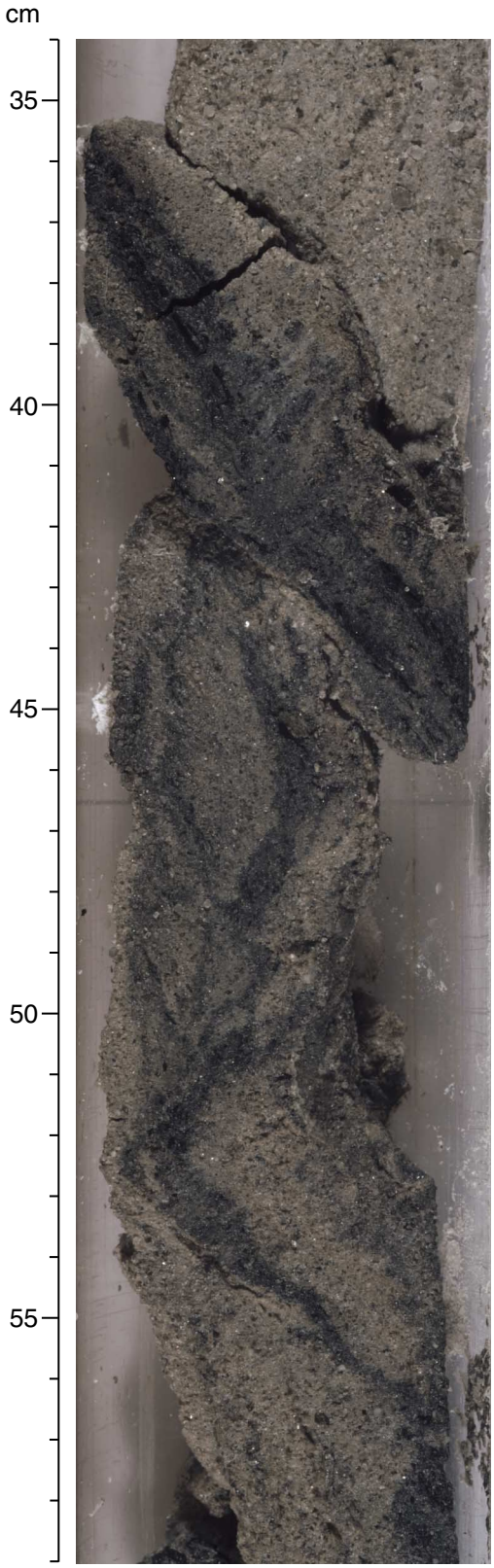

Figure F14. Laminated micaceous silt and organic detritus typical of Unit IV (interval 188-1166A-31R-1, 4–28 cm).

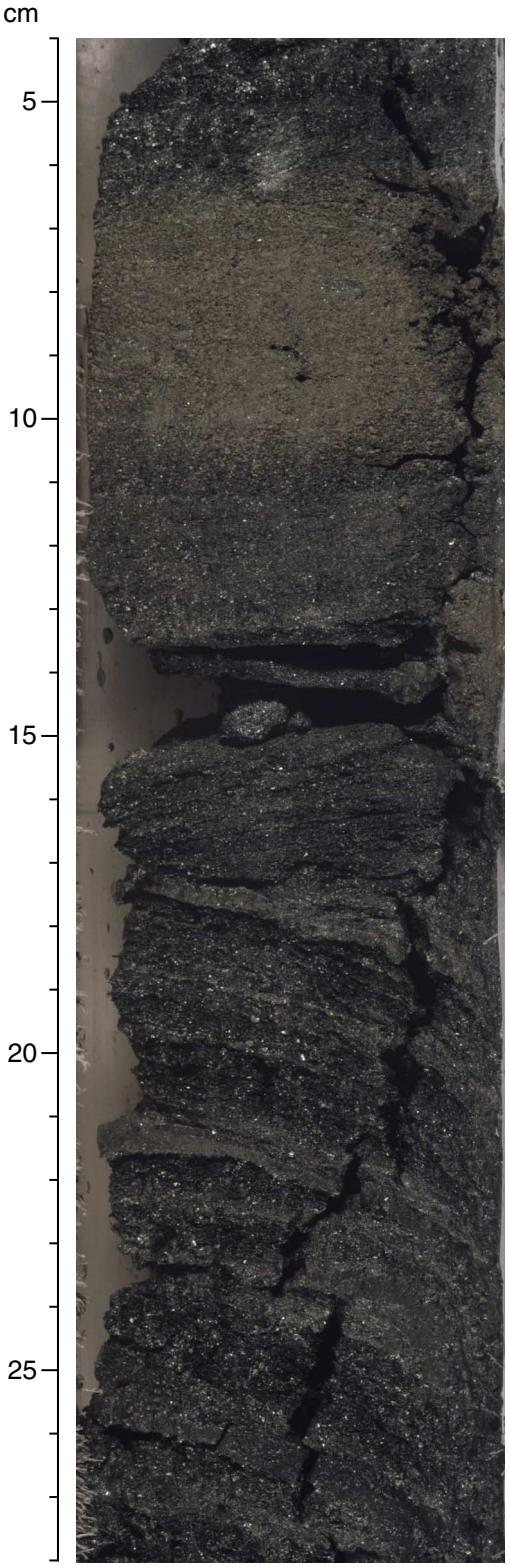

Figure F15. Combined percentages of muscovite and biotite mica from smear slides.

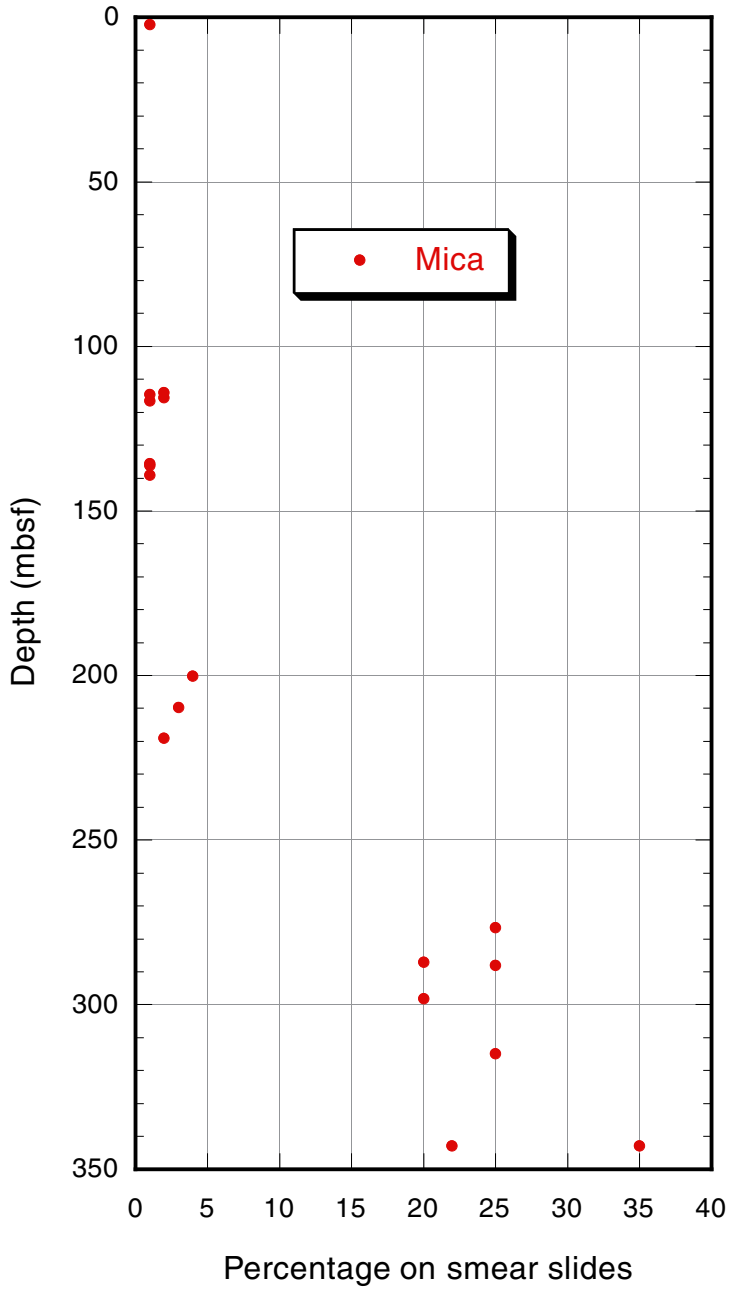

Figure F16. X-ray diffractograms of clay-sized fractions of sediment from Samples 188-1166A-12R-1, 45–46 cm (Subunit IB), and 13R-1, 143–145 cm (Subunit IC).

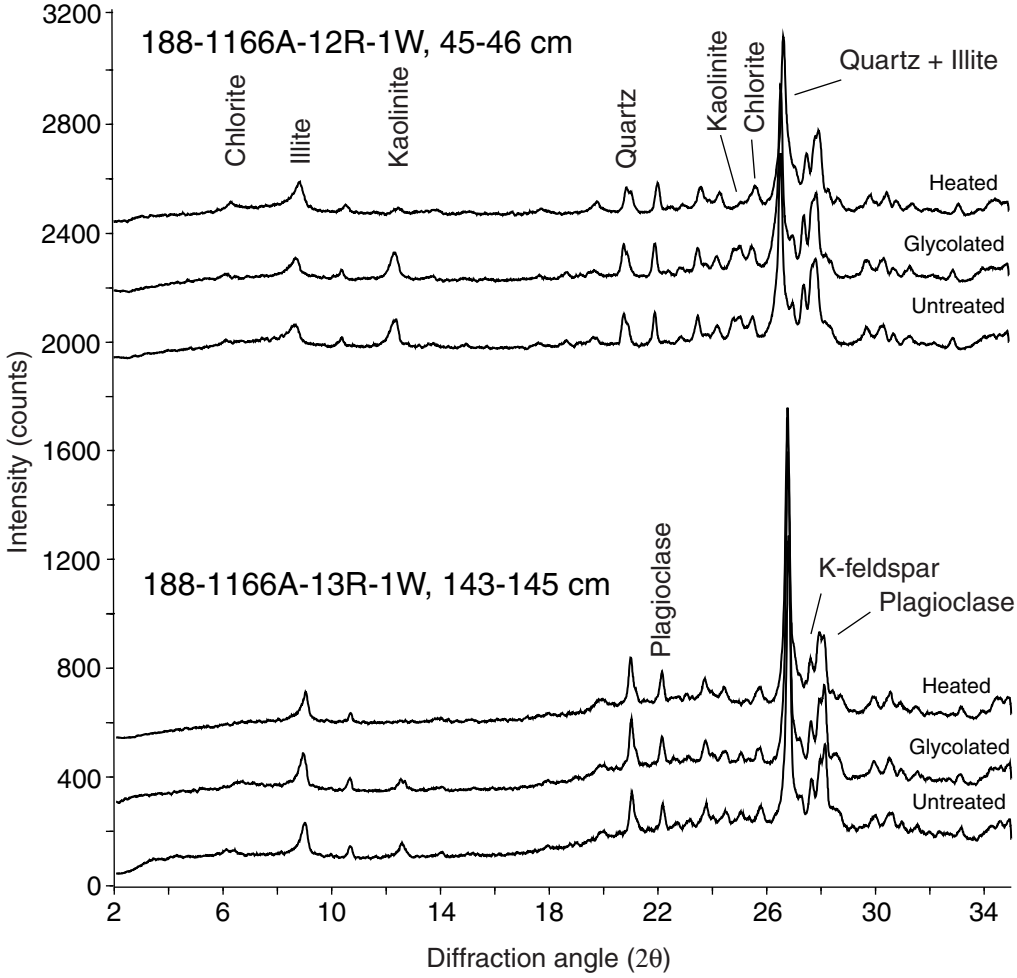

Figure F17. X-ray diffractograms of clay-sized fractions of sediment from Samples 188-1166A-14R-3, 120–121 cm (Subunit ID), and 15R-3, 24–25 cm (Unit II).

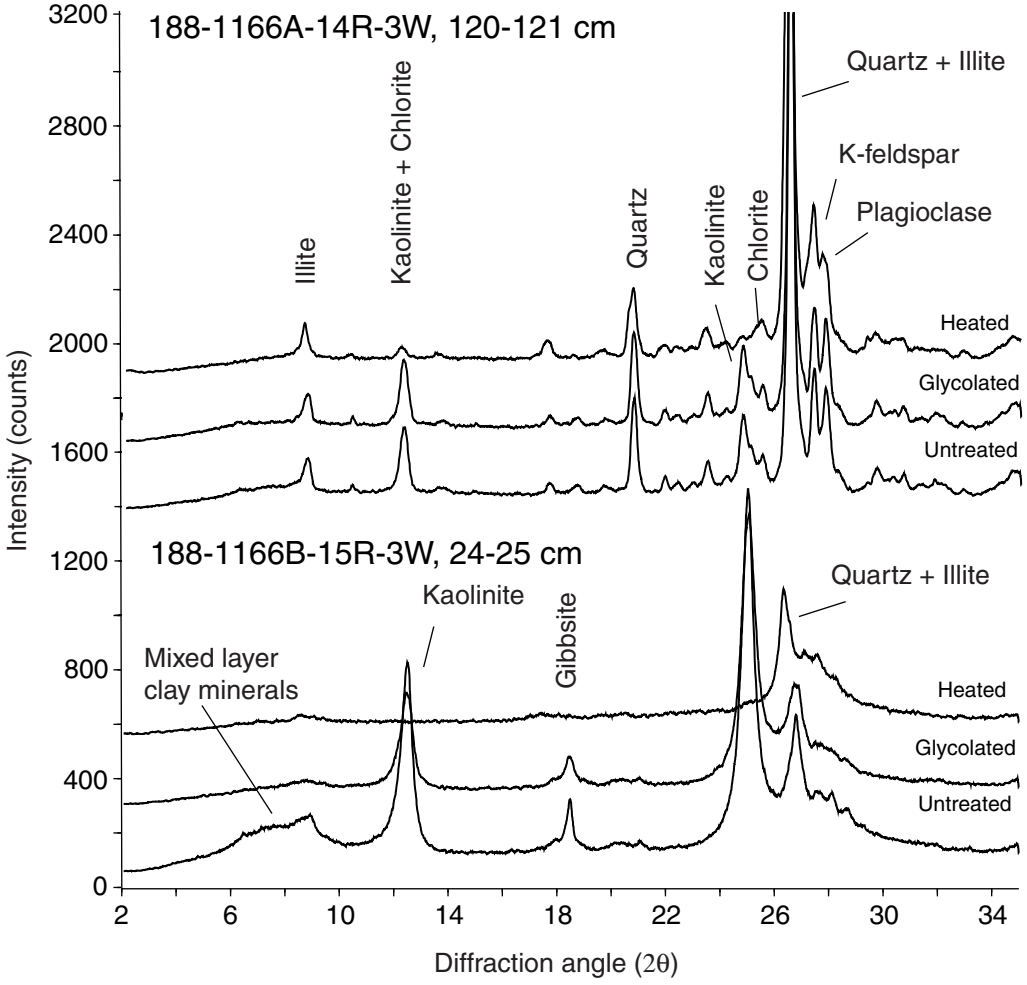

Figure F18. X-ray diffractograms of clay-sized fractions of sediment from Samples 188-1166A-24R-1, 107–108 cm (Unit III), and 32R-1, 25–26 cm (Unit IV).

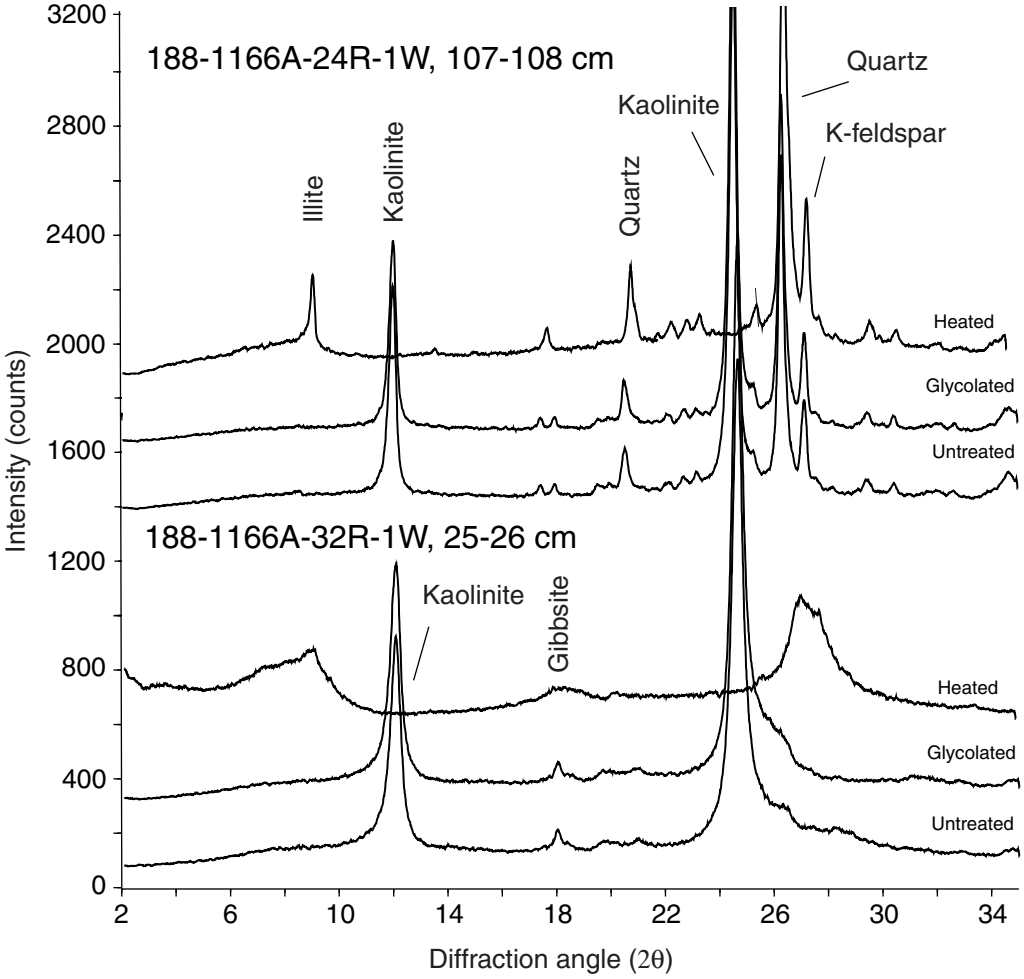

Figure F19. Graphical summary of core recovery, lithostratigraphic units, magnetostratigraphy, and biostratigraphic zones for Hole 1166A. See **"Lithostratigraphy,"** p. 9, for explanation of lithostratigraphic units. In "Polarity" column, black = normal and white = reversed polarity.

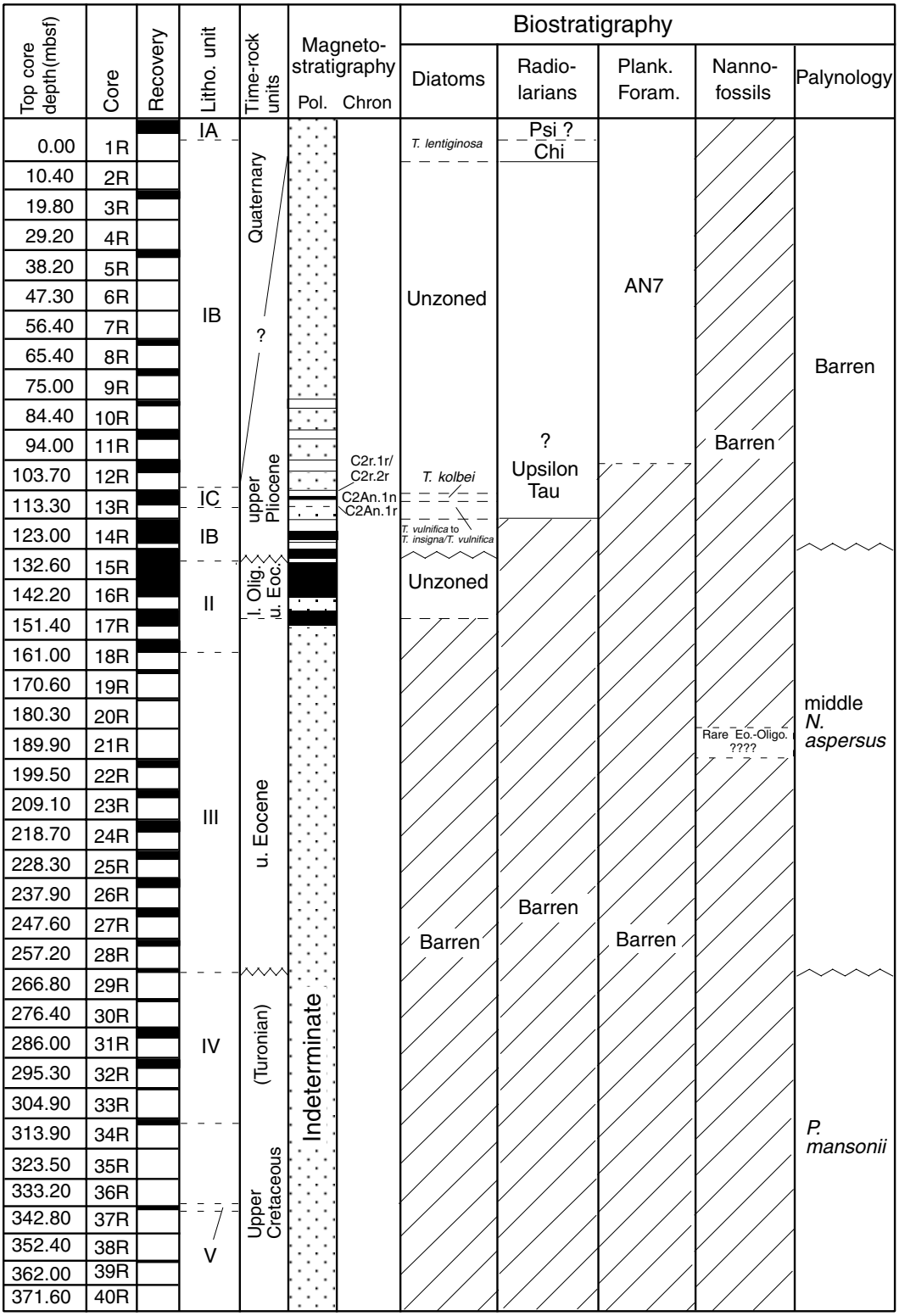

Figure F20. Age-depth plot for Hole 1166A. FO = first occurrence; LO = last occurrence.

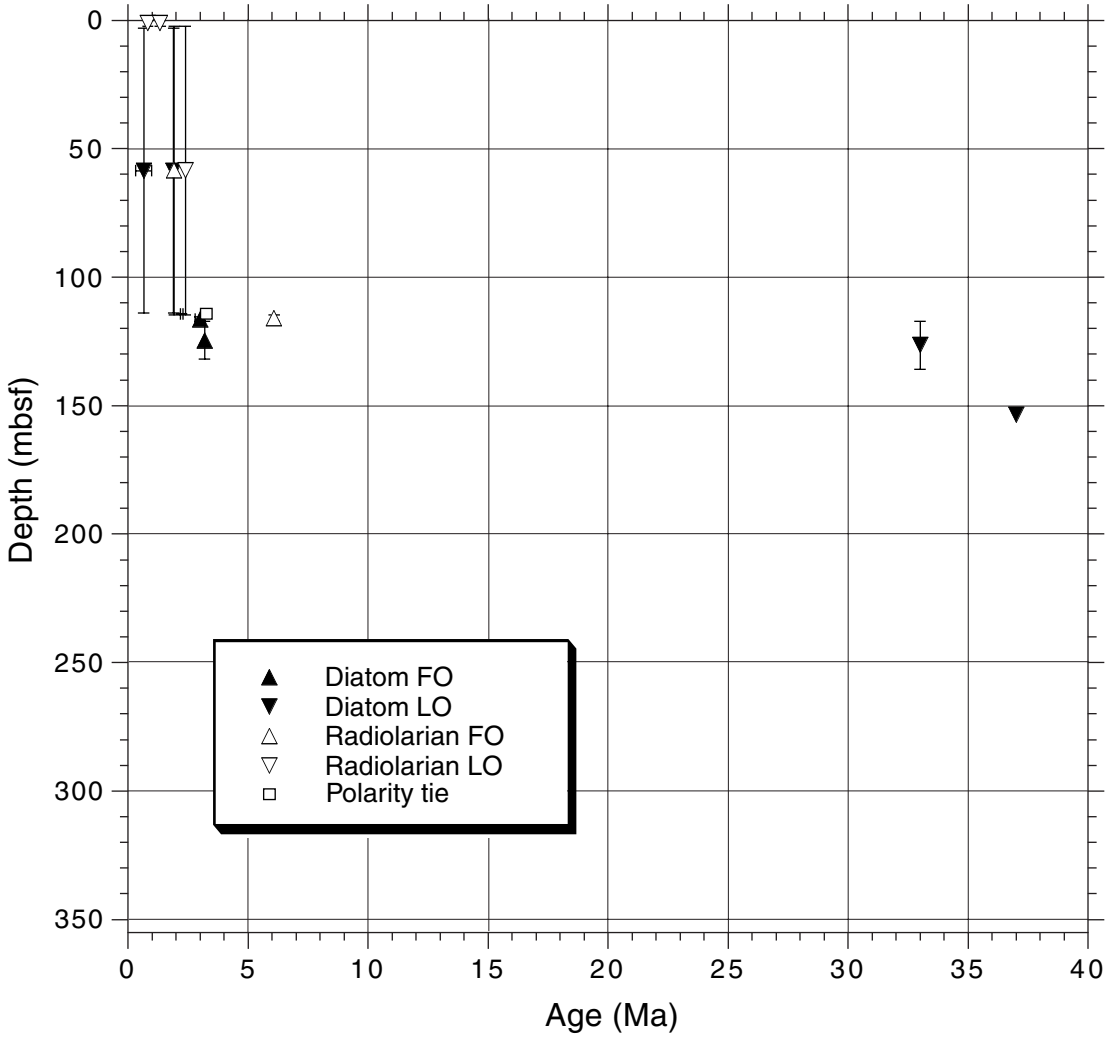

Figure F21. Downhole variation of concentration-dependent parameters (k, ARM, and IRM) in Hole 1166A. The horizontal lines and annotations indicate the position of the lithostratigraphic boundaries (see "Lithostratigraphy," p. 9). ARM = anhysteretic remanent magnetization; IRM = isothermal remanent magnetization.

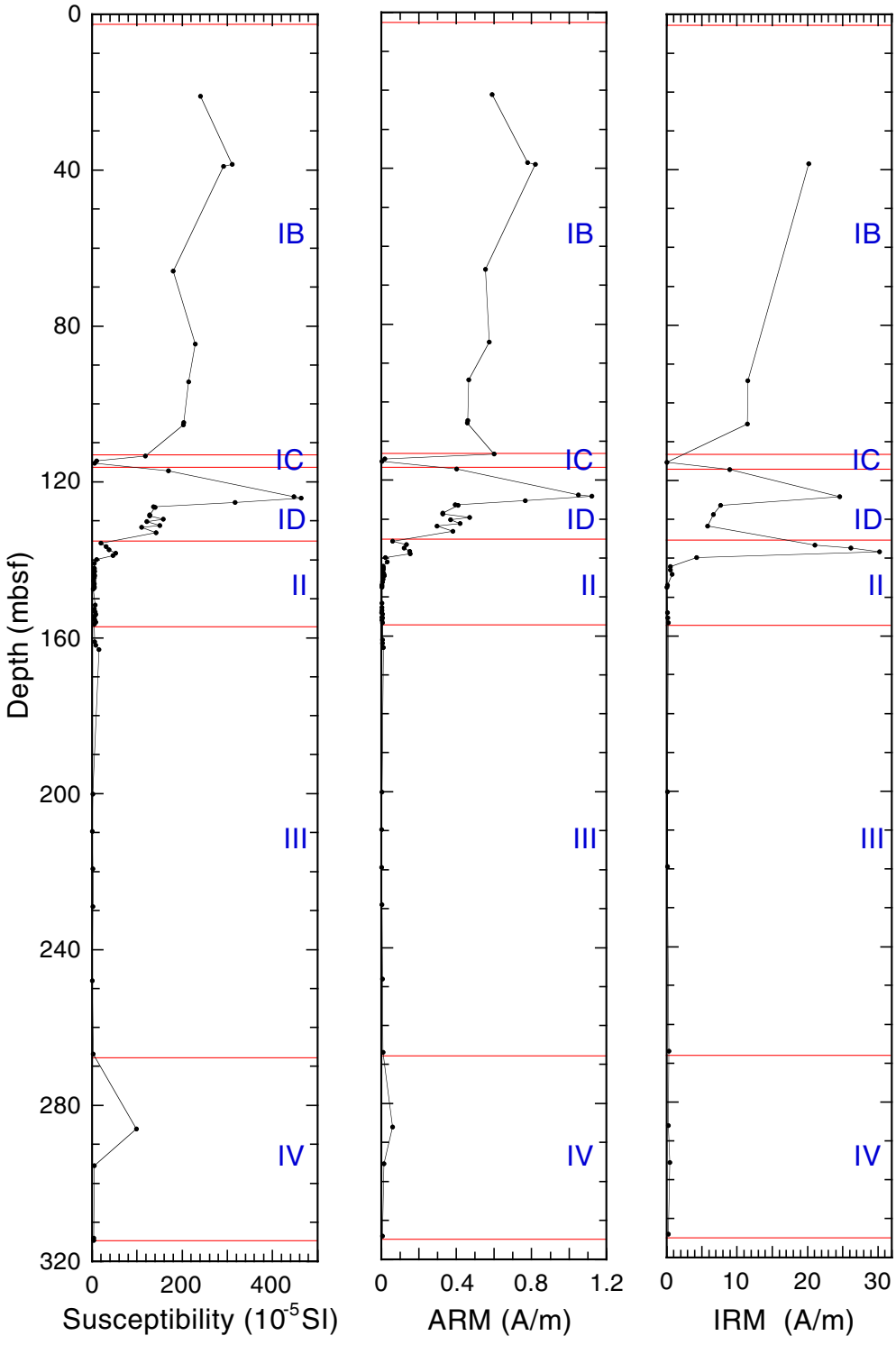

Figure F22. IRM acquisition curves for four representative samples from Hole 1166A. Saturation of IRM is reached in fields of 0.2–0.3 T.

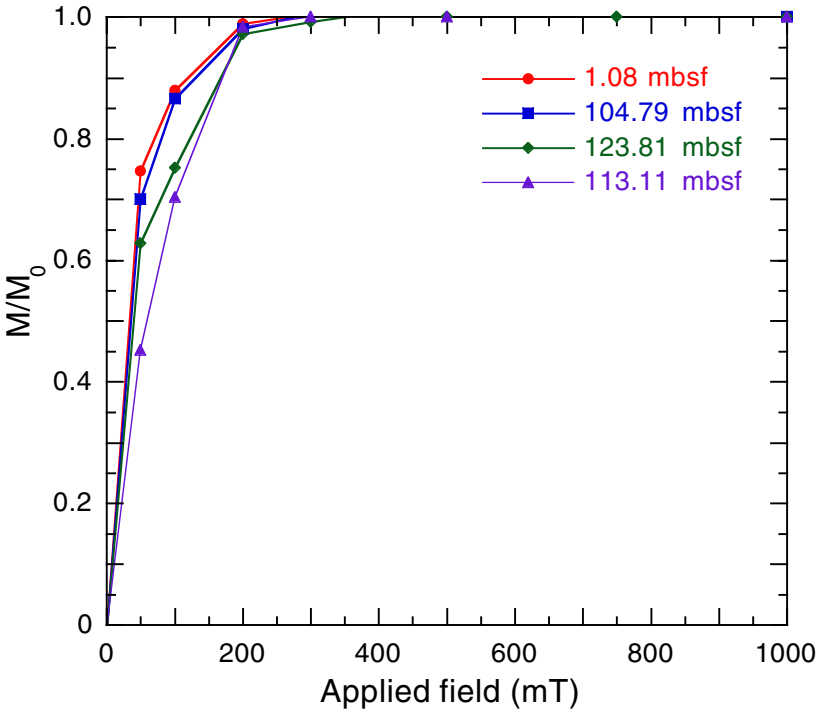

Figure F23. Thermal demagnetization of a composite three-axis IRM (Lowrie, 1990) for two representative samples from 21.08 (lithostratigraphic Unit IB) and 248.04 mbsf (lithostratigraphic Unit III).

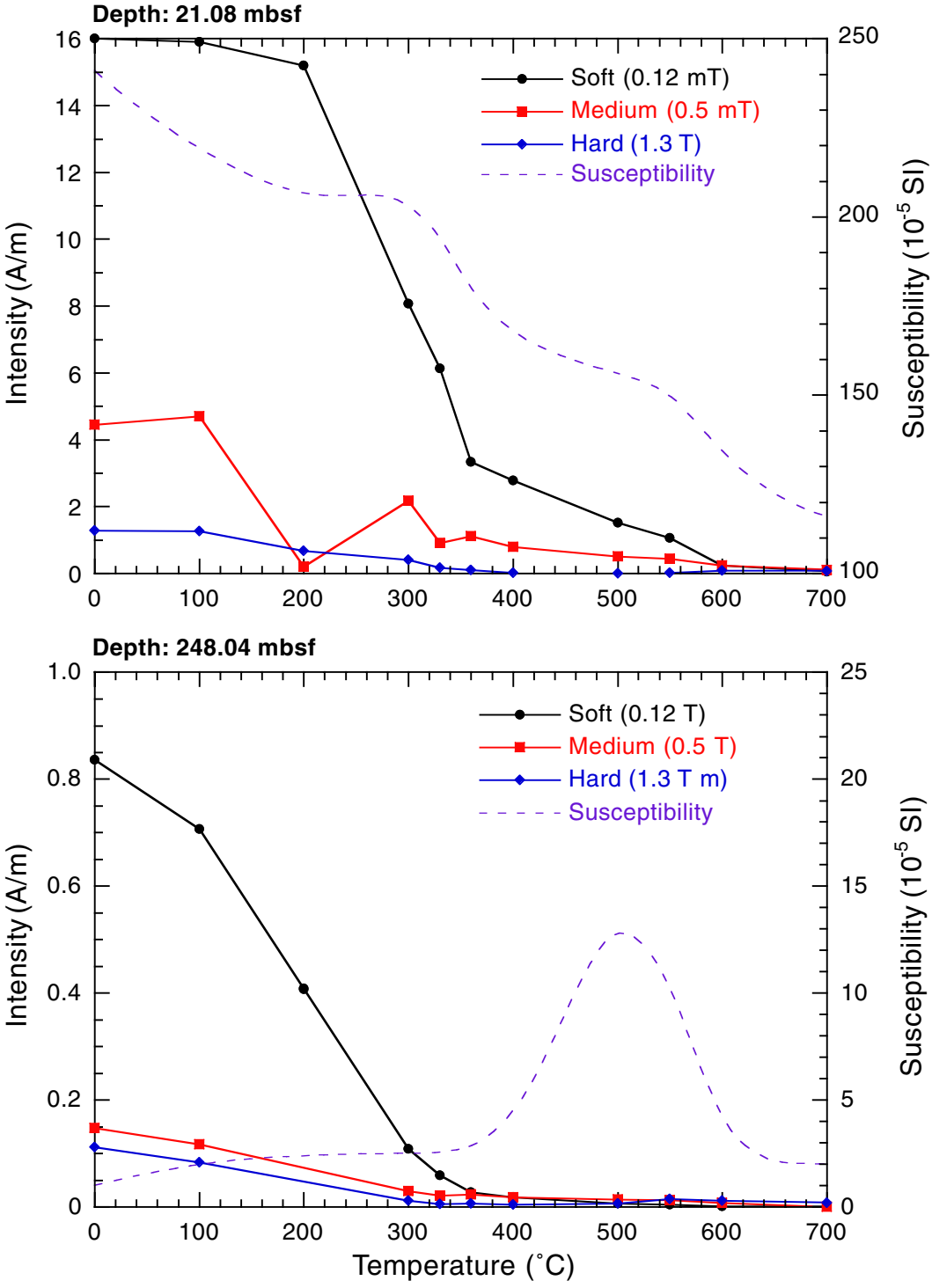

Figure F24. Vector component diagrams (with normalized intensity decay plots) of demagnetization (AF) behavior of four samples from Hole 1166A. Open symbols = projections onto the vertical plane; solid symbols = projections onto the horizontal plane. Numbers denote demagnetization levels in milliteslas. Dashed lines = linear regression fits that indicate the characteristic remanence component for each sample. The stereoplots are equal-area projections, with open symbols indicating upper hemisphere projections and solid symbols indicating lower hemisphere projections. The core is not azimuthally oriented; therefore, the declination values are not meaningful. NRM = natural remanent magnetization. (**Figure shown on next page.**)

Figure F24 (continued). (Caption shown on previous page.)

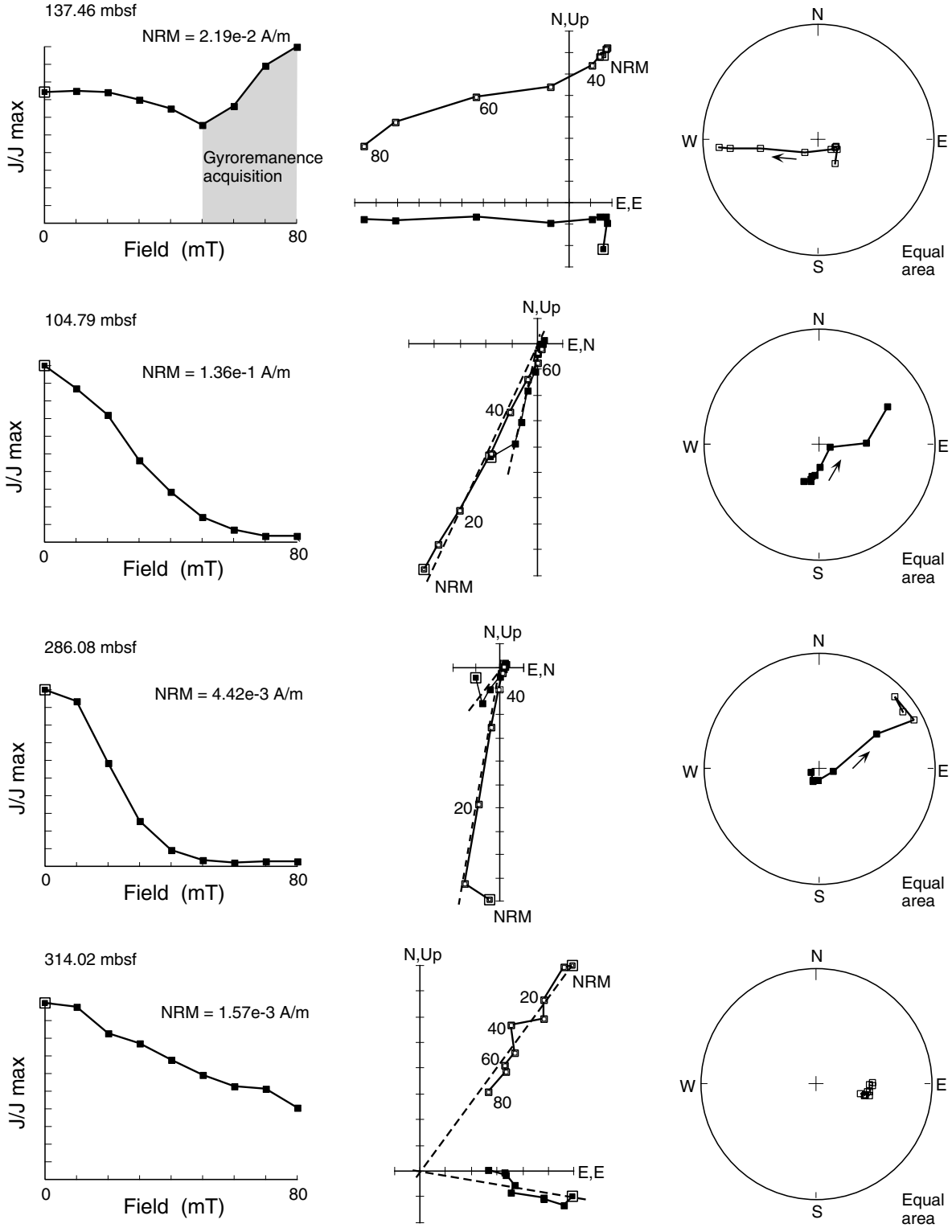

Figure F25. Histogram of paleomagnetic inclinations from Hole 1166A.

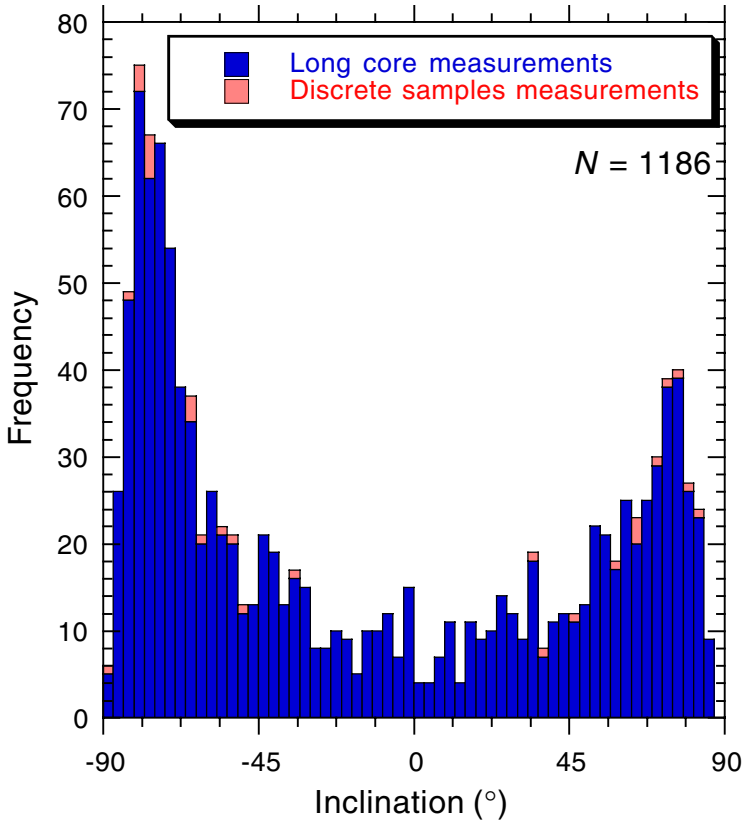

Figure F26. Magnetostratigraphic record from Hole 1166A (0–320 mbsf). Plot of NRM intensity, inclination after demagnetization at 30 mT, and an enlargement of the polarity data for the interval between 80 and 160 mbsf (shaded area). The inclinations obtained from split cores are compared with inclinations from stepwise-demagnetized discrete samples (solid circles). Inclinations for discrete samples were determined by linear regression fits to multiple demagnetization steps. Polarity is shown on the log to the right. The depths of polarity boundaries and major disconformities are also indicated. Chron ages for polarity reversal boundaries are from Berggren et al. (1995). LO = last occurrence.

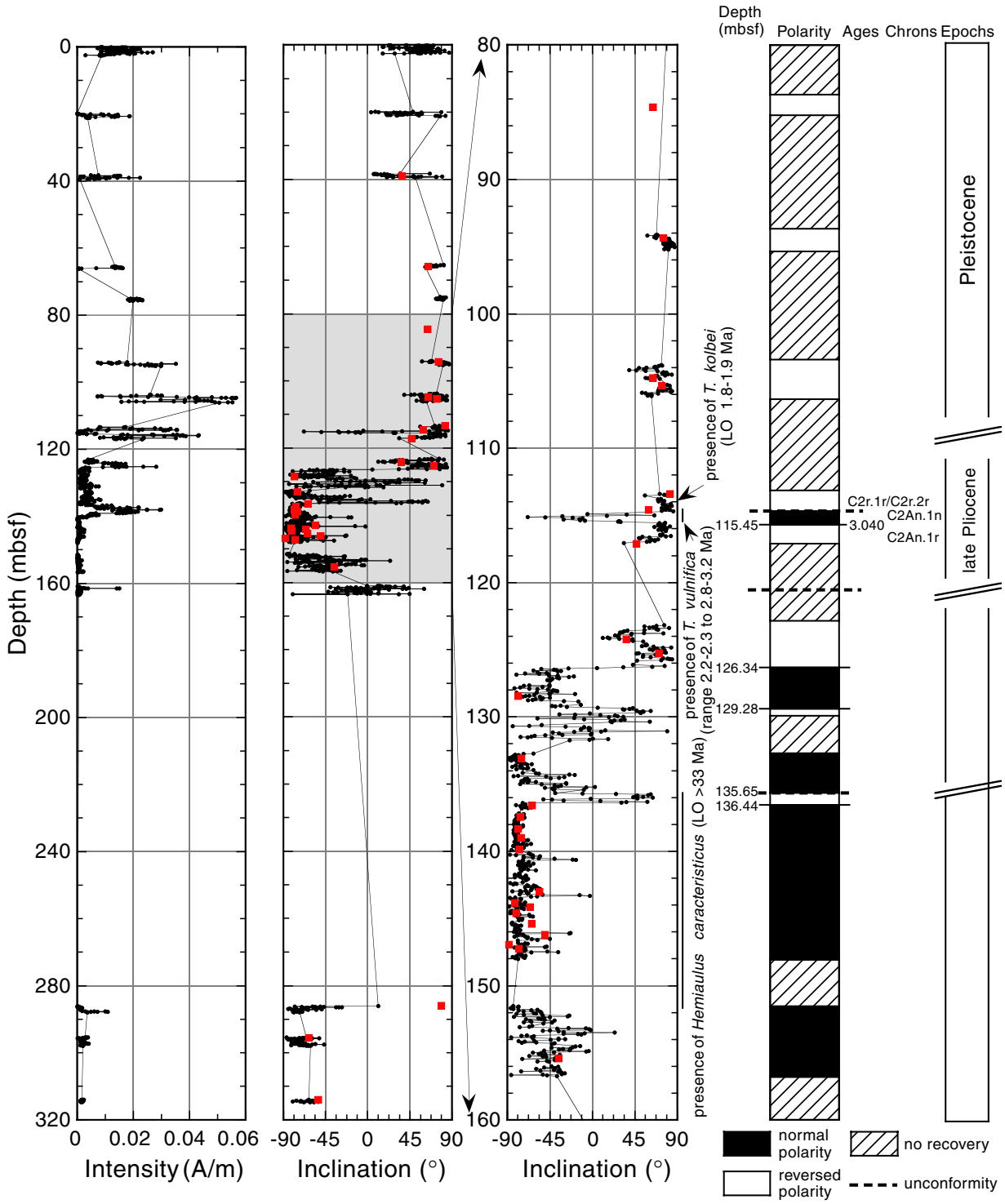

Figure F27. Downcore profiles of sulfate and ammonium at Site 1166.

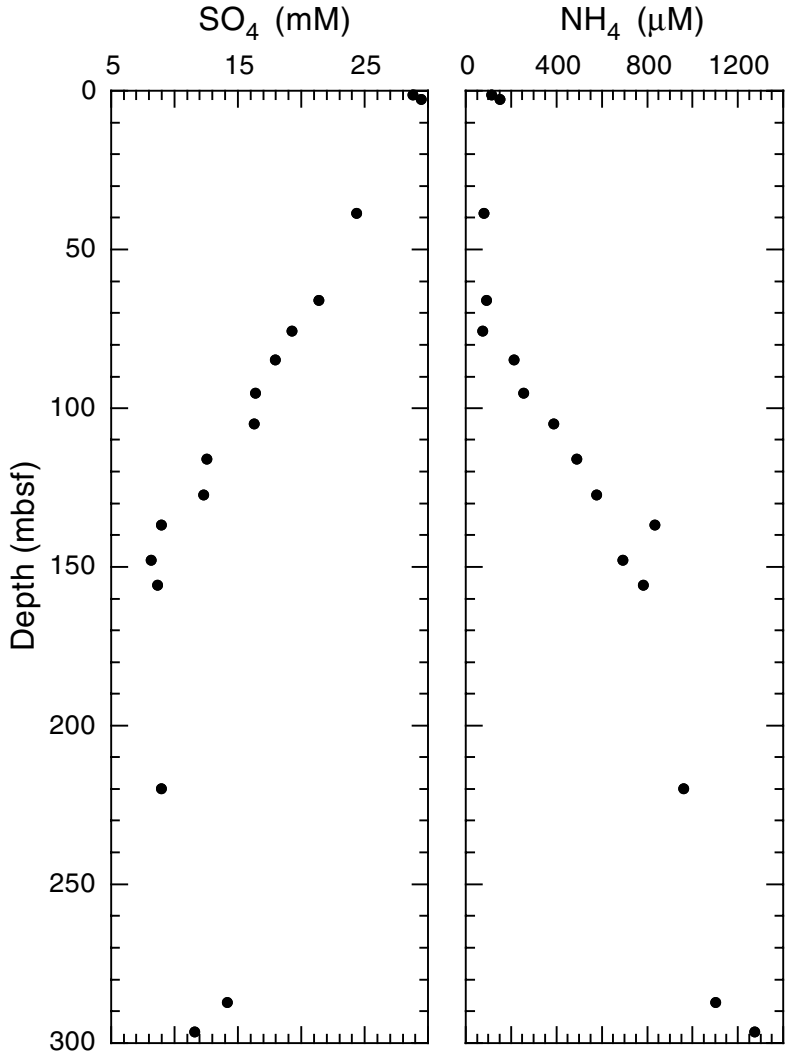

Figure F28. Downcore profiles at Site 1166. **A.** Calcium and magnesium. **B.** Strontium. **C.** Lithium. **D.** Manganese.

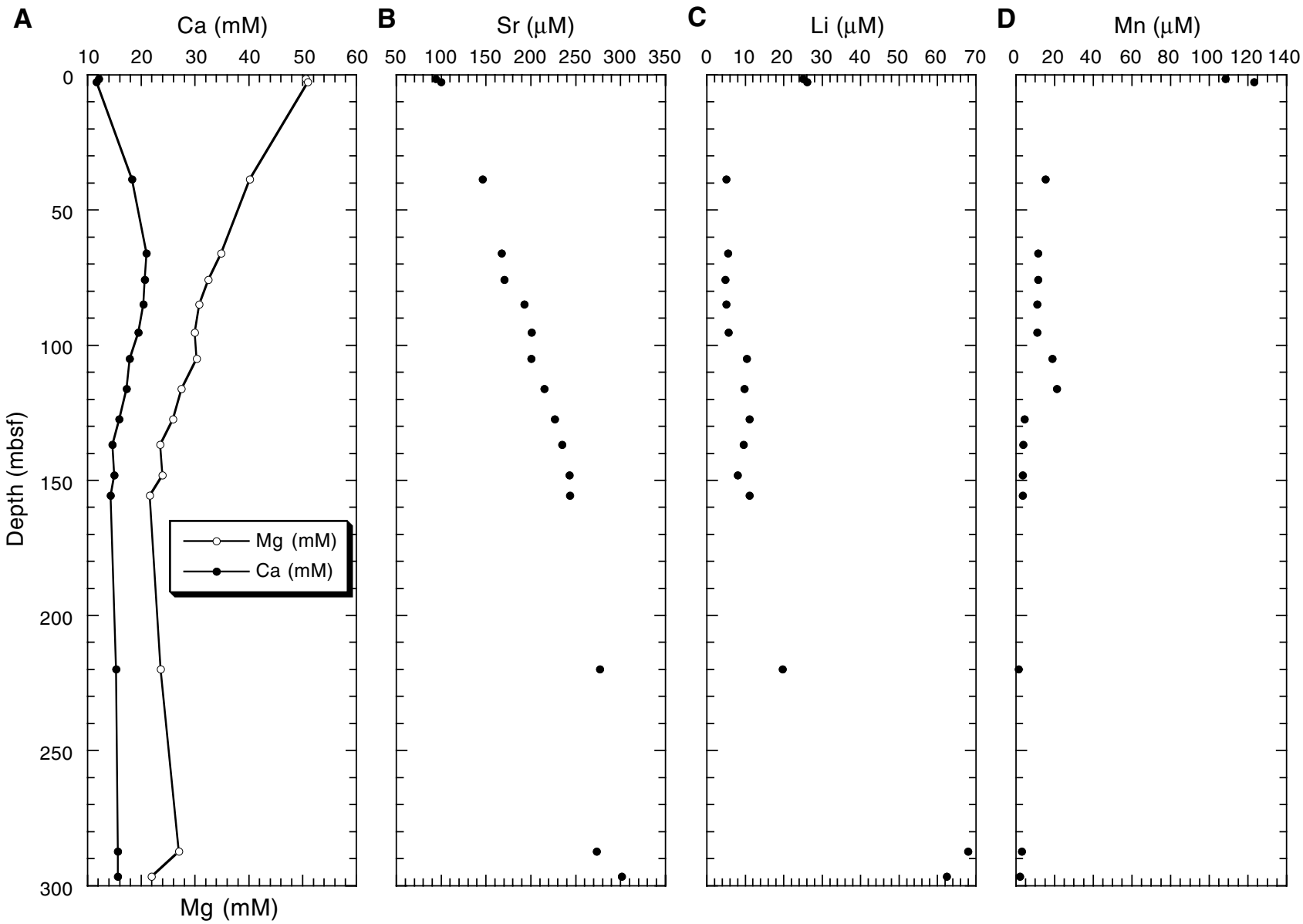

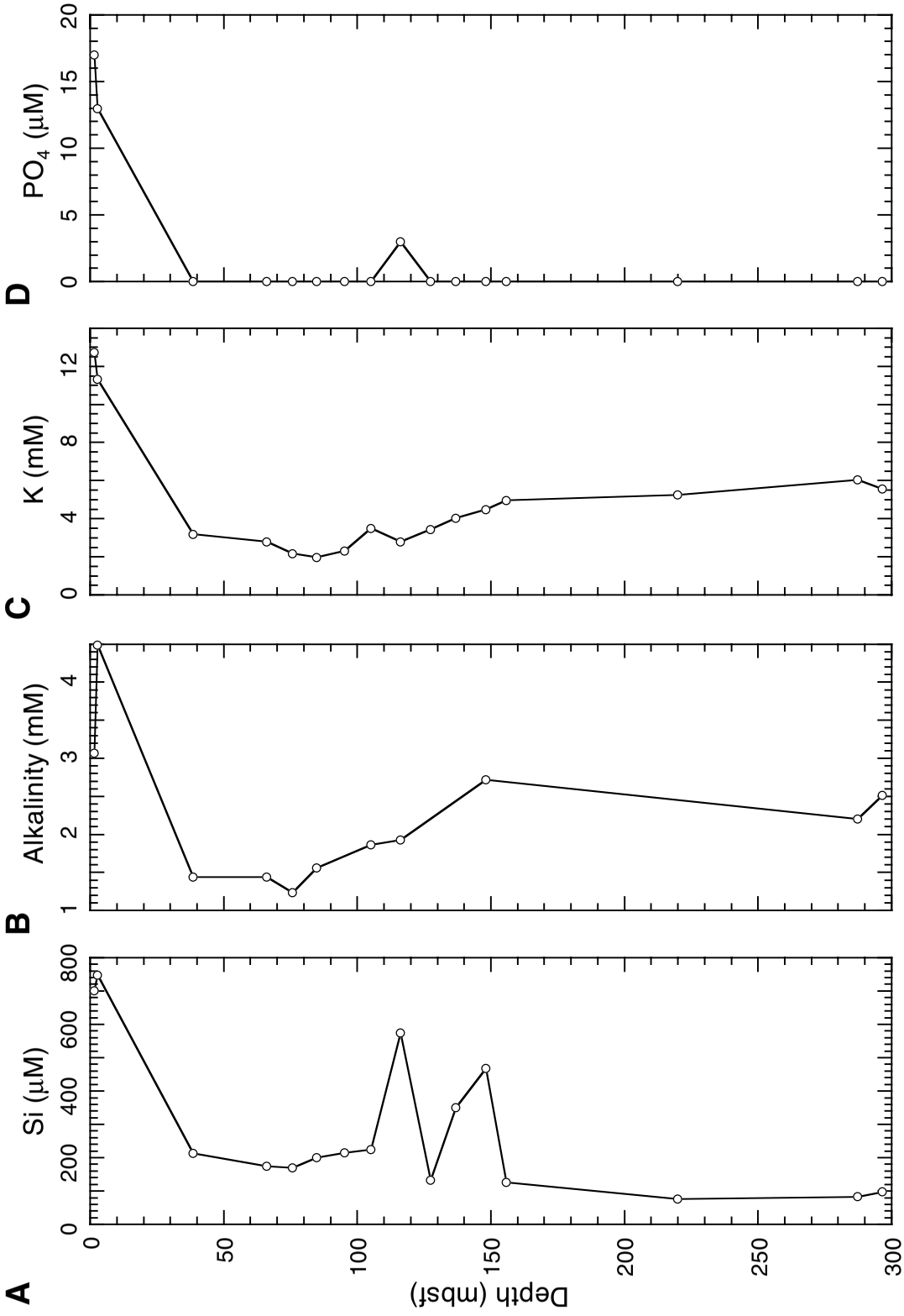

Figure F29. Downcore profiles of (**A**) silica, (**B**) alkalinity, (**C**) potassium, and (**D**) phosphate at Site 1166.

Figure F30. Downcore profiles of (**A**) sodium, (**B**) chloride, and (**C**) salinity at Site 1166.

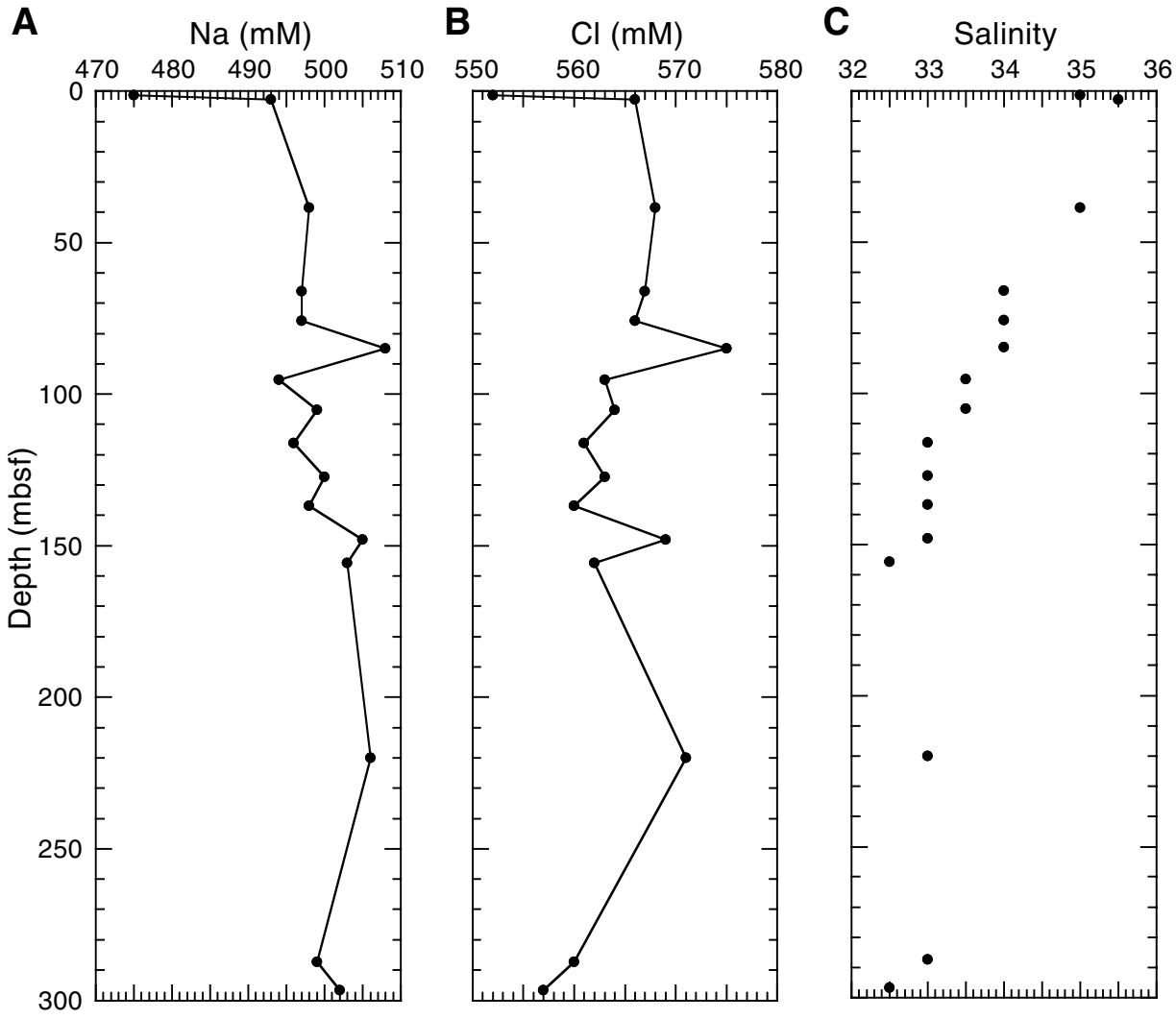

Figure F31. Weight percent carbon in sediments at Site 1166. **A.** Inorganic carbon (calcium carbonate). **B.** Organic carbon.

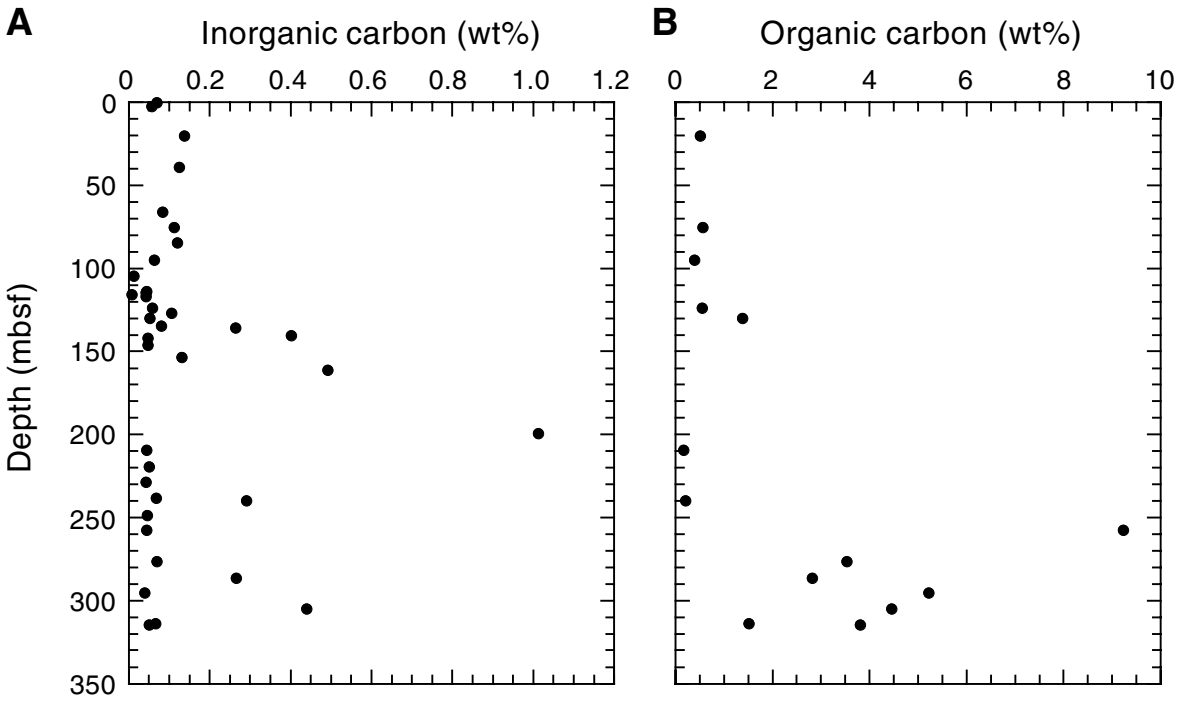

Figure F32. Plots showing bulk mineralogy from X-ray diffraction (XRD) and natural gamma radiation (NGR) vs. depth at Site 1166. Core recovery and lithostratigraphic units are shown on the left. The line through the NGR data is a 20-m moving average.

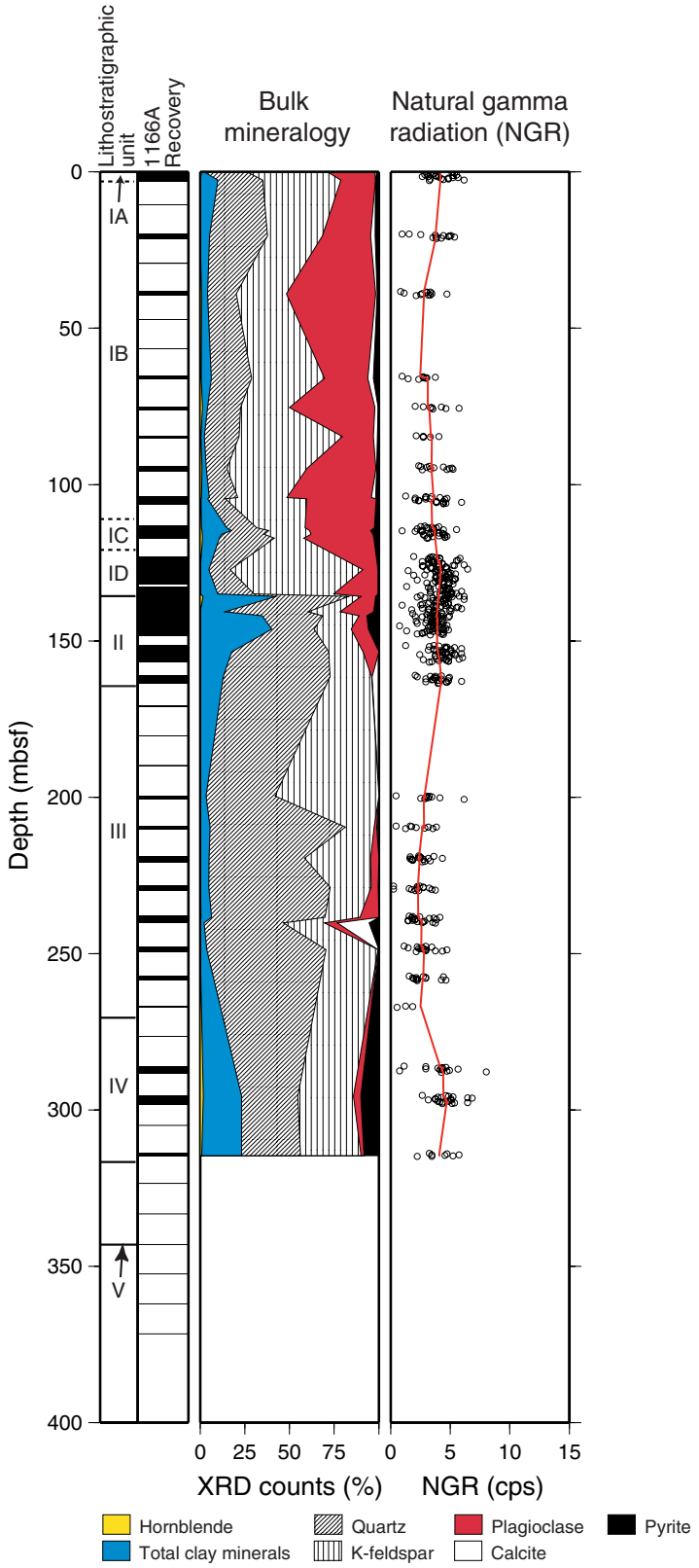

Figure F33. (**A**) Grain density and (**B**) porosity from discrete measurements. The columns on the right show lithostratigraphic units and core recovery.

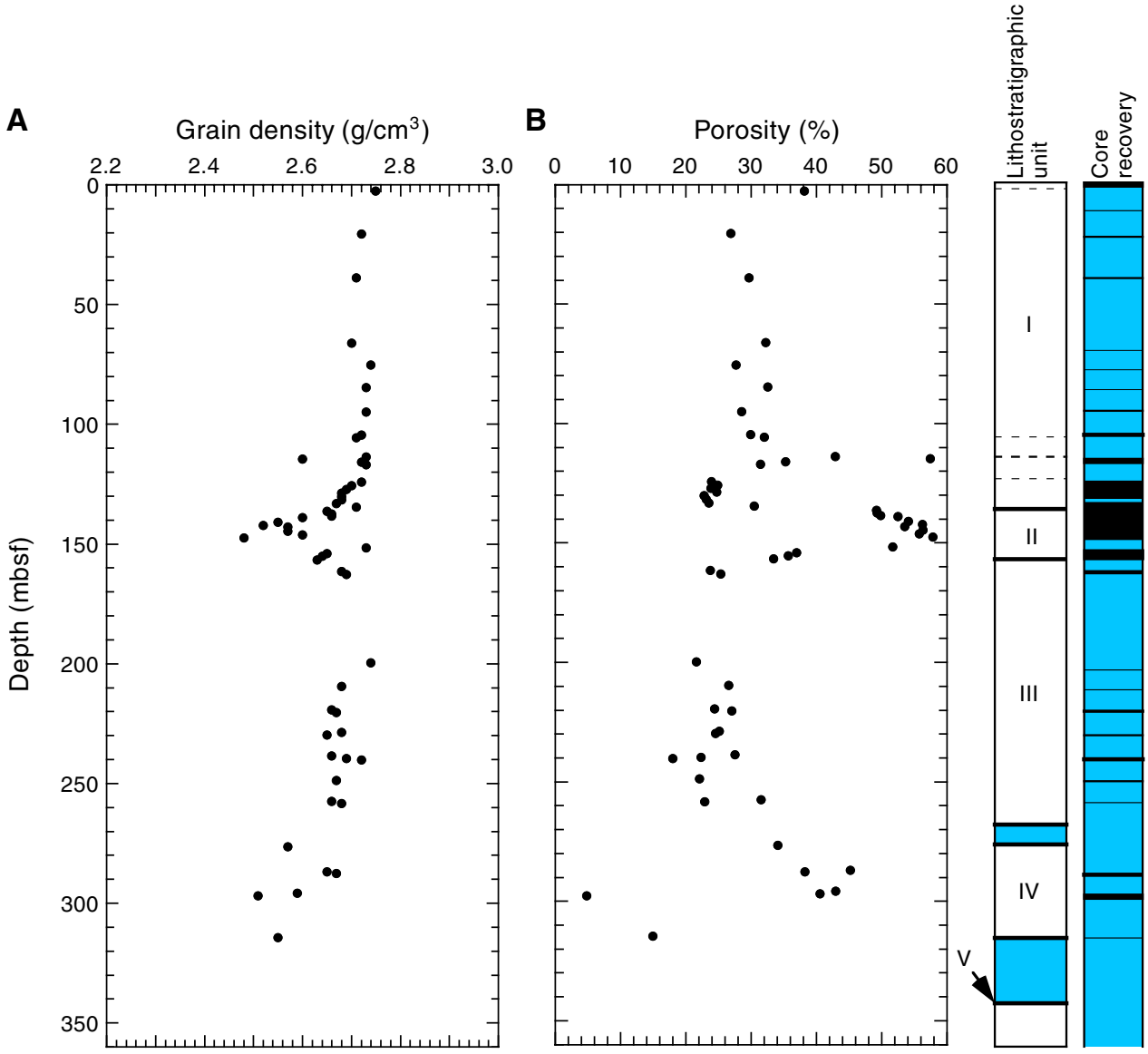

Figure F34. (A) Bulk density and (B) dry density from discrete measurements. The columns on the right show lithostratigraphic units and core recovery.

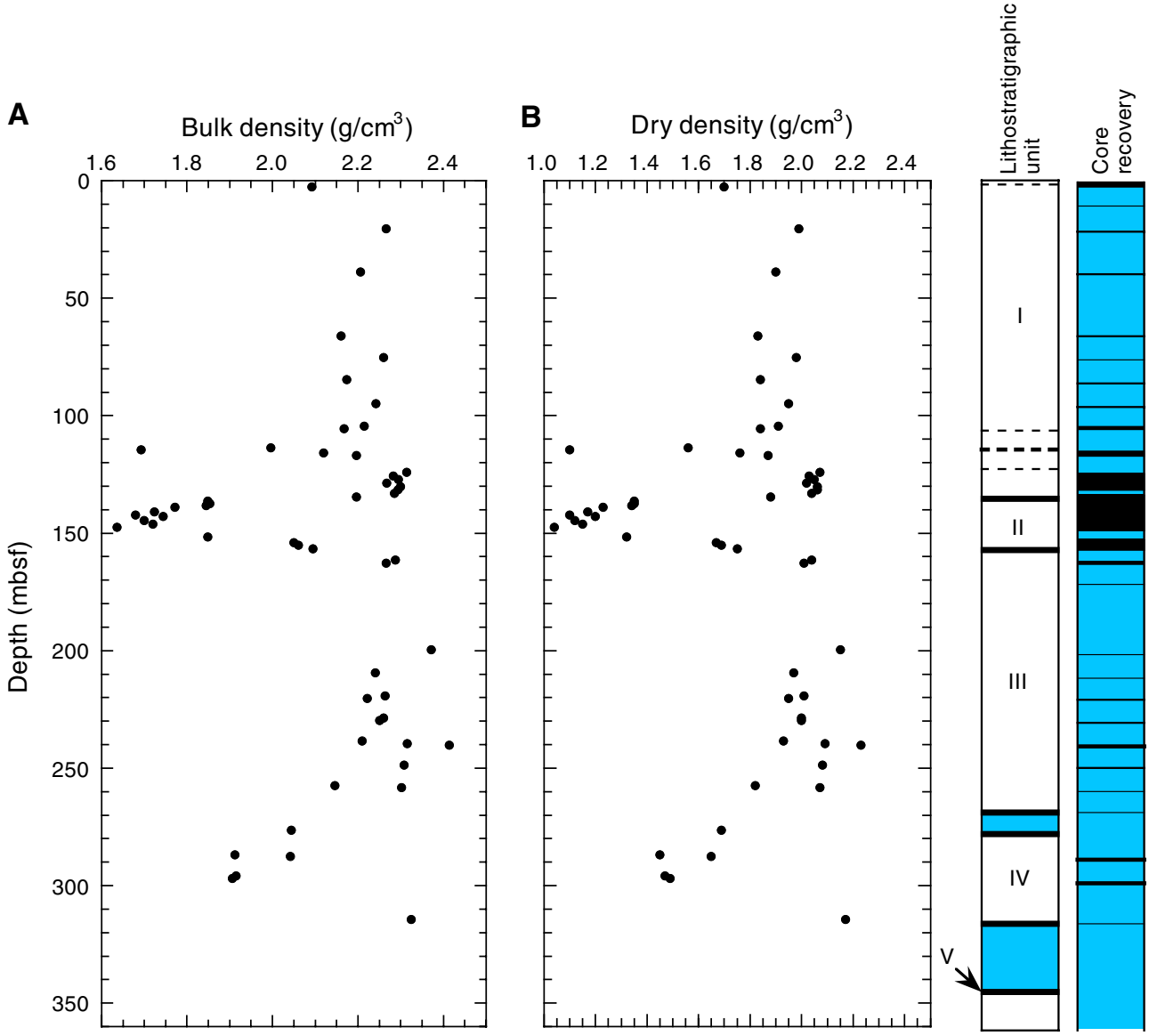

Figure F35. (A) Water content and (B) void ratio from discrete measurements. The columns on the right show lithostratigraphic units and core recovery.

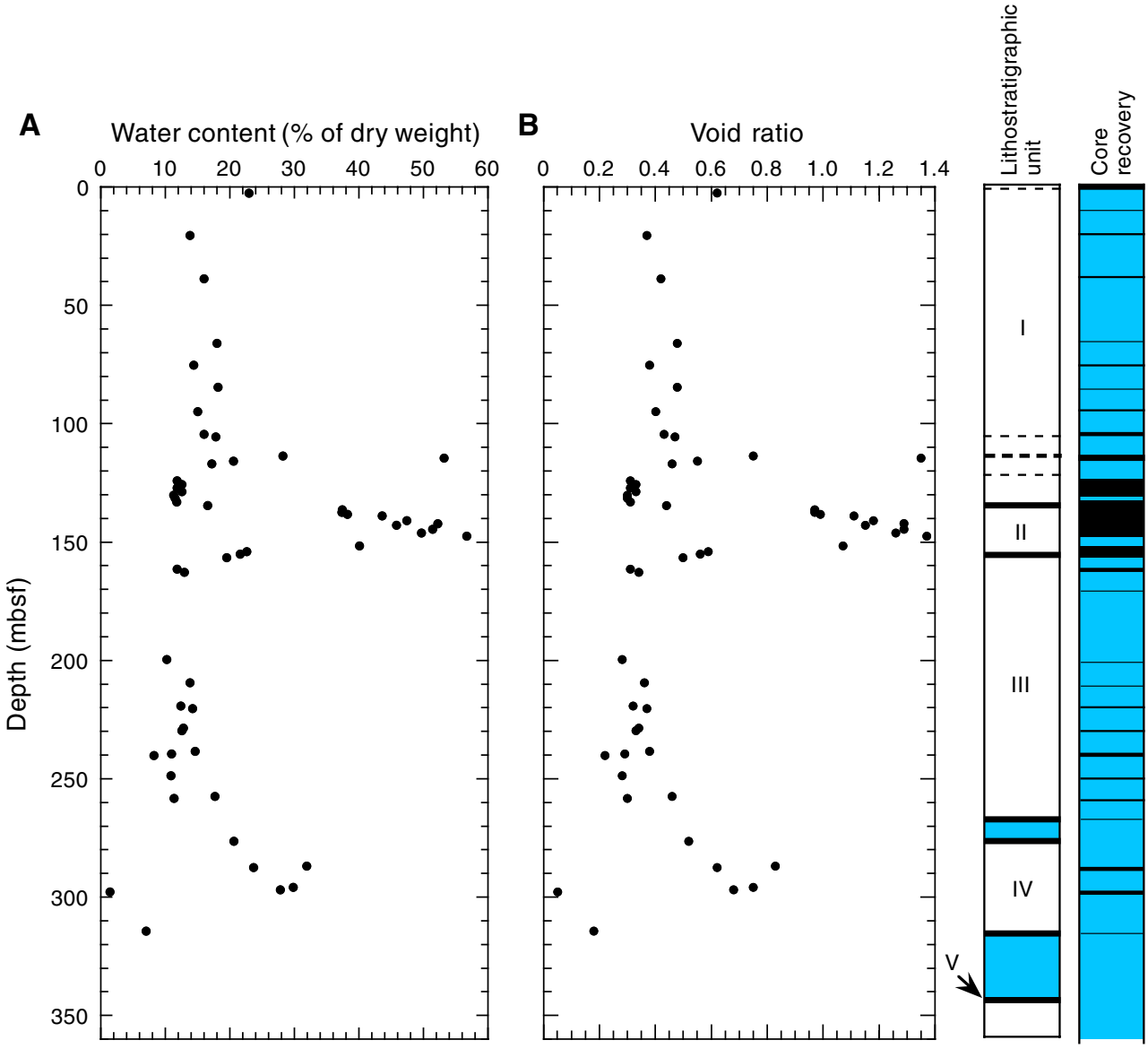

Figure F36. Discrete velocity measurements obtained with the PWS at Site 1166. The column on the right shows lithostratigraphic units.

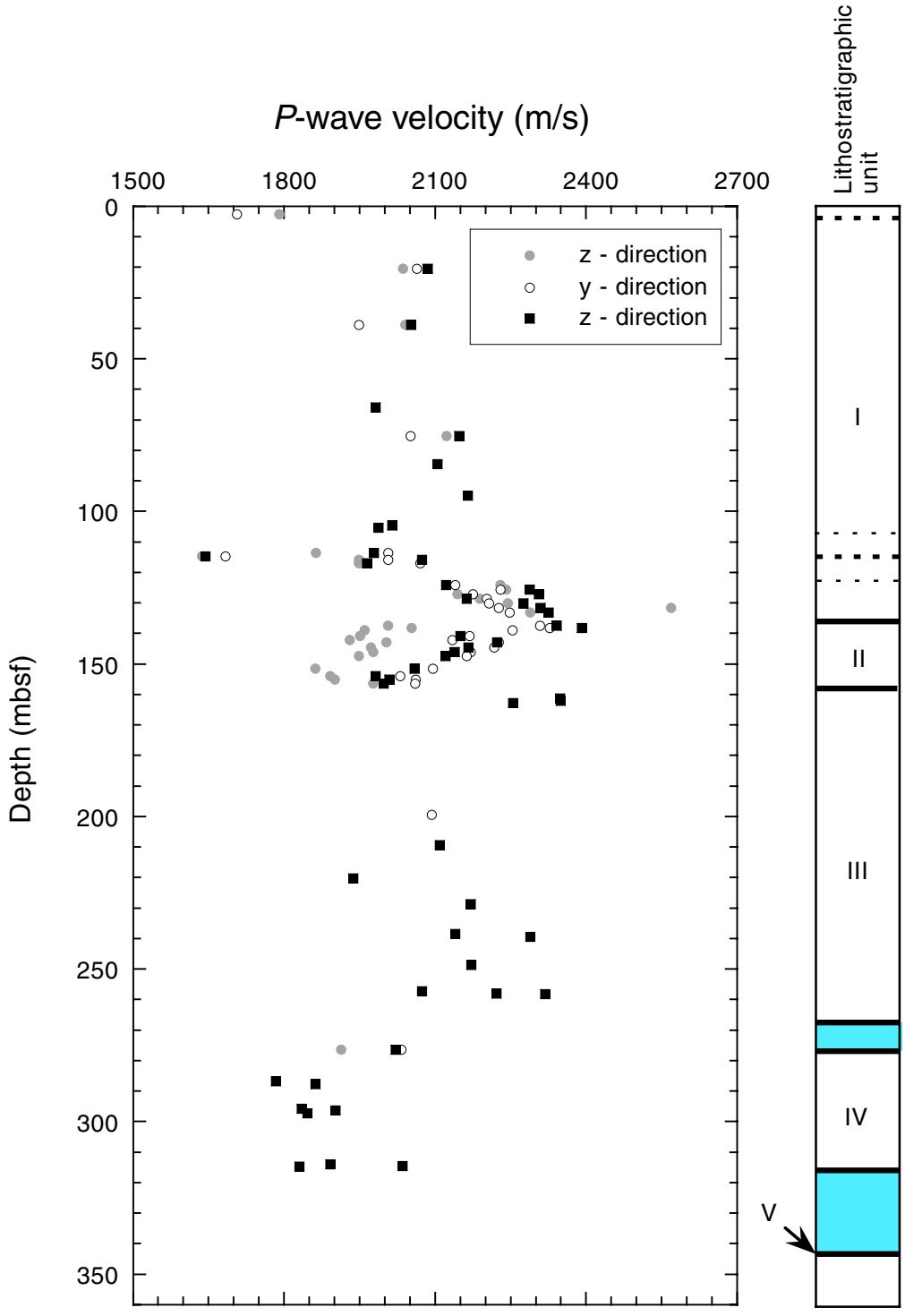

Figure F37. Measurements of undrained shear strength from Site 1166, using the fall cone (FC) and pocket penetrometer (PP). The column on the right shows lithostratigraphic units.

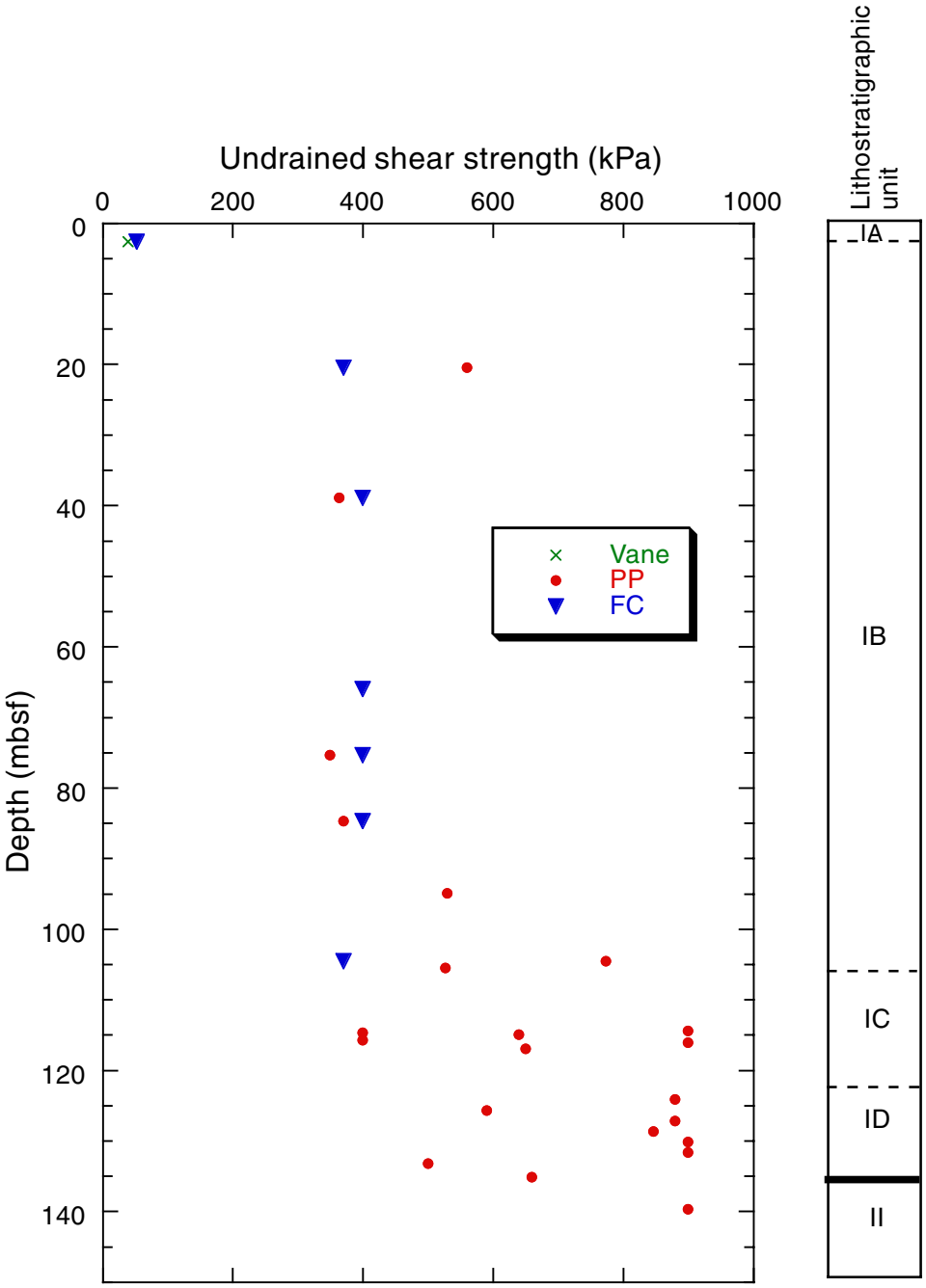

Figure F38. Normalization of undrained shear strength with respect to effective overburden pressure. The column on right shows lithostratigraphic units. PP = pocket penetrometer; FC = fall cone.

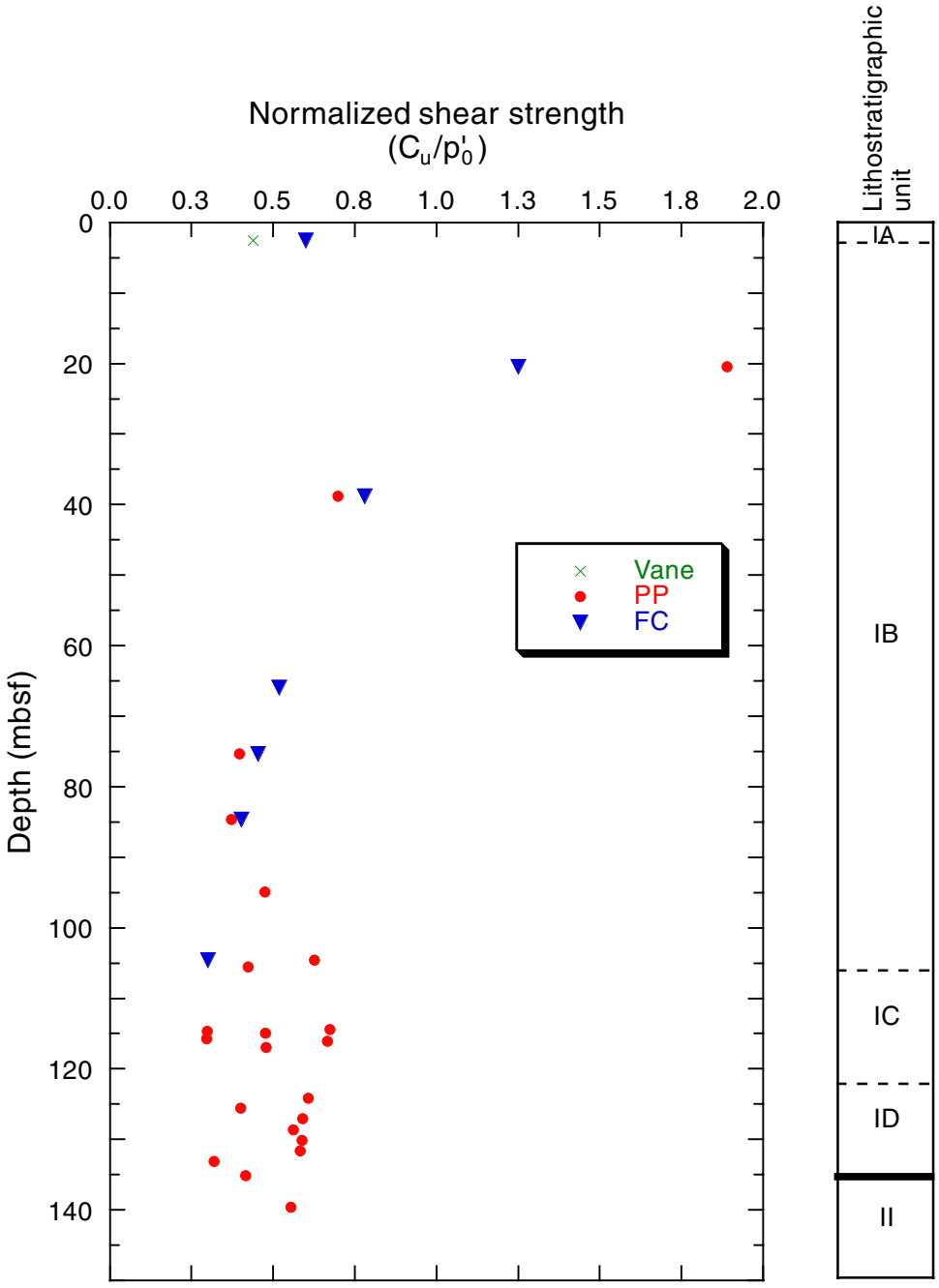

Figure F39. Thermal conductivity measurements and dry densities from Site 1166. There is a strong covariance between the two measured properties.

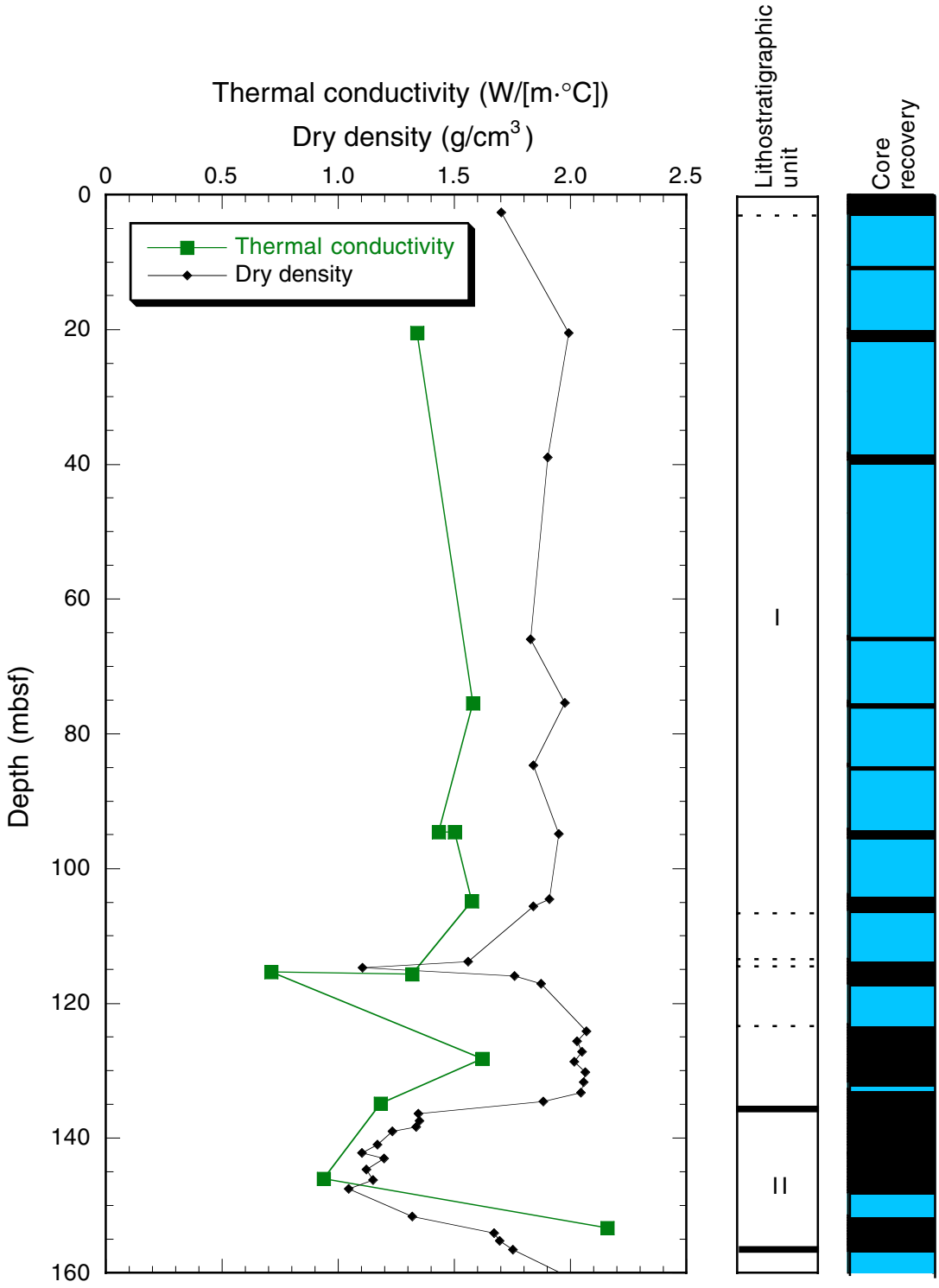

Figure F40. Logging summary diagram showing log, pipe, and seafloor depths. Although the driller's mudline was subsequently determined to be 480.0 mbrf (by video camera on reentry into the hole), all core depths in the volume are referenced to the initial mudline of 486.7 mbrf, except where stated.

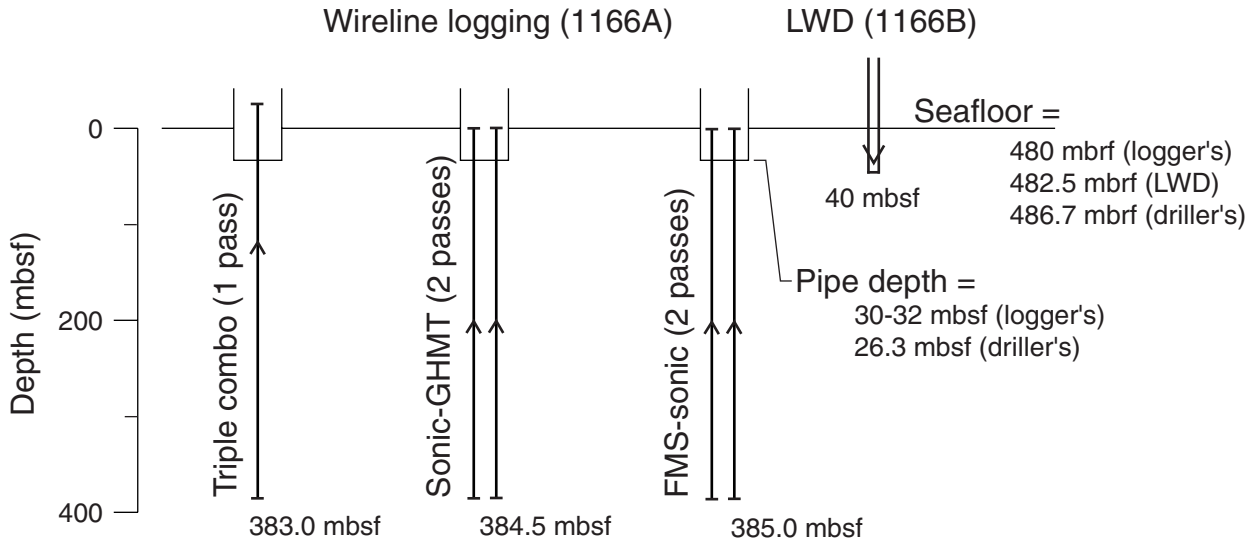

Figure F41. Density, porosity, resistivity, and sonic velocity logs, with the logging units marked. The core physical properties measurements of density and porosity and the lithostratigraphic column are also shown; they have been shifted downward by 6.7 m in order to compensate for the offset of the cores that resulted from nonrecovery of the mudline.

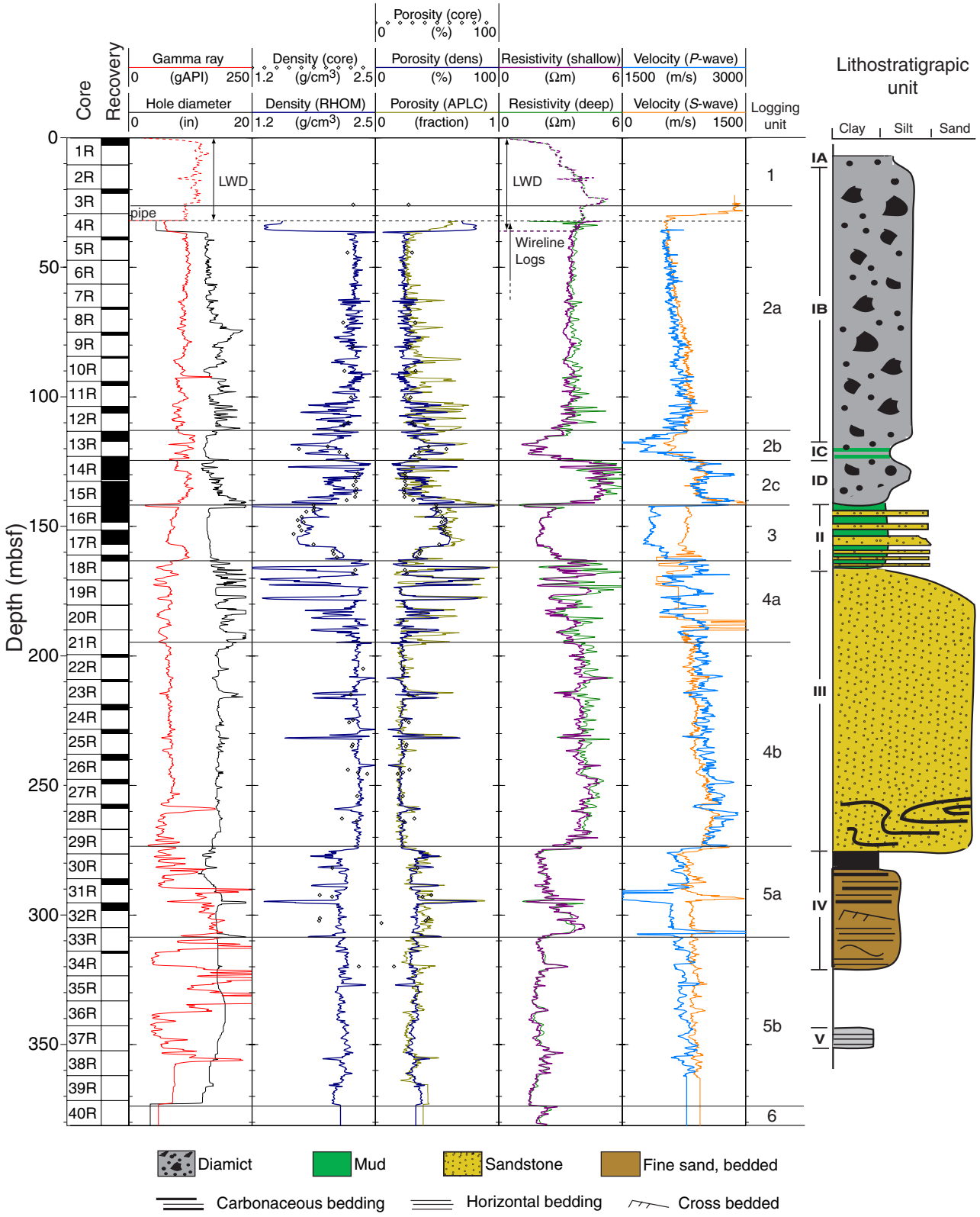

Figure F42. Total gamma-ray, potassium, thorium, uranium, photoelectric effect (PEF), and magnetic susceptibility logs. The lithostratigraphic column has been shifted down by 6.7 m to account for the offset between log and core depths.

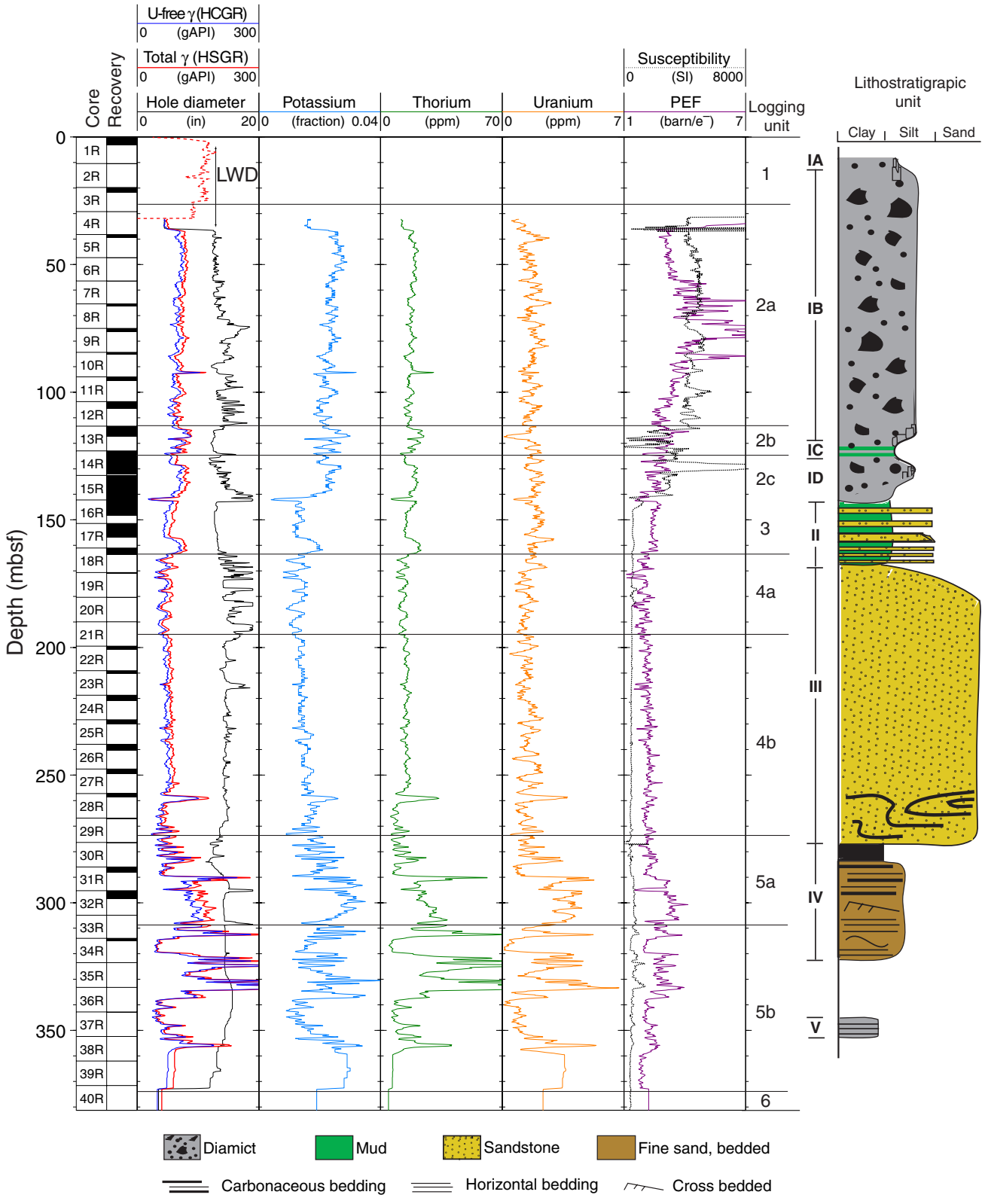

Figure F43. Representative examples of FMS images from Hole 1166A, with lithological descriptions. (Continued on next page.)

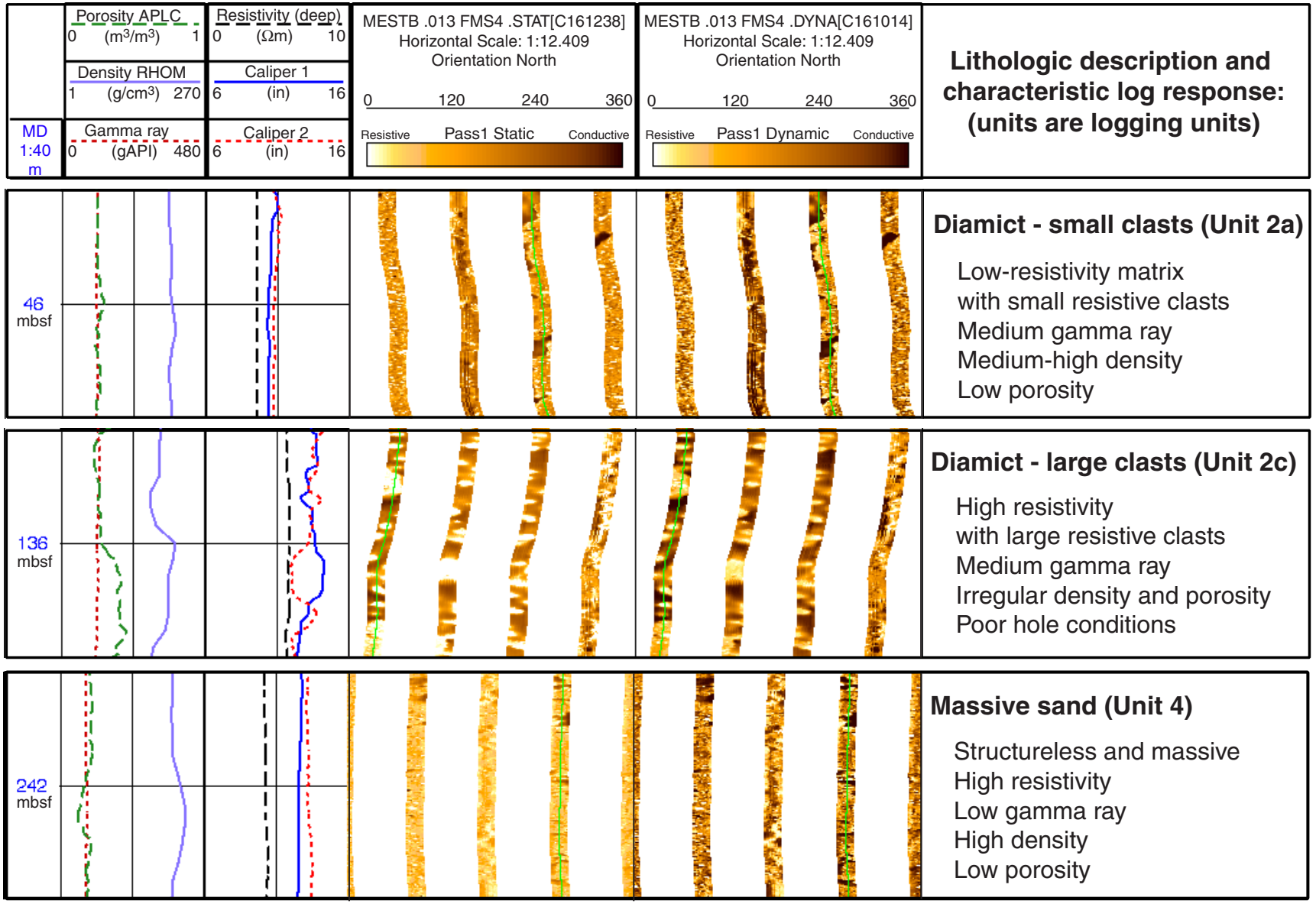

Figure F43 (continued).

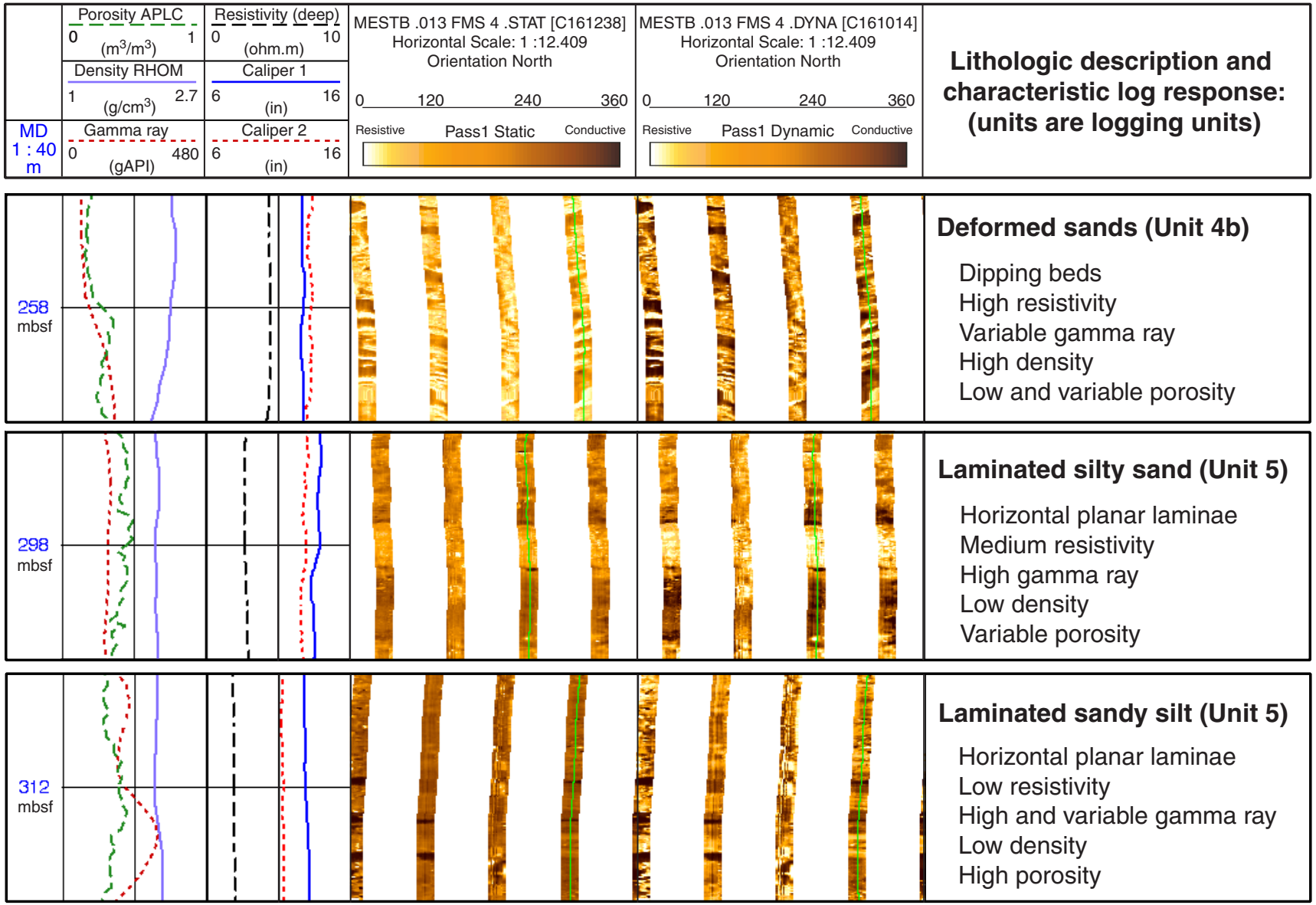

Figure F44. Detail of the *P*-wave velocity log in logging Units 3 and 4.

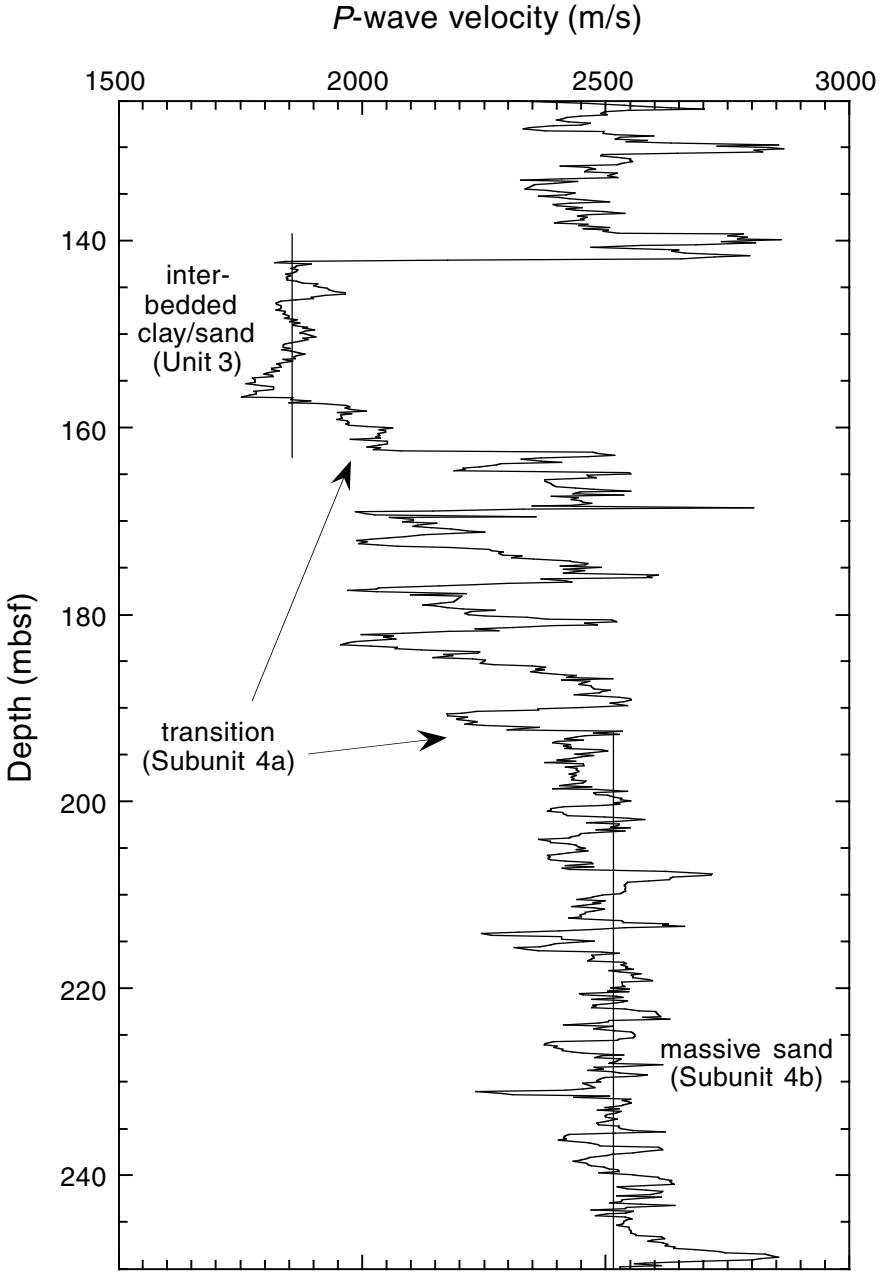

Figure F45. *P*-wave slowness log, source wavelet, and synthetic seismogram for Hole 1166A.

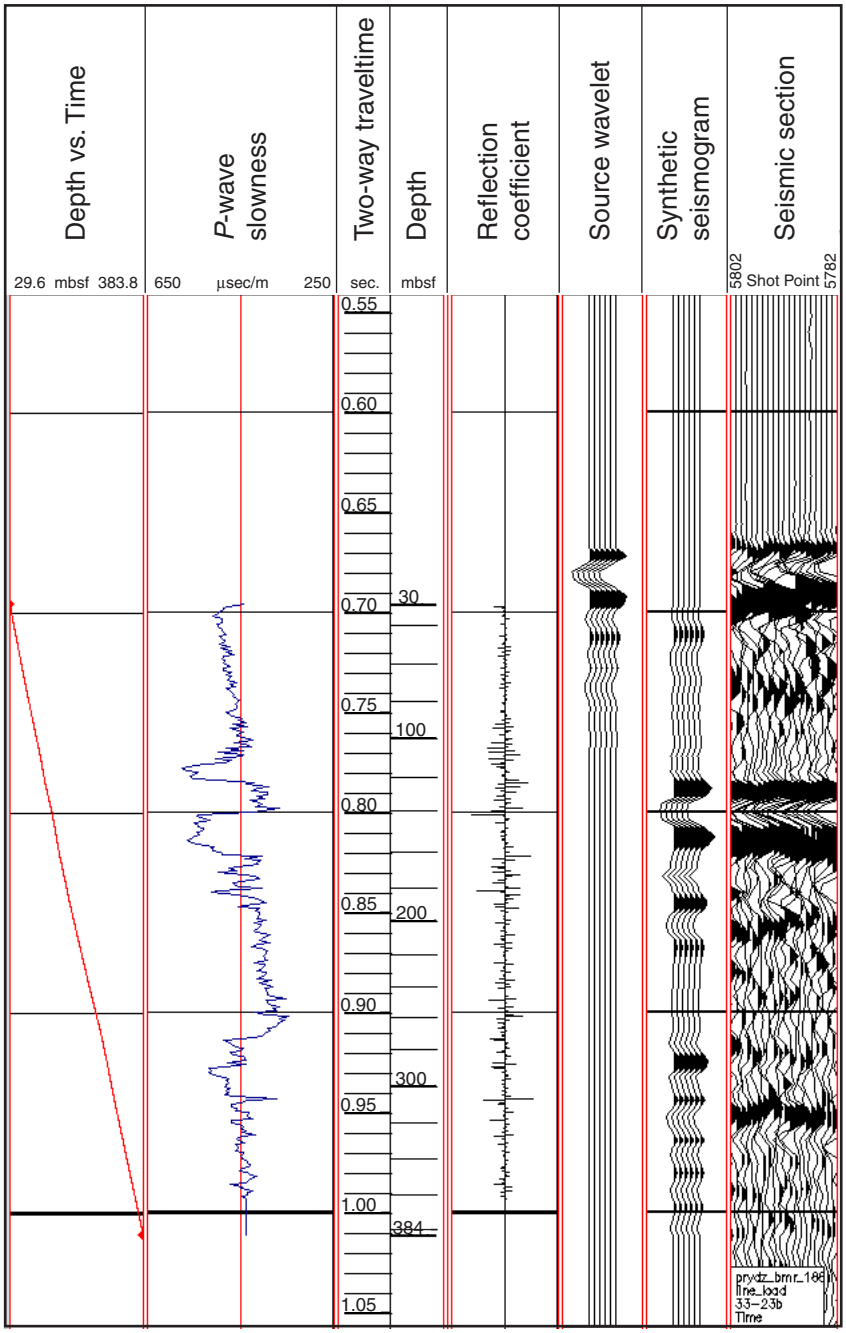

Figure F46. The synthetic seismogram (darker shading) and *P*-wave slowness log (lighter shading) overlaid on seismic line BMR33-23B. Note that the site is offset ~1 km south east of the seismic line.

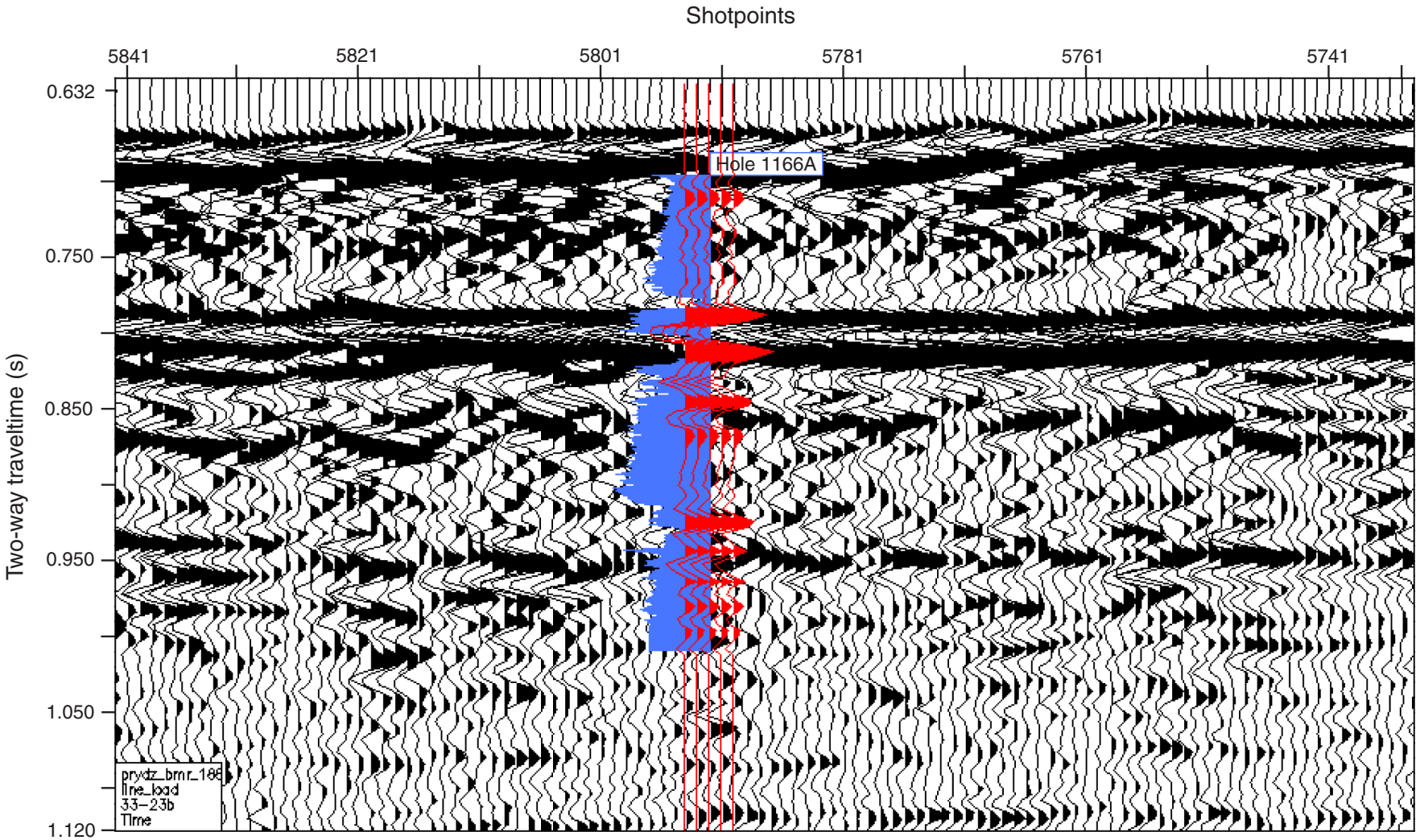

Figure F47. Correlation of resistivity and sonic velocity logs between Sites 1166 and 742 (Leg 119). Site 742 is ~30 km to the east of Site 1166.

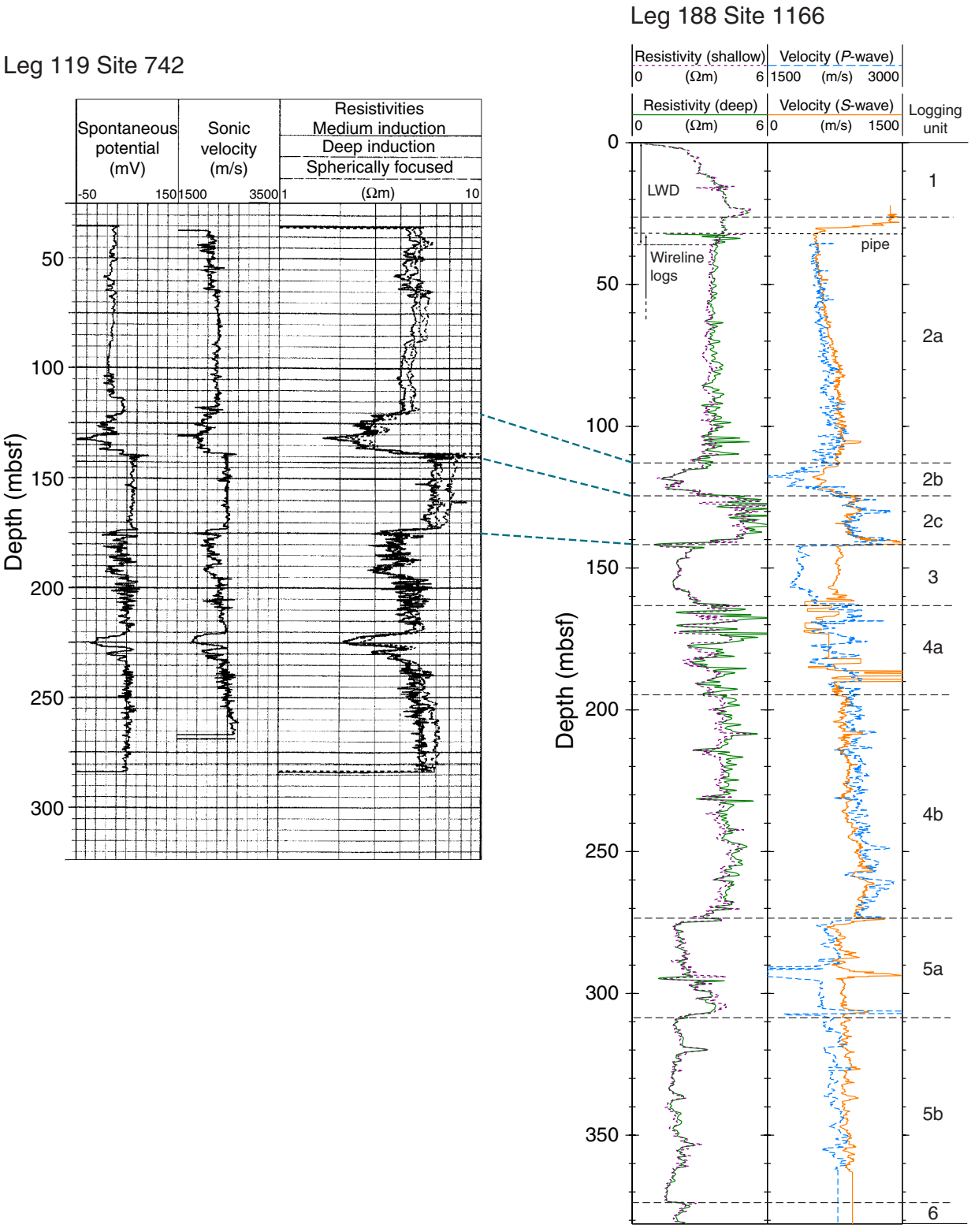

Figure F48. Processed GHMT logs. The remanent and induced (susceptibility) components of the total field measurement and a correlation analysis are plotted. Where the remanent and induced curves correlate, the polarity is normal; where they anticorrelate, the polarity is reversed. Ten interval thicknesses were used for this analysis. An interpretation of the correlation analysis is plotted along with the available core paleomagnetization. (**Figure shown on next page.**)

Figure F48 (continued). (Caption shown on previous page.)

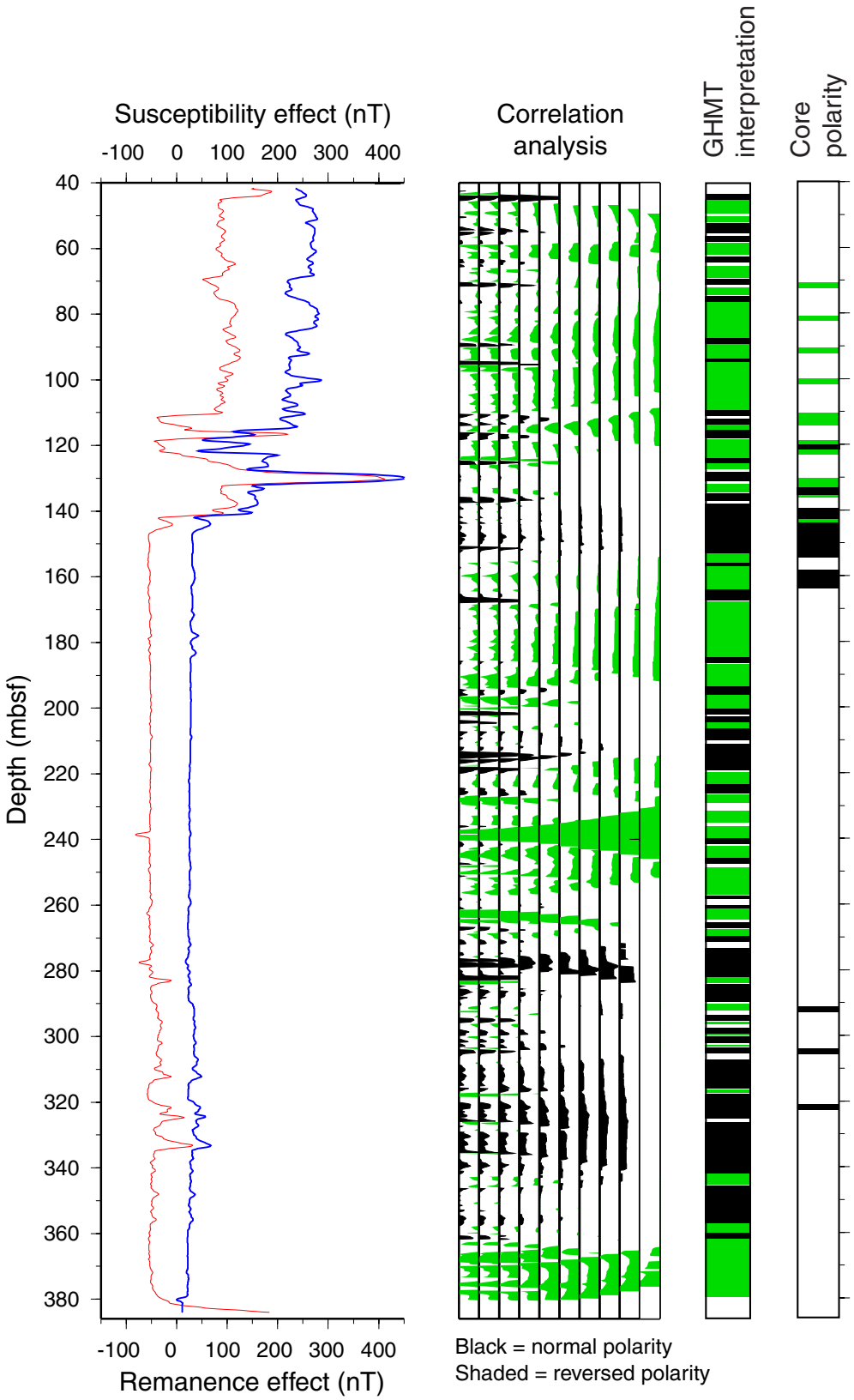

Figure F49. Temperature of the borehole fluid vs. depth.

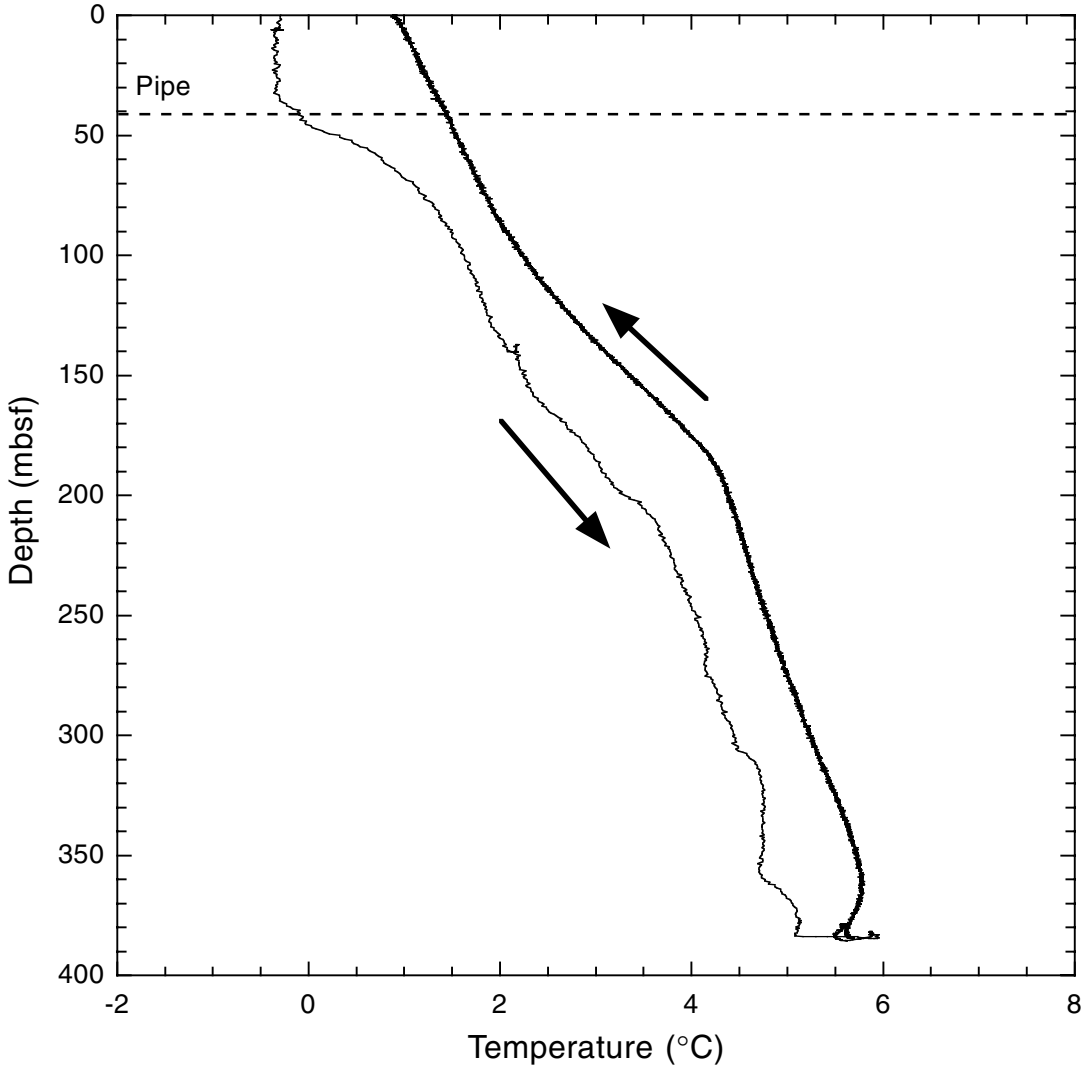

Table T1. Coring summary, Site 1166.

Core	Date (Feb 2000)	Ship local time	Depth (mbsf) Top	Depth (mbsf) Bottom	Length (m) Cored	Length (m) Recovered	Recovery (%)
188-1166A-							
1R	16	1015	0.0	10.4	10.4	2.97	29.7
2R	16	1340	10.4	19.8	9.4	0.25	2.7
3R	16	1635	19.8	29.2	9.4	1.79	19.0
4R	16	1945	29.2	38.2	9.0	0.07	0.8
5R	16	2210	38.2	47.3	9.1	1.40	15.4
6R	16	2350	47.3	56.4	9.1	0.10	1.1
7R	17	0140	56.4	65.4	9.0	0.10	1.1
8R	17	0320	65.4	75.0	9.6	0.90	9.4
9R	17	0445	75.0	84.4	9.4	1.20	12.8
10R	17	0605	84.4	94.0	9.6	0.78	8.1
11R	17	0745	94.0	103.7	9.7	1.75	18.0
12R	17	0920	103.7	113.3	9.6	2.72	28.3
13R	17	1045	113.3	123.0	9.7	4.05	41.8
14R	17	1240	123.0	132.6	9.6	8.93	93.0
15R	17	1425	132.6	142.2	9.6	9.90	103.1
16R	17	1540	142.2	151.4	9.2	6.16	67.0
17R	17	1710	151.4	161.0	9.6	5.59	58.2
18R	17	1815	161.0	170.6	9.6	2.60	27.1
19R	17	1915	170.6	180.3	9.7	0.38	3.9
20R	17	2020	180.3	189.9	9.6	0.10	1.0
21R	17	2125	189.9	199.5	9.6	0.01	0.1
22R	19	1255	199.5	209.1	9.6	1.17	12.2
23R	19	1350	209.1	218.7	9.6	1.08	11.3
24R	19	1445	218.7	228.3	9.6	2.15	22.4
25R	19	1535	228.3	237.9	9.6	1.75	18.2
26R	19	1625	237.9	247.6	9.7	2.46	25.4
27R	19	1740	247.6	257.2	9.6	1.82	19.0
28R	19	1835	257.2	266.8	9.6	1.52	15.8
29R	19	1920	266.8	276.4	9.6	0.38	4.0
30R	19	2015	276.4	286.0	9.6	0.20	2.1
31R	19	2120	286.0	295.3	9.3	2.26	24.3
32R	19	2320	295.3	304.9	9.6	3.03	31.6
33R	20	0040	304.9	313.9	9.0	0.05	0.6
34R	20	0150	313.9	323.5	9.6	1.06	11.0
35R	20	0300	323.5	333.2	9.7	0.00	0.0
36R	20	0410	333.2	342.8	9.6	0.00	0.0
37R	20	0530	342.8	352.4	9.6	0.20	2.1
38R	20	0640	352.4	362.0	9.6	0.00	0.0
39R	20	1115	362.0	371.6	9.6	0.03	0.3
40R	20	1300	371.6	381.3	9.7	0.00	0.0
				Totals:	381.3	71.21	18.7

Table T2. Expanded coring summary, Site 1166.

Core	Date (Feb 2000)	Ship local time	Core depth (mbsf) Top	Core depth (mbsf) Bottom	Length (m) Cored	Length (m) Recovered	Recovery (%)	Section	Length (m) Liner	Length (m) Curated	Section depth (mbsf) Top	Section depth (mbsf) Bottom	Catwalk samples	Comment
Position: 67.69618°S, 74.78693°E														
Water depth (mbrf; tagged): 486.7														
188-1166A-														
1R	16	1015	0.0	10.4	10.4	3.10	29.7							
								1	1.50	1.50	0.00	1.50	IW	
								2	1.29	1.29	1.50	2.79	IW, HS, PAL	
								CC (w/CC)	0.28	0.28	2.79	3.07	PAL	
									3.07	3.07				
2R	16	1340	10.4	19.8	9.4	0.30	2.7							
								CC (w/CC)	0.25	0.30	10.40	10.70	PAL	
									0.25	0.30				
3R	16	1635	19.8	29.2	9.4	1.80	19.0							
								1	1.50	1.50	19.80	21.30	CARL	
								2	0.29	0.29	21.30	21.59	PAL, HS	
									1.79	1.79				
4R	16	1945	29.2	38.2	9.0	0.10	0.8							
								1	0.07	0.11	29.20	29.31	PAL	
									0.07	0.11				
5R	16	2210	38.2	47.3	9.1	1.40	15.4							
								1	1.35	1.35	38.20	39.55	HS, IW	
								CC (NS)	0.05	0.05	39.55	39.60	PAL	All to PAL
									1.40	1.40				
6R	16	2350	47.3	56.4	9.1	0.10	1.1							
								CC (w/CC)	0.10	0.11	47.30	47.41	PAL	
									0.10	0.11				
7R	17	0140	56.4	65.4	9.0	0.10	1.1							
								CC (w/CC)	0.10	0.13	56.40	56.53	PAL	Other
									0.10	0.13				
8R	17	0320	65.4	75.0	9.6	0.90	9.4							
								1	0.90	0.93	65.40	66.33	PAL, HS, IW	
									0.90	0.93				
9R	17	0445	75.0	84.4	9.4	1.20	12.8							
								1	1.02	1.02	75.00	76.02	HS, IW	
								CC (w/1)	0.18	0.18	76.02	76.20	PAL	
									1.20	1.20				

Notes: CC = core catcher (number in parentheses indicates which section the core catcher is stored with). NS = all of the core catcher was used for paleontology sample, IW = interstitial water, HS = headspace, PAL = paleontology sample, CARL = whole-round sample for geotechnical experiments. Only a portion of the table appears here. The complete table is available in **ASCII format.**

Table T3. Summary of diatom and radiolarian biostratigraphic datums recognized and calibrated ages for each datum event, Hole 1166A.

Upper sample		Lower sample					
Core, section, interval (cm)	Interval depth (mbsf)	Core, section, interval (cm)	Interval depth (mbsf)	Event	Taxon	Constraint	Calibrated age (Ma)
Diatoms:							
188-1166A-		188-1166A-					
1R-CC	3.02	13R-1, 70-71	**114.00**	LO	*Actinocyclus ingens*	<	0.66
1R-CC	3.02	13R-1, 70-71	**114.00**	LO	*Thalassiosira kolbei*	>	1.8-2.0
13R-1, 80-83	114.10	13R-1, 124-126	**114.54**	LO	*Thalassiosira vulnifica*	>	2.2-2.3
13R-2, 65-67	**115.45**	13R-CC	117.25	FO	*Thalassiosira vulnifica*	<	2.8-3.2
13R-CC	**117.25**	14R-CC	131.88	FO	*Thalassiosira elliptipora*	<	3.2
13R-CC	117.25	15R-3, 18-19	**135.73**	LO	*Hemiaulus caracteristicus*	>	~33
17R-2, 58-59	**153.48**	—	—	LO (absence)	middle Eocene taxa	<	~37
Radiolarians:							
188-1166A-		188-1166A-					
—	0.00	1R-2, 72-73	**2.22**	LO	*Pterocanium c. trilobum*	<	0.83
—	0.00	1R-2, 72-73	**2.22**	LO	*Cycladophora pliocenica*	<	~1.35
1R-2, 72-73	**2.22**	13R-1, 150-151	114.77	FO	*Lithelium nautiloides*	>	1.93
1R-2, 72-73	**2.22**	13R-1, 150-151	114.77	FO	*Triceraspyris antarctica*	>	1.93
1R-2, 72-73	2.22	13R-1, 150-151	**14.77**	LO	*Antarctissa strelkovi*	<	~2.4
13R-2, 5-6	**114.83**	—	—	FO	*Antarctissa strelkovi*	>	~6.1

Notes: Sample designations and depths in bold type represent the occurrence of each taxon, and plain type represents sample-spacing uncertainty for each datum. LO = last occurrence, FO = first occurrence. — = upper or lower interval not recognized because of poor preservation or absence.

Table T4. Interstitial water chemistry from shipboard measurements, Site 1166.

Core, section	Depth (mbsf)	Salinity	pH	Alkalinity (mM)	Cl (mM)	SO_4 (mM)	NH_4 (μM)	PO_4 (μM)	H_4SiO_4 (μM)	Ca (mM)	Mg (mM)	Sr (μM)	K (mM)	Na (mM)	Li (μM)	Mn (mM)
188-1166A-																
1R-1	1.45	35.0	7.88	3.07	552.0	28.8	117.0	17.0	702.0	12.1	50.6	94.1	12.7	475.0	25.1	108.5
1R-2	2.74	35.5	7.86	4.49	566.0	29.5	153.0	13.0	748.0	11.8	51.1	100.5	11.3	493.0	26.1	123.1
5R-1	38.64	35.0	8.09	1.44	568.0	24.4	83.0	0.0	213.0	18.3	40.2	146.2	3.2	498.0	5.1	15.4
8R-1	66.07	34.0	8.28	1.44	567.0	21.4	93.0	0.0	174.0	21.0	34.9	167.5	2.8	497.0	5.6	11.7
9R-1	75.87	34.0	8.37	1.23	566.0	19.3	75.0	0.0	170.0	20.7	32.5	170.6	2.2	497.0	4.9	11.6
10R-1	84.88	34.0	8.36	1.56	575.0	18.0	215.0	0.0	201.0	20.4	30.8	193.1	2.0	508.0	5.1	11.2
11R-1	95.34	33.5			563.0	16.4	256.0	0.0	215.0	19.5	30.0	200.8	2.3	494.0	5.7	11.1
12R-1	105.10	33.5	8.20	1.86	564.0	16.3	391.0	0.0	224.0	17.9	30.3	200.6	3.5	499.0	10.4	18.9
13R-2	116.20	33.0	8.01	1.92	561.0	12.6	493.0	3.0	574.0	17.3	27.5	215.5	2.8	496.0	9.8	21.1
14R-3	127.40	33.0			563.0	12.3	578.0	0.0	133.0	16.0	25.9	226.9	3.4	500.0	11.1	4.5
15R-3	136.95	33.0			560.0	9.0	835.0	0.0	350.0	14.7	23.5	235.2	4.0	498.0	9.6	3.9
16R-4	148.11	33.0	8.18	2.72	569.0	8.2	696.0	0.0	468.0	15.0	24.0	243.1	4.5	505.0	8.0	3.6
17R-4	155.80	32.5			562.0	8.7	785.0	0.0	126.0	14.3	21.6	243.7	5.0	503.0	11.1	3.6
24R-1	220.05	33.0			571.0	9.0	962.0	0.0	77.0.	15.3	23.6	277.0	5.3	506.0	19.7	1.5
31R-1	287.40	33.0	7.50	2.20	560.0	14.2	1104.0	0.0	83.0	15.7	27.1	273.5	6.0	499.0	68.0	3.2
32R-1	296.70	32.5	7.68	2.52	557.0	11.6	1277.0	0.0	97.0	15.6	22.0	301.3	5.6	502.0	62.4	2.3

Table T5. Carbon, nitrogen, and sulfur analyses of sediments, Site 1166.

Core, section, interval (cm)	Depth (mbsf)	IC (wt%)	$CaCO_3$ (wt%)	TC (wt%)	OC (wt%)	TN (wt%)	TS (wt%)	C/N
188-1166A-								
1R-1, 23-24	0.23	0.07	0.57					
1R-2, 115-116	2.65	0.06	0.48					
3R-1, 69-70	20.49	0.14	1.15	0.58	0.511	0.01	0	58.00
5R-1, 77-78	38.97	0.13	1.04					
8R-1, 62-63	66.02	0.08	0.70					
9R-1, 38-39	75.38	0.11	0.94	0.68	0.567	0.03	0	22.67
10R-1, 23-24	84.63	0.12	1.00					
11R-1, 90-91	94.90	0.06	0.53	0.45	0.387	0.01	0	45.00
12R-1, 88-90	104.58	0.01	0.10					
13R-1, 49-50	113.79	0.04	0.37					
13R-1, 143-145	114.73	0.04	0.35					
13R-2, 116-11	115.96	0.01	0.07					
13R-3, 83-84	117.13	0.04	0.35					
14R-1, 120-121	124.20	0.06	0.49	0.62	0.561	0.03	0	20.67
14R-3, 120-121	127.20	0.11	0.89					
14R-5, 120-121	130.20	0.05	0.44	1.44	1.387	0.04	0	36.00
15R-2,88-89	134.93	0.08	0.67					
15R-3, 24-25	135.79	0.26	2.20					
15R-6, 58-59	140.63	0.40	3.34					
15R-7, 44-45	141.99	0.05	0.40					
16R-3, 102-107	146.22	0.05	0.40					
17R-2, 59-60	153.49	0.13	1.10					
18R-1, 46-47	161.46	0.49	4.10					
22R-1, 12-13	199.62	1.01	8.44					
23R-1, 45-46	209.55	0.04	0.37	0.21	0.166	0.02	0	10.50
24R-1, 74-75	219.44	0.05	0.43					
25R-1, 53-54	228.83	0.04	0.35					
26R-1, 53-54	238.43	0.07	0.57					
26R-2, 80-82	240.20	0.29	2.42	0.50	0.209	0.03	0.56	16.67
27R-1, 115-116	248.75	0.05	0.38					
28R-1, 39-40	257.59	0.04	0.37	9.27	9.225	0.10	0.55	92.70
30R-1, 7-8	276.47	0.07	0.57	3.61	3.541	0.25	0.09	14.44
31R-1, 47-48	286.47	0.27	2.22	3.09	2.824	0.24	0.21	12.88
32R-1, 26-27	295.56	0.04	0.33	5.26	5.220	0.20	1.23	26.30
33R-CC, 0-5	304.90	0.44	3.66	4.90	4.460	0.09	5.90	54.44
34R-1, 0-5	313.90	0.07	0.55	1.59	1.525	0.06	0.09	26.50
34R-1, 68-69	314.58	0.05	0.43	3.87	3.820	0.27	1.31	14.33

Note: IC = inorganic carbon, $CaCO_3$ = calcium carbonate, TC = total carbon, OC = organic carbon, TN = total nitrogen, TS = total sulfur.

Table T6. Organic carbon and Rock-Eval pyrolysis on selected samples, Site 1166.

Core, section, interval (cm)	Depth (mbsf)	OC (wt%)	S_1 (mg/g)	S_2 (mg/g)	S_3 (mg/g)	HI (mg/g C)	OI (mg/g C)	T_{max} (°C)
188-1166A-								
9R-1, 38-39	75.40	0.57	0.05	0.13	1.20	23	211	462
14R-1, 120-121	124.20	0.56	0.08	0.13	0.00	23	0	477
14R-5, 120-121	130.20	1.39	0.15	0.67	0.00	48	0	438
28R-1, 39-40	257.60	9.23	0.19	4.30	2.15	47	23	420
30R-1, 7-8	276.50	3.54	0.10	0.94	2.74	27	77	425
31R-1, 47-48	286.50	2.82	0.11	0.87	2.09	31	74	425
32R-1, 115-117	295.60	5.22	0.13	1.06	2.42	20	46	423
33R-CC, 0-5	304.90	4.46	0.13	1.46	3.17	33	71	420
34R-1, 0-5	313.90	1.52	0.11	0.25	0.00	16	0	475
34R-1, 68-69	314.60	3.82	0.15	1.53	0.62	40	16	420

Note: For explanation of column headings, see **"Organic Matter Characterization,"** p. 21, in "Organic Geochemistry" in the "Explanatory Notes" chapter.

Table T7. Discrete *P*-wave measurements, Site 1166.

Core, section, interval (cm)	Depth (mbsf)	Direction	Velocity (m/s)	Core temperature (°C)	Method
188-1166A-					
1R-2, 113.1	2.63	z	1790	25.9	PWS1
1R-2, 112.5	2.62	y	1706	25.6	PWS2
3R-1, 70.0	20.50	y	2064	25.1	PWS3
3R-1, 70.0	20.50	z	2037	25.1	PWS3
3R-1, 70.0	20.50	x	2086	25.0	PWS3
5R-1, 77.0	38.97	y	1949	25.2	PWS3
5R-1, 77.0	38.97	x	2052	25.2	PWS3
5R-1, 77.0	38.97	z	2041	25.3	PWS3
8R-1, 61.2	66.01	x	1982	22.4	PWS3
9R-1, 43.0	75.43	z	2123	23.6	PWS3
9R-1, 43.0	75.43	x	2148	23.6	PWS3
9R-1, 43.0	75.43	y	2051	23.6	PWS3
10R-1, 29.1	84.69	x	2105	23.6	PWS3
11R-1, 99.5	95.00	x	2165	22.1	PWS3
12R-1, 93.4	104.63	x	2015	22.1	PWS3
12R-2, 36.0	105.56	x	1987	24.2	PWS3
13R-1, 50.0	113.80	y	2007	25.3	PWS3
13R-1, 50.0	113.80	z	1864	25.4	PWS3
13R-1, 50.0	113.80	x	1979	25.5	PWS3
13R-1, 143.0	114.73	y	1683	25.5	PWS3
13R-1, 143.0	114.73	z	1637	25.5	PWS3
13R-1, 143.0	114.73	x	1644	25.5	PWS3
13R-2, 116.0	115.96	y	2007	25.4	PWS3
13R-2, 116.0	115.96	z	1949	25.4	PWS3
13R-2, 116.0	115.96	x	2074	25.3	PWS3
13R-3, 80.0	117.10	y	2070	25.4	PWS3
13R-3, 80.0	117.10	z	1949	25.4	PWS3
13R-3, 80.0	117.10	x	1965	25.4	PWS3
14R-1, 120.0	124.20	y	2140	24.9	PWS3
14R-1, 120.0	124.20	z	2230	24.9	PWS3
14R-1, 120.0	124.20	x	2122	25.0	PWS3
14R-2, 120.0	125.70	y	2230	25.0	PWS3
14R-2, 120.0	125.70	z	2242	25.0	PWS3
14R-2, 120.0	125.70	x	2288	25.0	PWS3
14R-3, 120.0	127.20	y	2175	25.1	PWS3
14R-3, 120.0	127.20	z	2145	25.2	PWS3
14R-3, 120.0	127.20	x	2306	25.2	PWS3
14R-4, 120.0	128.70	y	2202	25.4	PWS3
14R-4, 120.0	128.70	z	2189	25.3	PWS3
14R-4, 120.0	128.70	x	2162	25.3	PWS3
14R-5, 120.0	130.20	y	2207	25.1	PWS3
14R-5, 120.0	130.20	z	2245	25.1	PWS3
14R-5, 120.0	130.20	x	2275	25.0	PWS3
14R-6, 120.0	131.70	y	2226	24.7	PWS3
14R-6, 120.0	131.70	z	2569	24.7	PWS3
14R-6, 120.0	131.70	x	2309	24.8	PWS3
15R-1, 66.0	133.26	y	2248	24.9	PWS3
15R-1, 66.0	133.26	z	2289	24.9	PWS3
15R-1, 66.0	133.26	x	2325	24.9	PWS3
15R-4, 43.0	137.48	x	2341	25.2	PWS3
15R-4, 43.0	137.48	z	2007	25.1	PWS3
15R-4, 43.0	137.48	y	2308	25.2	PWS3
15R-4, 132.0	138.37	z	2053	25.2	PWS3
15R-4, 132.0	138.37	x	2391	25.2	PWS3
15R-4, 132.0	138.37	y	2328	25.2	PWS3
15R-5, 44.0	138.99	z	1960	25.2	PWS3
15R-5, 44.0	138.99	y	2254	25.1	PWS3
15R-6, 91.0	140.96	z	1951	25.1	PWS3
15R-6, 91.0	140.96	y	2168	24.9	PWS3
15R-6, 91.0	140.96	x	2150	25.0	PWS3
15R-7, 66.0	142.21	z	1931	25.0	PWS3
15R-7, 66.0	142.21	y	2135	24.9	PWS3
16R-1, 85.0	143.05	x	2223	24.9	PWS3
16R-1, 85.0	143.05	z	2003	24.9	PWS3
16R-1, 85.0	143.05	y	2226	24.9	PWS3
16R-2, 96.0	144.66	x	2166	24.8	PWS3
16R-2, 96.0	144.66	z	1973	24.8	PWS3
16R-2, 96.0	144.66	y	2217	24.7	PWS3
16R-3, 104.0	146.24	x	2139	24.9	PWS3
16R-3, 104.0	146.24	z	1977	24.9	PWS3
16R-3, 104.0	146.24	y	2171	25.0	PWS3
16R-4, 85.0	147.55	x	2121	25.2	PWS3
16R-4, 85.0	147.55	z	1949	25.2	PWS3
16R-4, 85.0	147.55	y	2163	25.2	PWS3
17R-1, 24.0	151.64	x	2059	23.8	PWS3
17R-1, 24.0	151.64	y	2095	23.8	PWS3
17R-1, 24.0	151.64	z	1862	23.8	PWS3
17R-2, 119.0	154.09	x	1982	23.6	PWS3
17R-2, 119.0	154.09	z	1892	23.6	PWS3
17R-2, 119.0	154.09	y	2031	23.6	PWS3
17R-3, 87.0	155.27	x	2009	23.7	PWS3
17R-3, 87.0	155.27	z	1901	23.7	PWS3
17R-3, 87.0	155.27	y	2061	23.7	PWS3
17R-4, 69.0	156.59	x	1998	23.7	PWS3
17R-4, 69.0	156.59	z	1977	23.7	PWS3
17R-4, 69.0	156.59	y	2060	23.6	PWS3
18R-1, 42.0	161.43	x	2349	23.5	PWS3
18R-1, 116.0	162.16	x	2350	23.5	PWS3
18R-2, 41.1	162.91	x	2255	23.5	PWS3
22R-1, 12.0	199.62	y	2093	23.2	PWS3
23R-1, 44.0	209.54	x	2109	25.8	PWS3
24R-2, 16.0	220.36	x	1937	23.9	PWS3
25R-1, 49.1	228.79	x	2170	23.4	PWS3
26R-1, 65.1	238.55	x	2140	23.7	PWS3
26R-2, 21.7	239.62	x	2289	22.6	PWS3
26R-2, 78.3	240.18	x	4015	23.0	PWS3
27R-1, 114.7	248.75	x	2172	22.6	PWS3
28R-1, 25.4	257.45	x	2074	23.7	PWS3
28R-1, 91.8	258.12	x	2222	22.5	PWS3
28R-1, 121.7	258.42	x	2318	22.4	PWS3
30R-1, 10.0	276.50	x	2022	26.6	PWS3
30R-1, 10.0	276.50	y	2033	26.6	PWS3
30R-1, 10.0	276.50	z	1914	26.6	PWS3
31R-1, 94.8	286.95	x	1784	23.9	PWS3
31R-2, 22.7	287.73	x	1862	25.5	PWS3
32R-1, 51.6	295.82	x	1835	22.9	PWS3
32R-1, 83.7	296.14	x	5419	23.2	PWS3
32R-1, 105.0	296.35	x	1902	23.3	PWS3
32R-1, 112.6	296.43	x	5739	22.7	PWS3
32R-2, 61.6	297.42	x	1846	23.5	PWS3
34R-1, 22.3	314.12	x	1892	26.1	PWS3
34R-1, 66.5	314.57	x	2035	26.0	PWS3
34R-1, 82.7	314.73	x	1830	26.1	PWS3

Notes: PWS1 = *P*-wave sensor 1, PWS2 = *P*-wave sensor 2, PWS3 = *P*-wave sensor 3. This table is also available in **ASCII format.**

Table T8. Measurements of undrained shear strength, Site 1166.

Automated vane shear data		Fall cone data		Pocket penetrometer data	
Depth (mbsf)	C_u (kPa)	Depth (mbsf)	C_u (kPa)	Depth (mbsf)	C_u (kPa)
2.66	39	2.63	53	20.50	560
		20.50	370	38.88	363
		38.90	400	75.35	350
		66.01	400	84.67	370
		75.35	400	94.95	530
		84.67	400	104.60	773
		104.60	370	105.56	527
				114.48	900
				114.71	400
				114.95	640
				115.76	400
				116.10	900
				116.99	650
				124.15	880
				125.65	590
				127.15	880
				128.65	847
				130.15	900
				131.65	900
				133.20	500
				135.15	660
				139.65	900

Note: This table is also available in **ASCII format.**

Table T9. Full- and half-space needle measurements of thermal conductivity, Site 1166.

Core, section, interval (cm)	Depth (mbsf)	Thermal conductivity measurements (W/[m·°C])					
		Type	Reading 1	Reading 2	Reading 3	Reading 4	Average
188-1166A-							
3R-1, 75	20.55	Full	1.311	1.370	1.338		1.340
9R-1, 47	75.47	Full		0.979			0.979
9R-1, 55	75.55	Full	1.575	1.516	1.649		1.580
11R-1, 60	94.60	Full	1.296	1.435	1.571		1.434
11R-1, 60	94.60	Full	1.582	1.472	1.453		1.502
12R-1, 119	104.89	Full	1.554	1.567	1.605		1.575
13R-2, 91	115.71	Full	1.294	1.264	1.398		1.319
13R-2, 55	115.35	Full	1.032	1.009	0.097		0.713
14R-4, 75	128.25	Full	1.559	1.682	1.624		1.622
15R-2, 85	134.90	Full	1.123	1.282	1.143		1.183
16R-3, 83	146.03	Half	0.793	1.023	0.970	0.964	0.938
17R-2, 52	153.42	Half	2.188	1.987	2.383	2.079	2.159

Notes: Type = full-space or half-space needle probe. Full-space needle probe number = V00694, half-space needle probe number = H19608. This table is also available in **ASCII format.**

Table T10. Logging operations summary, Hole 1166A.

Operations depth summary	Run 1 Triple combo (Main)	Run 2 GHMT-sonic (Main and repeat)	Run 3 FMS-NGT (Passes 1 and 2)	Comments
				Logging operations commenced at 1600 hr on 2/20/00. Wiper trip, sepiolite was circulated; no KCl used. Sea state/heave: average 0.5 m; maximum 1.5 m.
Water depth, seafloor or mudline:				
Mudline (mbrf): driller's depth	486.7	486.7	486.7	Run into hole speed = 7000 ft/hr.
Mudline (mbrf): logger's depth	480.0	480.0	480.0	Triple combo uprun speed = 900 ft/hr.
Mudline (mbsl)	475.4	475.4	475.4	GHMT-sonic uprun speed = 900 ft/hr; 1200 ft/hr.
				FMS-NGT uprun speed = 1600 ft/hr; 1700 ft/hr.
Drill-pipe depth during logging:				Logging operations ceased at 0800 hr on 2/21/00.
Initial pipe depth (mbrf): driller's depth	527.9	527.9	527.9	
Initial pipe depth (mbsf): using driller's depth	41.2	41.2	41.2	
Final pipe depth (mbrf): driller's depth	513.0	513.0	513.0	Initial pipe depth was set at 41.2 mbsf, and pipe was pulled up to 30 mbsf during upruns to give greater coverage of the open hole.
Final pipe depth (mbrf): depth from logs	510.0	510.0	510.0	
Final pipe depth (mbsf): using driller's depth	26.3	26.3	26.3	
Final pipe depth (mbsf): using logger's depth	32.0	30.0	30.0	Final pipe depth = initial log depth.
Sticking encountered during logging:				
Depth of first bridge or ledge (mbrf; winch)		650.0		No ledges or bridges encountered on first run into hole.
Depth of first bridge or ledge (mbsf)		170.0		Some sticking experienced at ~170 mbsf on repeat of run 2.
Final tool depth:				
(mbrf; winch)	863.0	864.5	864.9	
(mbsf): using logger's depth	383.0	384.5	384.9	
Total hole depth (m):	381.3	381.3	381.3	All three runs (including both passes of runs 2 and 3) reached total depth, giving maximum open-hole coverage. The upper 40 m to the seafloor were successfully logged with LWD/MWD.
Length of logging run (m):	353.0	354.5	354.9	

Note: GHMT = geological high-resolution magnetic tool; FMS = Formation MicroScanner; NGT = natural gamma-ray tool; mbrf = meters below rig floor; mbsl = meters below sea level; LWD = logging while drilling; MWD = measurement while drilling.

Table AT1. Summary of accessory components identified in foraminiferal residues.

Core, section, interval (cm)	Residue size	Content	Sorting	Planktonic foraminifers	Benthic foraminifers	Sponge spicules	Echinoid spines	Bone	Black coal	Wood	Pyrite	Micrometeorite
188-1166A-												
1R-1, 16-21	L	T		C	C	X	X		Tr			
1R-1, 117-122	L	T	P	C	C	X	X		C			
1R-2, 9-12	L	T		C	C	X	X					
1R-1-CC	L	T	P	B	B	Tr			Tr			
2R-CC	L	T		B	B	Tr			Tr			
3R-2, base	L	T		F	R				Tr			X
4R-CC	L	T		R	R				Tr			
5R-1, 26-31	L	T		R	B				Tr		Tr	
5R-CC	L	T	P	F	R						Tr	
R-CC	S	T		R	R				Tr			
7R-CC	L	T		F	R				Tr			
8R-1, 42-45	L	T		R	B							
8R-CC	L	T		B	B				Tr		Tr	
9R-CC	L	T		R	R				Tr		Tr	
1R-1, 11-13	L	T		C	C				Tr			
10R-CC	L	T	P	C	F							
11R-1, 47-50								N				
11R-CC	L	T	P	C	R						Tr	
12R-1, 18-20	L	T	P	R	R		X		Tr			
12R-CC	S	T	P	B	B	Tr			Tr			
14R-CC	L	T	P	B	B				C		Tr	
17R-CC	L	T	P	B	B					N		

Notes: Residue size: L = large, S = small. Content: T = dominantly terrigenous. Sorting of terrigenous fraction: P = poor, G = good. Foraminifers: C = common, B = barren, F = few, R = rare. Other components: C = common, X = present, Tr = trace, N = noteworthy.